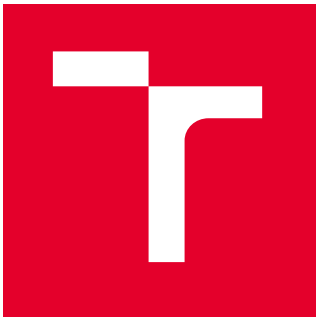

BRNO UNIVERSITY OF TECHNOLOGY

VYSOKÉ UČENÍ TECHNICKÉ V BRNĚ

CENTRAL EUROPEAN INSTITUTE OF TECHNOLOGY BUT

STŘEDOEVROPSKÝ TECHNOLOGICKÝ INSTITUT VUT

CERAMIC MATERIALS AND COMPOSITES FOR ADVANCED APPLICATIONS

KERAMICKÉ MATERIÁLY A KOMPOZITY PRO POKROČILÉ APLIKACE

DOCTORAL THESIS

DIZERTAČNÍ PRÁCE

AUTHOR — **Ing. Vojtěch Mařák**

AUTOR PRÁCE

SUPERVISOR — **Ing. Daniel Drdlík, Ph.D.**

ŠKOLITEL

BRNO 2024

Abstract

This thesis focuses on advanced oxide ceramics and particle and laminate composites. The materials studied include bioceramic hydroxyapatite, thermomiotic aluminium tungstate, and lead-free barium titanate-based piezoelectrics. These ceramics suffer from several limitations in their processing and properties, including the use of toxic stabilisers, low densification, susceptibility to cracking, undesirable chemical reactions, and poor mechanical and electrical performance. This work addresses these issues by tailoring individual processing steps and employing novel fabrication and treatment methods to optimise the desired performance of the materials. Plasma treatment of hydroxyapatite powder allowed electrophoretic deposition without toxic stabilisers, resulting in denser and crack-free coatings, as was also showcased on orthopaedic screws. Thermomiotic aluminium tungstate, known for its near-zero coefficient of thermal expansion, was synthesised by optimised co-precipitation to produce a powder with improved sinterability. Rapid pressure-less sintering and spark plasma sintering were used to densify the material to the highest density at the lowest temperature to date. The microstructural evolution of barium titanate piezoceramics was studied using rapid pressure-less sintering and radiation-assisted sintering. The gained knowledge was used to sinter barium titanate-based particle composites with reinforcing tougher oxide ceramics. High reactivity between selected materials had a negative influence on the properties of the composites, and one of the reaction products was characterised in greater detail. Laminated composites were prepared by alternating barium titanate-based and dielectric zirconia layers. The high reactivity of piezoelectric materials was inhibited by the sintering strategy. In summary, this dissertation thesis aims to improve the understanding of ceramic material properties and processing techniques, provide insight into performance optimisation, and address critical limitations across diverse applications.

Keywords

Ceramics, Hydroxyapatite, Aluminium tungstate, Barium titanate, Alumina, Zirconia, Particle composites, Laminated composites, Sintering, Microstructure, Phase composition, Mechanical properties, Electrical properties

Abstrakt

Tato dizertační práce se zaměřuje na pokročilou oxidovou keramiku a částicové a vrstevnaté kompozity. Studované materiály zahrnují biokeramický hydroxyapatit, termomiotický wolframan hlinitý a bezolovnaté piezoelektrické materiály na bázi titaničitanu barnatého. Příprava těchto keramik má několik omezení ovlivňující finální vlastnosti, zahrnující použití toxických stabilizátorů, nízké zhutnění, náchylnost k praskání, vznik nežádoucích chemických reakcí, nízké mechanické a elektrické vlastnosti. Tato práce řeší tyto problémy přizpůsobením jednotlivých kroků zpracování a použitím progresivních výrobních metod pro optimalizaci požadovaných funkčních vlastností materiálů. Úprava hydroxyapatitového prášku studenou plazmou umožnila elektroforetickou depozici bez toxických stabilizátorů, což vedlo k hutnějším povlakům bez trhlin. Praktický benefit tohoto přístupu byl demonstrován v případě bezdefektních hydroxyapatitových povlaků ortopedických šroubů. Termomiotický wolframan hlinitý, vyznačující se svým téměř nulovým koeficientem tepelné roztažnosti, byl syntetizován optimalizovanou koprecipitací za účelem zlepšení slinovatelnosti prášku. Rychlé beztlaké slinování a slinování plazmovou jiskrou byly použity ke zhutnění materiálu, přičemž bylo dosaženo dosud nejvyšších publikovaných hodnot hustot při nejnižší slinovací teplotě. Vývoj mikrostruktury piezokeramiky titaničitanu barnatého byl studován pomocí rychlého beztlakého slinování a slinování s pomocí radiace. Získané poznatky byly využity pro slinování částicových kompozitů na bázi titaničitanu barnatého vyztuženého oxidovými keramikami. Vysoká reaktivita mezi zvolenými materiály měla negativní vliv na vlastnosti kompozitů a jeden z reakčních produktů byl podrobněji charakterizován. Byly připraveny vrstvené kompozity střídáním vrstev na bázi titaničitanu barnatého a dielektrického oxidu zirkoničitého. Vysoká reaktivita piezoelektrických materiálů byla potlačena volbou slinovací strategie. Souhrnným cílem této disertační práce je posunout vědění v oblasti vlastností a zpracování keramických materiálů, poskytnout náhled na optimalizaci funkčnosti a řešit kritická omezení v různých aplikacích.

Klíčová slova

Keramické materiály, Hydroxyapatit, Wolframan hlinitý, Titaničitan barnatý, Oxid hlinitý, Oxid zirkoničitý, Částicový kompozit, Vrstevnatý kompozit, Slinování, Mikrostruktura, Fázové složení, Mechanické vlastnosti, Elektrické vlastnosti

Bibliografická citace

MAŘÁK, Vojtěch. *Keramické materiály a kompozity pro pokročilé aplikace*. Brno, 2024. Dostupné také z: https://www.vut.cz/studenti/zav-prace/detail/161274. Dizertační práce. Vysoké učení technické v Brně, Středoevropský technologický institut VUT, Středoevropský technologický institut VUT. Vedoucí práce Daniel Drdlík.

Declaration

I declare that I wrote this doctoral thesis using available literature and under the guidance of my supervisor.

…… ……..

Date Ing. Vojtěch Mařák

Acknowledgement

I want to thank my family and my fiancé for their ongoing support during my studies. Special thanks go to my supervisor, Ing. Daniel Drdlík, PhD, whose guidance and knowledge were essential for completing this work and improving my professional skills and knowledge. I would also like to acknowledge all CEITEC VUT, IPM CAS, and other colleagues who freely offered their expertise and help.

Contents

1 Introduction

Advanced ceramic materials are attracting the attention of industry and research due to their unique properties. They possess qualities such as high durability, chemical stability, biocompatibility, or intriguing mechanical, thermal, optical, and electrical properties, and are increasingly used for high-tech applications [1,2]. Their properties and subsequent performance are closely related to the processing and microstructure. In recent decades, the design of optimised materials has followed the three-link chain of the central paradigm, linking processing to microstructure, microstructure to properties, and finally, properties to performance. Top-down thinking is increasingly used, and modern advanced materials are designed with specific properties and performance in mind [3].

The processing of the material forms the basis for all its properties, and processing optimisation can occur at any stage of the manufacturing of advanced ceramic materials: powder synthesis, powder consolidation, or heat treatment [4]. Improvements in powder synthesis using chemical and vapour-phase methods allow the production of ceramic nanopowders with controlled particle size distribution, phase composition, and high purity [1]. Powder functionalisation can change the powder morphology [5], the particle size [1], and the surface state of the particles [6]. Finally, heat treatment offers many possible optimisations, such as sintering temperature, heating rate, applied pressure, and sintering atmosphere [1,7].

In addition to processing optimisations, the final performance of advanced ceramic materials can be influenced by changes in their composition. Additional phases can significantly affect the properties of the material. The resulting ceramic composite can be either fibre/whisker reinforced [8,9], laminated [10], or particle [11] type. Fibre composites can help to improve mechanical properties mostly through fibre pulling and laminated composites through crack deflection and internal compressive stresses [8,10]. The addition of a secondary phase in the form of particles to the ceramic matrix can lead to chemical reactions and the formation of new phases [12], the introduction of beneficial internal compressive stresses [13], or the pinning effect [11], and subsequent grain size optimisation and improvement in mechanical and electrical performance.

This work focuses on advanced single-phase and composite oxide ceramic materials: bioceramics, thermomiotics, and lead-free electroceramics. Optimisations involving powder synthesis and functionalisation, consolidation, phase composition tailoring, and advanced heat treatment techniques are implemented and thoroughly investigated. The resulting structures are analysed, and materials are optimised for performance in advanced applications.

2 Current state of the studied topic

2.1 Advanced ceramic materials

Advanced ceramic materials fabricated from pure precursors are crucial compounds in every aspect of modern society. Their industrial and research applications range from automotive, energy, electronics, construction, space, robotics, medical, and many more [1,2]. Compared to other material groups, e.g., plastics or metals, they offer intriguing properties, such as high hardness, compressive strength, bioinertness, biocompatibility, bioresorbability, ferroelectricity, pyroelectricity, piezoelectricity, semiconductivity, luminescence, thermomiotic behaviour, and chemical inertness [1]. This work considers three groups of materials: bioceramic calcium phosphates, thermomiotic aluminium tungstates, and lead-free electroceramics based on barium titanate.

2.1.1 Single-phase oxide ceramics

Bioceramics

Calcium phosphates are composed of calcium cations and phosphate anions and form a major inorganic compound in human bones [14]. For this reason, synthetic calcium phosphates have been widely-studied for clinical use as scaffolds, coatings, and implants [15–17].

One of the most important bioceramics, hydroxyapatite (HA), has a Ca/P ratio similar to human calcified tissue (1.67) [18]. HA is mostly used as a coating because its hardness and brittleness prevent it from being used in high-load applications [19,20]. Coatings on metallic implants have been shown to improve fixation, biocompatibility, and bioactivity [14], but proper selection of the processing method is necessary concerning the final biomedical application of the product.

Thermomiotics

Advanced ceramic materials with thermomiotic behaviour, i.e., possessing negative, near-zero, or low-positive coefficient of thermal expansion (CTE), have been investigated for their potential use in improved thermal shock-resistant components [21–23]. The orthorhombic $A_2M_3O_{12}$ family of ceramics is characterised by trivalent cations *A* (Al^{3+} to Dy^{3+} ionic radius), *M* (W^{6+} or Mo^{6+}), and oxygen. During heating, transverse vibration of the bridging oxygen atom in an *A*–O–*M* unit decreases the *A*–O–*M* angle, which reduces the *A*–*M* non-bonding distance and can manifest macroscopically as thermomiotic behaviour

[24–26]. However, due to their anisotropic CTE, $A_2M_3O_{12}$ ceramics are prone to microcracking in sintered bodies [27]. In the case of $Al_2W_3O_{12}$, difficulties in obtaining a homogeneous, dense, and fine microcrack-free microstructure affect the mechanical properties, and the tensile strength can drop to less than 10 MPa [21]. In conclusion, processing optimisations are required to overcome these challenges.

Lead-free electroceramics

Electroceramic materials are used to manufacture multilayer ceramic capacitors, piezoelectric actuators, sensors, transducers, harvesters, etc., thanks to their dielectric, ferroelectric, and piezoelectric properties [1]. One of the most widely used and studied materials is lead zirconium titanate. Discovered in the 1950s [28,29], this perovskite compound has a higher piezoelectric response and operating temperature than the oldest ferroelectric oxide in use—barium titanate [30]—but the presence of lead in the structure is fatal to its nowadays applications. Lead is hazardous to health and the environment, and since the adoption of a directive on the use of hazardous substances by the European Parliament [29,31,32], more research has focused on lead-free alternatives.

Barium titanate, $BaTiO_3$, the first ferroelectric oxide discovered during the Second World War, is still widely used in electronics applications thanks to its dielectric, ferroelectric, and piezoelectric properties [33]. These are due to its perovskite ABO_3 structure and tetragonal crystal lattice (P4mm), which is stable at room temperature. Ba^{2+} cations occupy the *A*-site in the corners of the lattice, and smaller Ti^{4+} cation occupies the *B*-site in the central octahedron (see **Fig. 1**). The tetragonal distortion of the cell is caused by a deflection of Ti^{4+} from the centre of the octahedron. The distortion leads to an intrinsic polarisation of the cell and transforms into the macroscopic piezoelectric properties of the material [1].

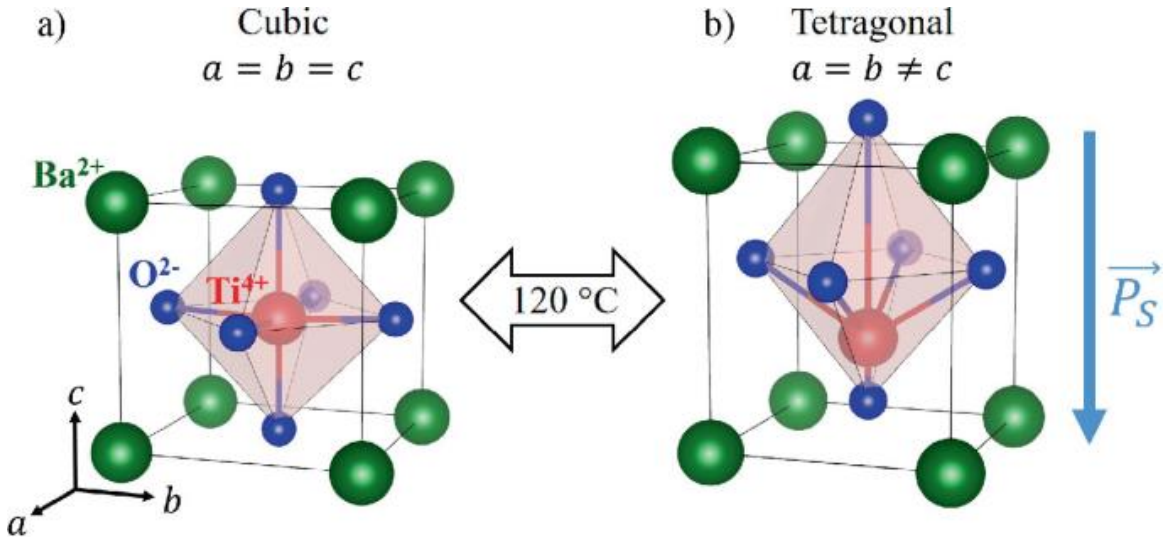

Fig. 1 Cubic and tetragonal $BaTiO_3$ crystal cell with the indicated direction of the intrinsic polarisation P_S [34].

The tetragonal phase transitions to orthorhombic near 0 °C and then to rhombohedral around – 90 °C [35,36]. However, above the Curie temperature T_C (~120 °C), the cubic phase becomes stable, and the piezoelectric properties deteriorate [31,37]. In addition, the non-perovskite hexagonal structural polymorph of barium titanate exhibits ferroelectric behaviour below – 199 °C [38].

However, $BaTiO_3$ is not an ideal electroceramic material—the highest dielectric performance is reported at a small temperature interval close to T_C [35,36], and properties strongly depend on purity [35] and grain size [39–41]. Therefore, microstructural tailoring of pure $BaTiO_3$ and doping with cations occupying both *A*-site (Ca) and *B*-site (Zr, Sn) are often used to improve its performance [42,43].

(Ba, Ca)(Zr, Ti)O_3 (BCZT), the most often used in $Ba_{0.85}Ca_{0.15}Zr_{0.1}Ti_{0.9}O_3$ composition [42,44,45] but also reported in different stoichiometries [46–49], is a well-studied modification of barium titanate that brings several advantages. The tetragonal-orthorhombic phase transition is shifted to ~30 °C [50], resulting in the co-existence of multiple phases at room temperature. The rhombohedral phase is also frequently detected, and the rhombohedral-orthorhombic-tetragonal morphotropic phase boundary can lead to higher electromechanical properties [47,49]. At the macroscopic level, a higher piezoelectric coefficient d_{33} than $BaTiO_3$ has been obtained [35].

2.1.2 Multi-phase oxide ceramics

Single-phase ceramics often have disadvantageous properties in crucial aspects such as inferior mechanical properties (especially brittleness), electrical properties and sintering behaviour, to name a few [1,35]. For this reason, ceramic composites offer an interesting opportunity to optimise performance by combining several materials with complementary properties. For example, adding a secondary phase in the form of particles or layers can improve the composite's toughness [10,11].

Particle composites

Particle composites, in general, use two or more phases with dispersed particles of various sizes to achieve the desired optimisation [11]. Combining piezoelectric $BaTiO_3$ with more mechanically durable dielectrics such as Al_2O_3 and ZrO_2 can significantly improve mechanical performance. $BaTiO_3/Al_2O_3$ composites have been extensively investigated, resulting in enhanced fatigue strength [51], Knoop hardness, Young's modulus [52], and fracture toughness [53,54]. Similarly, adding ZrO_2 to the microstructure improved properties such as higher density, relative permittivity, and reduced grain growth and dielectric loss [55,56].

Laminated composites

Laminated composites use alternating layers of two or more materials to enhance mechanical properties through mechanisms such as crack deflection and internal compressive stresses [10]. Therefore, laminates are a potential solution to the brittleness problem of piezoceramics, which limits their use. An inseparable multi-layer ceramic composite harvester has recently been proposed using $BaTiO_3$ with Al_2O_3 and ZrO_2 [13]. It was demonstrated in the theoretical model that internal compressive stresses arising from the laminated structure can protect the brittle $BaTiO_3$ piezoceramic layers. Additional internal stresses in the $BaTiO_3$ layers can further improve the electromechanical performance. However, the main issue with the aforementioned laminated composite is the behaviour of the layers during the heat treatment. It has been shown that $BaTiO_3$ starts to shrink ~100 °C earlier than Al_2O_3 and ZrO_2 [13], and this discrepancy can lead to delamination and cracking of the layers [12,13], making sintering optimisations necessary.

The high reactivity of barium titanate-based systems is a challenge for fabricating the aforementioned composites. The formation of additional phases such as $BaTiAl_6O_{12}$, $BaAl_2O_4$, $Ba_4Ti_{10}Al_2O_{40}$, $BaAl_{13.2}O_{20.8,}$ and $BaZrO_3$ has been confirmed in the literature [12,51,52,54,57–59]. The chemical composition of the $Al_2O_3/BaTiO_3$ interface indicated the presence of a thick interlayer [12]. These intermediary phases typically have poorer electrical properties than $BaTiO_3$ and worse mechanical properties than the reinforcing phases. It is, therefore, desirable to limit the chemical reactions by tailoring the processing of the composites.

2.2 Processing of ceramic materials

The aforementioned single-phase and multi-phase advanced ceramic materials have several limitations in their performance. This thesis adopts a top-down approach to materials design [3], emphasising the production of materials with desired performance by optimising individual processing steps. Processing optimisations start with powder synthesis and functionalisation, followed by powder consolidation and heat treatment to obtain dense ceramic bodies with improved material properties.

2.2.1 Powder synthesis

Generally, powder synthesis is the first step leading to the final ceramic product. Therefore, optimising the synthesis is essential, as the prepared ceramic powder will influence further processing. The desired properties of the synthesised powders are fine particle size with narrow distribution without agglomeration, required particle shape, high purity, and single-phase composition [1]. Examples of optimisations include using higher-quality precursors and varying the solution's molarity, pH, and ageing time [21,60–62].

2.2.2 Powder functionalisation

The functionalisation of ceramic powders modifies their properties and facilitates consequent processing steps to obtain the final product's best performance. Modifications include particle size reduction by mechanical milling [63], change of surface properties by plasma activation [6] or various grafting compounds [64], adjustment of morphology and phase composition by heat treatment [65,66], and simple sieving to obtain specific particle size fractions [1].

High-energy ball milling

High-energy planetary ball milling allows effective particle size reduction using simple equipment. Reduced particle size results in increased surface energy, and improved sinterability and reactivity [63]. It has been shown to improve densification and grain size control, which positively affected the properties of final ceramics and ceramic composites, such as fracture toughness, strength, and electrical properties [67–70].

Plasma activation

In addition to altering the powder morphology and particle size during milling, powder functionalisation can enhance powder properties by introducing various surface adsorbed groups. This can be achieved by non-thermal plasma treatment applied at atmospheric pressure. For example, diffuse coplanar surface barrier discharge (DCSBD) has previously been used to optimise alumina processing. It increased the colloidal stability of the suspension, allowed the electrophoretic deposition (EPD) without any hazardous stabilisers, and the final ceramics achieved a finer and denser microstructure [6,71].

2.2.3 Powder consolidation

Once synthesised and functionalised, ceramic powders can be consolidated using various shaping techniques to achieve the desired shape. Powder consolidation techniques such as uniaxial pressing, cold isostatic pressing (CIP), EPD, sol-gel, and slip-casting are among the most widely used. Advanced methods combine powder consolidation with heat treatment, such as hot pressing, spark plasma sintering (SPS), and thermal spraying [1].

Wet route

Wet powder consolidation methods generally use ceramic particles dispersed in aqueous or non-aqueous media to form a suspension, paste, or gel. Extrusion and injection moulding are used for more complex shapes. Sol-gel uses organic and powder precursors to produce high-purity ceramic powders, fibres, thin films, and coatings. Slip-casting is a viable option for the simple preparation of bulk and shaped ceramics by suspension drying. Tape casting can be used to prepare films by doctor blade. Finally, electrophoretic deposition serves to prepare coatings or layers by electric field-driven ceramic powder consolidation [1].

During the EPD, a ceramic deposit is formed on the electrode directly from the stable colloidal suspension after applying an external electric field [72]. EPD has been established as a rapid and robust processing method suitable for the preparation of ceramic films [72], layers [73], or even bulk materials [74]. In addition, particle and laminated ceramic composites have also been prepared [12,13,75].

Dry route

Dry powder consolidation methods are an alternative to wet methods, allowing homogeneous bulk samples to be produced relatively easily. Uniaxial pressing is a fast and simple powder consolidation method suitable for producing simple-shaped ceramic bodies. The powder can be mixed with a binder or a pressing aid, poured into the mould, and then pressed between two pistons. The pressure is usually in the tens of MPa but can be as high as 1 GPa. CIP may follow to increase powder consolidation and uniformity. The hydraulic oil isostatically compresses the sample in the rubber container in the pressure chamber. The pressure is often in the hundreds of MPa, higher than for uniaxial pressing. CIP is a quick and easy method that allows the consolidation of more complex shapes [1].

2.2.4 Heat treatment

Sintering

After powder consolidation, heat treatment—sintering—of the green body follows. Sintering is a thermodynamic process in which consolidated particles are bonded together, followed by fusion into grains without melting [1], with subsequent changes in shape and size [76]. It also involves transporting material by diffusion into the pores and their shrinkage and removal. Grain boundary (GB) diffusion, lattice diffusion, and grain rearrangement contribute to the shrinkage and densification of the ceramic body [77].

Direct measurement of shrinkage during sintering is possible using dilatometry. Shrinkage curves can provide valuable data on densification progress [76], CTE [60,76], phase transformations [78], thermal hysteresis [78], and are essential for rate-controlled sintering [79].

Grain growth is a complementary phenomenon to densification. The direction of the grain growth is always towards the centre of curvature of the GB, and the movement of the GB is due to the pressure difference and the vacancy gradient [1]. The coarsening of the microstructure usually has a detrimental effect on the mechanical, optical, and electrical properties of ceramic materials [35,39,40].

It is possible to prevent unwanted grain growth by using unconventional sintering methods: pressure-assisted sintering methods such as hot isostatic pressing and SPS [80,81], two- and three-step sintering [60,82], microwave sintering [83], flash sintering [84], rapid pressure-less sintering (RPLS) [41,85], or radiation-assisted sintering [86,87].

Rapid pressure-less sintering

Rapid pressure-less sintering, also known as fast firing, is a progressive method where ceramic samples achieve high densification using a fraction of the necessary time and energy [88]. A high heating rate can accelerate the densification process through early activation of lattice diffusion and GB diffusion [88,89] and densification front formation [90]. Conventional sintering cycles are typically orders of magnitude longer, and the time savings are comparable to SPS [80] or microwave sintering [91]. The decrease in energy consumption leads to substantial economic and environmental benefits.

The aforementioned sintering mechanisms can lead to intriguing results. RPLS has been successfully used for various ceramic materials such as Al_2O_3 [92–94], tetragonal ZrO_2 [85,94,95], electroceramics such as $BaTiO_3$ [41] and BCZT [42], calcium phosphates [96], and even more unusual compounds such as Sm-doped CeO_2 [97].

Spark plasma sintering

Another established advanced heat treatment method is SPS. Ceramic powder is placed in a graphite die between two graphite punches, uniaxially pressed, and a low voltage electric current is applied to generate heat (see **Fig. 2**a) [98]. The maximum achievable temperature is up to 2400 °C. SPS is frequently used to densify a wide range of materials, such as refractory metals, intermetallics, ultra-high-temperature ceramics, transparent ceramics, nanostructured and functionally graded materials [80], aluminium tungstate [60], and lead-free electroceramics, producing dense samples with controlled grain size [99–103].

Radiation-assisted sintering

SPS equipment can be modified using graphite crucibles to eliminate the influence of the pressure during the sintering (see **Fig. 2**b). A direct comparison between SPS and radiation-assisted sintering of ZrO_2 showed similar densification and microstructural state of the sintered bodies [98]. Due to the presence

of the vacuum, the majority of the energy available for densification comes from radiation (similar to RPLS), hence radiation-assisted sintering [87].

High heating rates (hundreds of °C/min), good densification, and less shape constrictions (compared to SPS) have allowed radiation-assisted sintering of various materials, including structural ceramics such as ZrO_2 [86,98,104] and Al_2O_3 [87,105], lead-free electroceramics KNN [106], non-oxide ceramics SiC [107] and V_8C_7 [108], and even alloys, intermetallics, and pure metals [109–113].

Overall, radiation-assisted sintering offers the possibility of optimising the sintering process in terms of the final performance of the material; it serves as an alternative to RPLS performed in air and to SPS with added pressure.

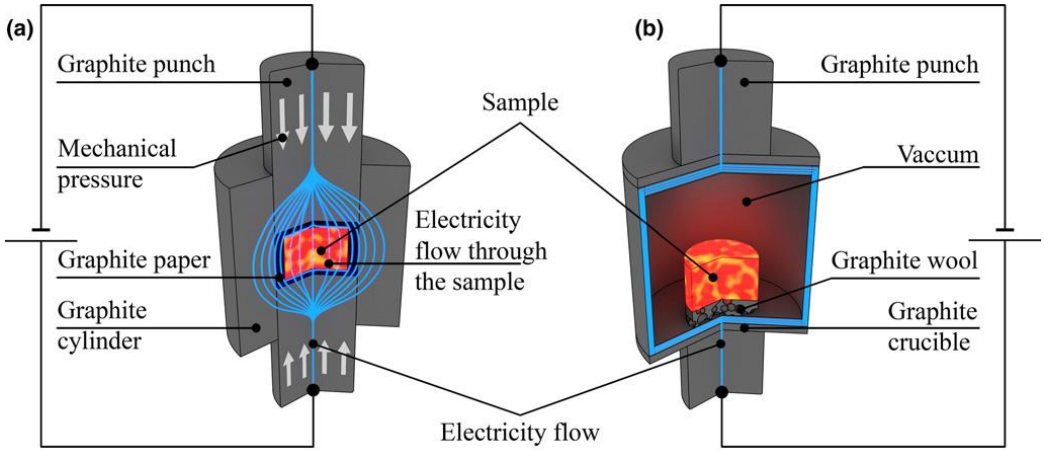

Fig. 2 Schematic setup for a) pressure-assisted sintering and b) radiation-assisted sintering in an SPS machine [98].

3 Aims of the thesis

This thesis aims to advance selected ceramic materials. The studied materials have several limitations restricting their full application potential. To overcome these issues, this work embraces a top-down material design approach, and the focus is placed on preparing the materials with improved properties for better performance by optimising individual processing steps: powder synthesis, functionalisation, consolidation, and sintering.

The goals include:

1. Functionalisation of the hydroxyapatite powder using plasma activation for optimised orthopaedic biocoatings densified by RPLS technique.
2. Examining the influence of powder synthesis and treatment, calcination temperature, and rapid sintering methods on the final properties of $Al_2W_3O_{12}$.
3. Documenting the influence of non-conventional sintering methods on the microstructural evolution of $BaTiO_3$.
4. Studying $BaTiO_3$-based particle composites with added Al_2O_3 or ZrO_2.
5. Describing the fundamental properties of $BaTiO_3/Al_2O_3$ reaction product $BaTiAl_6O_{12}$.
6. Preparing laminate composites based on $BaTiO_3$ and ZrO_2 and mitigating interlayer reactivity by changing the composition of piezoceramic layers and the sintering strategy.

4 Methods and experimental

4.1 Sample preparation

4.1.1 Ceramic powders

Several commercial powders were used: hydroxyapatite (Nanografi, Turkey), tetragonal $BaTiO_3$ (Nanografi, Turkey), Al_2O_3 powder (Taimei Chemicals, Japan), Al_2O_3 platelets (Merck, Germany), and 3 mol.% Y_2O_3-stabilised tetragonal ZrO_2 (ZrO_2, Tosoh, Japan). The basic characteristics of the powders are summarised in **Table 1**.

Table 1 Particle size and density of used commercial powders.

Powder	Primary particle size [nm]	Density [g/cm^3]
Hydroxyapatite	50	3.16
$BaTiO_3$	280	6.02
Al_2O_3 powder	120	3.99
Al_2O_3 platelets	6000–10000	3.99
ZrO_2	60	6.05

4.1.2 HA biocoatings

Hydroxyapatite powder was activated by DCSBD. A flat dielectric panel (96% Al_2O_3) with screen-printed comb-like high voltage electrodes generated a thin layer of non-thermal plasma. The width of the electrode strips was 1.5 mm, and their mutual distance was 1 mm. 0.05 g of HA powder was sieved onto the discharge zone, covered with an alumina plate shield, and activated for 60 s using a 15 kHz transformer and 400 W power input. The activation was performed under ambient conditions, and maximum temperature of the DCSBD panel was kept below 70 °C. The process and schematic representation of the apparatus has been described in the literature [71].

EPD suspensions consisted of 15 wt.% HA dispersed in 2-propanol (p.a., Lachner, Czech Republic). The 2-propanol content was appropriately reduced when monochloracetic acid (MCAA, p.a., Sigma-Aldrich, Germany) was added as a stabiliser at concentrations of 0, 0.85, and 12.75 wt.%. The suspensions were stirred in an ultrasonic bath for 30 min. The EPD was performed in a horizontal cell with two polished stainless-steel electrodes 26 mm apart with an effective surface area of 8.8 cm^2. A constant current of 5 mA was maintained for 60 min. The deposition was interrupted every 5 min to stir the suspension and weigh the electrode with the deposit. After deposition, the deposits were air-dried for 24 h and removed from the electrodes for further analysis as stand-alone samples.

Cancellous orthopaedic stainless-steel screws (Beznoska, Czech Republic) were used as cathodes and coated by HA in the same setup described above. During these depositions, the screws rotated 2 rps. The EPD lasted 2 min for the suspension containing plasma treated HA powder and 2 s for the suspension containing as received powder to achieve the desired coating thickness. The orthopaedic screws were coated without MCAA stabiliser in the suspensions.

Densification of deposited samples was achieved using RPLS in a superkanthal elevator furnace with a moving sample holder (Clasic, Czech Republic), which allowed quick sample insertion into the preheated furnace chamber. Sintering was performed at temperatures 1100, 1200, and 1300 °C with heating and cooling rates between 5 and 100 °C/min and dwell times of 10 and 120 min.

4.1.3 $Al_2W_3O_{12}$ thermomiotics

Amorphous $Al_2W_3O_{12}$ powder was synthesised by the co-precipitation method. The precursors $Al(NO_3)_3 \cdot 9H_2O$ (Alfa Aesar, USA) and $Na_2WO_4 \cdot 2H_2O$ (Sigma-Aldrich, USA) were dissolved in distilled water at a concentration of 0.005 M in 2:3 stoichiometric ratio. The resulting white precipitates were centrifuged at 5000 rpm for 5 min and washed thoroughly with ethanol. The amorphous precipitates were dried at 90 °C for 12 h and ground in an agate mortar. The amorphous powder was calcined in the RPLS furnace at 500–620 °C for 20 min using heating and cooling rates of 100 °C/min. The calcined crystalline $Al_2W_3O_{12}$ powder was milled in deionised water in a planetary ball mill Pulverisette 5 Classic (Fritsch, Germany) for 10 min in zirconia containers with 5 mm zirconia balls as a milling medium. The powder was dried, ground in an agate mortar, and sieved through a 100 μm mesh before compaction.

Dry pressing was used to compact calcined $Al_2W_3O_{12}$ powder. Uniaxial pressing was performed at 15 MPa pressure in a 5 mm diameter graphite die. CIP was performed at 700 MPa. Compacted green bodies were densified using high-temperature dilatometry and RPLS. A high-temperature dilatometer L70/1700 (Linseis, Germany) was used to measure shrinkage curves at 10 °C/min heating and cooling rates with 60 min dwell at 1000 °C. RPLS was performed at heating and cooling rates of 100 °C/min with 10 and 60 min dwell at 1000 °C sintering temperature. SPS was conducted in a Dr. Sinter 615 (Fuji, Japan) using a 10 mm carbon die. The applied pressure during SPS was 50 MPa and heating and cooling rates were 100 °C/min with a dwell time of 2 min at 850 and 1000 °C sintering temperature. The theoretical density (TD) of $Al_2W_3O_{12}$ used for further calculations was 5.08 g/cm^3 [114].

4.1.4 $BaTiO_3$ for rapid pressure-less sintering and radiation-assisted sintering

$BaTiO_3$ powder was annealed at 600 °C for 60 min to remove organic residues and moisture. The powder was then mixed in ethanol with 1 wt.% of polyethylene glycol (PEG) binder (mw 200, Sigma-Aldrich, USA) and 5 mm ZrO_2 balls as milling media. Suspensions were mixed for 24 h on a roller bench, dried, ground in an agate mortar, and sieved through 500 µm mesh before compaction. Uniaxial pressing was performed at 15 MPa in a 30 mm stainless steel die. CIP was performed at 300 MPa for 5 min. The compacted $BaTiO_3$ pellets were calcined in a muffle furnace (Clasic, Czech Republic) at 800 °C for 60 min to burn out the organic binder. The RPLS and radiation-assisted sintering cycles consisted of 100 °C/min heating and cooling rates and 5 min dwell time at a sintering temperature in the range of 1200–1300 °C (RPLS) and 1325–1400 °C (radiation-assisted sintering).

4.1.5 $BaTiO_3$-based particle composites

The $BaTiO_3$-based composites with fine dispersion of secondary phases were densified by RPLS, and therefore, dry-pressed green bodies were prepared. Appropriate ratios (0, 3, 5, 10 vol.% of Al_2O_3 or ZrO_2 in $BaTiO_3$) of powders were mixed in ethanol with 1 wt.% of PEG binder (mw 200, Sigma-Aldrich, USA) and 5 mm Al_2O_3 or ZrO_2 balls as a milling media. Suspensions were mixed for 24 h on a roller bench, dried, ground in an agate mortar, and sieved through 500 µm mesh before compaction. Uniaxial pressing was performed at 15 MPa pressure in a 30 mm stainless steel die. CIP was performed at 300 MPa for 5 min. Compacted $BaTiO_3$ pellets were calcined in a muffle furnace (Clasic, Czech Republic) at 800 °C for 60 min to burn out organic binders. The RPLS regime consisted of heating and cooling rates of 100 °C/min and dwell time of 15 min. The sintering temperature was 1250 °C.

4.1.6 $BaTiAl_6O_{12}$

To explore one of the most significant reaction products, i.e., $BaTiAl_6O_{12}$, $BaTiO_3$, and Al_2O_3 powders were mixed in a molar ratio of 1:3 and wet milled in a planetary ball mill Pulverisette 5 Classic (Fritsch, Germany) for 30 min in zirconia containers with 5 mm zirconia balls as a milling medium. The mixed powder was dried, ground in an agate mortar, and sieved through 500 µm mesh before further processing. The homogenised powder mixture was sintered in SPS at 1450 °C with a 5 min dwell and 100 °C/min heating and cooling rates. Prior to further characterisation, $BaTiAl_6O_{12}$ sintered samples were annealed at 1400 °C for 5 h to remove carbon contamination.

4.1.7 $BaTiO_3$ and BCZT-based ceramic laminates

BCZT ceramics of the composition $(Ba_{0.85}Ca_{0.15}Zr_{0.1}Ti_{0.9})O_3$ were synthesised by solid-state reaction from $BaCO_3$ (Dakram, United Kingdom), $CaCO_3$ (Lachner, Czech Republic), TiO_2 (Dakram, United Kingdom), and ZrO_2 (Dakram, United Kingdom). The precursors were dried at 220 °C for 2 h and weighed according to the stoichiometric ratios. The powders were wet milled in ethanol with ZrO_2 milling balls for 24 h on a roller bench. The powder was dried at 90 °C for 10 h, sieved through 300 μm mesh and calcined at 1250 °C for 4 h to obtain the final product ready for the preparation of laminated composites by EPD.

EPD suspensions consisted of 15 wt.% of $BaTiO_3$, BCZT, or ZrO_2 ceramic powders dispersed in 2-propanol and stabilised with 12.75 wt.% of MCAA. The suspensions were stirred in an ultrasonic bath for 30 min. The EPD was performed in a horizontal cell with two polished stainless-steel electrodes 26 mm apart with an effective surface area of 18.7 cm^2. A constant current of 5 mA was maintained. The layered structure was created by switching the deposition electrode from one deposition cell (containing dielectric ceramics) to another (containing piezoelectrics). The EPD kinetics required for precise layer thickness were designed based on the literature data [13,44,115]. After deposition, the deposits were air-dried for 24 h and removed from the electrodes for further analysis as stand-alone samples. Two types of laminated composites were prepared: alternating layers of $BaTiO_3/ZrO_2$ and $BCZT/ZrO_2$.

The laminated deposits were sintered conventionally and by SPS. Before sintering, the deposits were ground and shaped into cylinders with a 12 mm diameter. The conventional sintering cycle in a high-temperature furnace (Clasic, Czech Republic) used a heating rate of 5 °C/min with a 120 min dwell time at 1300 °C ($BaTiO_3/ZrO_2$) or 1500 °C ($BCZT/ZrO_2$). SPS was performed at 100 °C/min heating and cooling rates and 5 min dwell at 1250 °C ($BaTiO_3/ZrO_2$) or 1350 °C ($BCZT/ZrO_2$) under 50 MPa pressure in a 12 mm diameter carbon die.

4.2 Sample characterisation

4.2.1 Powders and suspensions

Particle size distributions of the powders were measured using an LA950 analyser (Horiba, Japan), and surface area was analysed by the Brunauer-Emmett-Teller (BET) method on a NOVA touch LX^2 gas sorption analyser (QuantaChrome, USA). Thermogravimetry (TG), mass spectroscopy (MS), and differential scanning calorimetry (DSC) analyses were performed using the STA 409 C/CD analyser

(Netzsch, Germany). The electrical conductivity of HA powder suspensions was measured using a SevenCompact Conductivity S230 (Mettler Toledo AG, Switzerland) equipped with a platinum 4-plate conductivity probe (0–500 $mS \cdot cm^{-1}$, 0–100 °C, 0.80 cm^{-1}). The zeta potential of HA suspensions was measured using a Zetasizer Nano ZS (Malvern Instruments, United Kingdom).

4.2.2 Densification and dilatometry

The density of green bodies and sintered samples was determined by the Archimedes method (EN 18754) using the theoretical densities of used materials given in Table 1. A high-temperature dilatometer L70/1700 (Linseis, Germany) was used to measure shrinkage curves at 10 °C/min heating and cooling rates and various sintering temperatures. The CTE of sintered $Al_2W_3O_{12}$ and $BaTiAl_6O_{12}$ samples was measured during cooling at a rate of 1 °C/min in the temperature range of 450–100 °C according to the equation [76]:

$$CTE = \frac{\varepsilon_{100} - \varepsilon_{450}}{(T_{100} - T_{450}) \cdot 100}, \quad (1)$$

where ε_{100} [%] is the shrinkage after cooling to 100 °C, ε_{450} [%] is the shrinkage at 450 °C, T_{100} [°C] is the temperature of 100 °C, and T_{450} [°C] is the temperature of 450 °C.

4.2.3 Microstructural, chemical, and phase composition characterisation

Scanning electron microscopy (SEM) was used to observe powder particles and the microstructure of polished and etched cross-sections of sintered samples. Verios 460L (Thermo Fisher, USA) and Mira 3 (Tescan, Czech Republic) SEMs were used. For chemical composition analysis, the Mira 3 SEM was equipped with an energy-dispersive X-ray spectroscopy (EDX) detector (Oxford Instruments, United Kingdom) operated by Aztec software. Electron backscatter diffraction (EBSD) maps of $BaTiAl_6O_{12}$ sintered sample were acquired using Lyra 3 (Tescan, Czech Republic) equipped with EBSD symmetry camera (Oxford Instruments, United Kingdom) and analysed in Aztec Crystal software. Grain size distribution was calculated from the set of EBSD maps with a grain boundary detection limit of 15°. The mean grain size (MGS) of sintered HA and $BaTiO_3$-based composite samples was determined by the linear intercept method multiplied by a correction factor 1.56 [116]. The share of abnormal grains in the microstructure was estimated from three SEM micrographs (2000 μm^2) of the polished surface. In the case of $Al_2W_3O_{12}$ sintered samples, grain area and grain area distributions were calculated using binary images of traced grains in ImageJ software.

X-ray diffractometry (XRD) was used to analyse the phase composition and crystallinity of powders, green bodies, and sintered samples. A Bragg-Brentano setup was used with a Cu-Kα radiation source (λ = 1.54 Å). XRD data evaluation was performed using PDXL2 software and the ICSD database. Raman spectroscopy was used to measure the vibrational characteristics of powders and sintered samples using a Witec Alpha 300R (Witec, Germany) with a 532 nm wavelength laser operating at 30 mW. X-ray photoelectron spectroscopy (XPS) was used to study the surface properties of powders. Measurements were performed on an AXIS Supra (Kratos Analytical, United Kingdom) with a monochromatic Al-Kα (1486.7 eV) excitation source. Spectra were calibrated to the adventitious carbon component C–C in the C 1s peak at 284.8 eV and further analysed in CasaXPS software.

Electron paramagnetic resonance (EPR) was used to determine the concentration of oxygen vacancies in $Al_2W_3O_{12}$ calcined powders. The spectrometer was equipped with a JM-PE-3 (Jeol, Japan) resistive magnet and a microwave source Magnettech MXH2 (Bruker, United States of America) with a magnetic field modulation amplitude of 0.92 G at 100 kHz, 20 mW, and 60 s scans. The *g*-splitting factor was calibrated against a $MgO:Cr^{3+}$ standard sample with $g = 1.9797$ and known spins concentration. The oxygen vacancy signal was compared to the standard, divided by the mass of the sample, and multiplied by the theoretical density of $Al_2W_3O_{12}$.

4.2.4 Mechanical characterisation

Hardness was measured on polished cross-sections of the samples using a Z2.5 hardness tester (Zwick/Roel, Germany) equipped with a ZHU02 instrumented hardness head and a Vickers diamond indenter. The load of 0.98 N was maintained for 10 s in the case of $Al_2W_3O_{12}$ samples, and the size of the indentations was measured using a confocal microscope LEXT OLS 3100 (Olympus, Japan) to calculate the Vickers hardness HV0.1. The indentation hardness, calculated from the depth of the indent, was measured in the case of $BaTiO_3$-based laminated composites with a load of 50 mN maintained for 12 s using the ZHN machine (Zwick/Roel, Germany). Young's modulus was calculated from the unloading part of the loading curves. At least 20 indentations were made for each sample.

The fracture toughness of $BaTiO_3$-based particle composites was measured using the chevron notch technique. Sintered discs were cut and polished to obtain bending bars (3.5 × 2.5 × 20 mm) with the required surface quality. A precision saw Isomet 5000 (Buehler, United States of America) was used to cut chevron notches in the bars. The bending bars were loaded in the three-point bending configuration

with a 16 mm span, and a crosshead speed of 0.005 mm/min was maintained by a universal testing system 8862 (Instron, USA). The geometric function was calculated using the slice model.

4.2.5 Electrical characterisation

The electrical properties of $BaTiO_3$-based samples were measured after applying Ag paste and firing the samples at 700 °C before poling in silicon oil at 3 kV/mm for 10 min. The dielectric properties were measured at room temperature in a frequency range between 10 mHz and 1 MHz using Alpha-A High Performance Modular Measurement System (Novocontrol, Germany) in ZGS Active Sample Cell. The quasistatic piezoelectric constant, d_{33} (pC/N), was measured by Berlincourt d_{33} meter (ZJ-3C, Institute of physics, China) after poling in silicon oil at 3 kV/mm for 10 min at room temperature.

5 Results and discussion

5.1 Hydroxyapatite coatings

This sub-chapter is dedicated to optimising HA powder properties by plasma treatment to stabilise the EPD suspensions without hazardous and toxic additives. The effects of the DCSBD treatment were described in terms of TG/MS and XPS analyses of the powder and electrical conductivity, zeta potential, and deposition behaviour of the suspensions. Several RPLS sintering cycles with sintering temperatures between 1100 and 1300 °C, dwell times 10 and 120 min and heating rates between 5 and 100 °C/min were used to obtain deposits with tailored porosity and microstructure. As a proof of concept, orthopaedic screws were coated to demonstrate the benefits of plasma treatment on the homogeneity and uniformity of HA coatings.

Powder properties

Firstly, the influence of plasma treatment on powder properties was investigated using simultaneous TG and MS analyses in the temperature range of 75–1300 °C. **Fig. 3**a shows similar mass change profiles for as received and plasma treated powders, but the total mass change was higher for the plasma treated HA: 6.5 vs 4.6%. This difference was most pronounced in the temperature range of 200–1000 °C, where the plasma treated powder showed a 1.5% higher weight loss. It can be explained by adsorbed molecules on the surface of the treated particles, as shown in **Fig. 3**b. A significant m/z = 44 peak around 320 °C confirmed the existence of N_2O or CO_2 molecules [117,118] and three m/z = 30 peaks at 300, 530, and 750 °C confirmed the presence of NO or NO_2 [71]. In addition, the m/z = 18 signal showed irreversible expulsion of lattice water and reversible expulsion of OH^- and formation of oxyhydroxyapatite in the temperature range of 100–400 °C and 900–1300 °C, respectively [119,120].

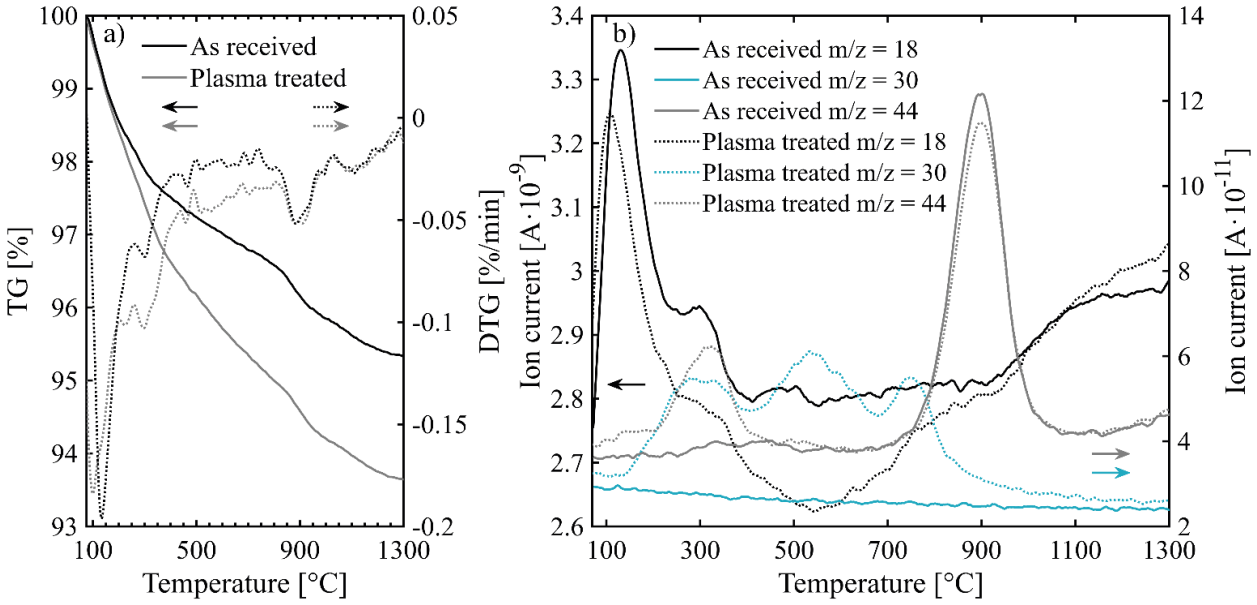

Fig. 3 TG/DTG (a) and MS (b) curves of as received and plasma treated HA powders [121].

The surface of the powders was examined in more detail by XPS. Five elements were detected: Ca, P, O, C, and N. Their mutual ratio remained practically unaffected by the plasma treatment, except for nitrogen, which increased from 1.3% to 2.9%. A detailed investigation with peak deconvolution of the C 1s peak of the as received and plasma treated powder is shown in **Fig. 4**a and **Fig. 4**c, respectively. The as received powder contained the components C-C at 284.8 eV (adventitious carbon, calibrated to this value), C-O at 286.3 ± 0.2 eV, and C=O at 288.6 ± 0.1 eV. Plasma treated powder spectrum showed that all components increased in concentration at the expense of C-C, and an additional component COO appeared at 289.9 eV. Similarly, N 1s deconvoluted peaks are shown in **Fig. 4**b (as received powder) and **Fig. 4**d (plasma treated powder). In both cases, NH and NO were detected at 400.3 ± 0.3 eV, NO_2^- at 403.7 ± 0.3 eV, and NO_3^- at 407.4 ± 0.1 eV. The intensity of NO_3^- increased significantly after plasma treatment and was responsible for the higher total nitrogen content in the plasma treated powder. These findings agree with the TG/MS analyses and the literature data, where an increased presence of N has been reported after DCSBD treatment [118]. In the case of ceramic materials, DCSBD treatment of alumina powder showed similar changes in the carbon and nitrogen components adsorbed on the surface, as analysed by TG/MS and XPS [71].

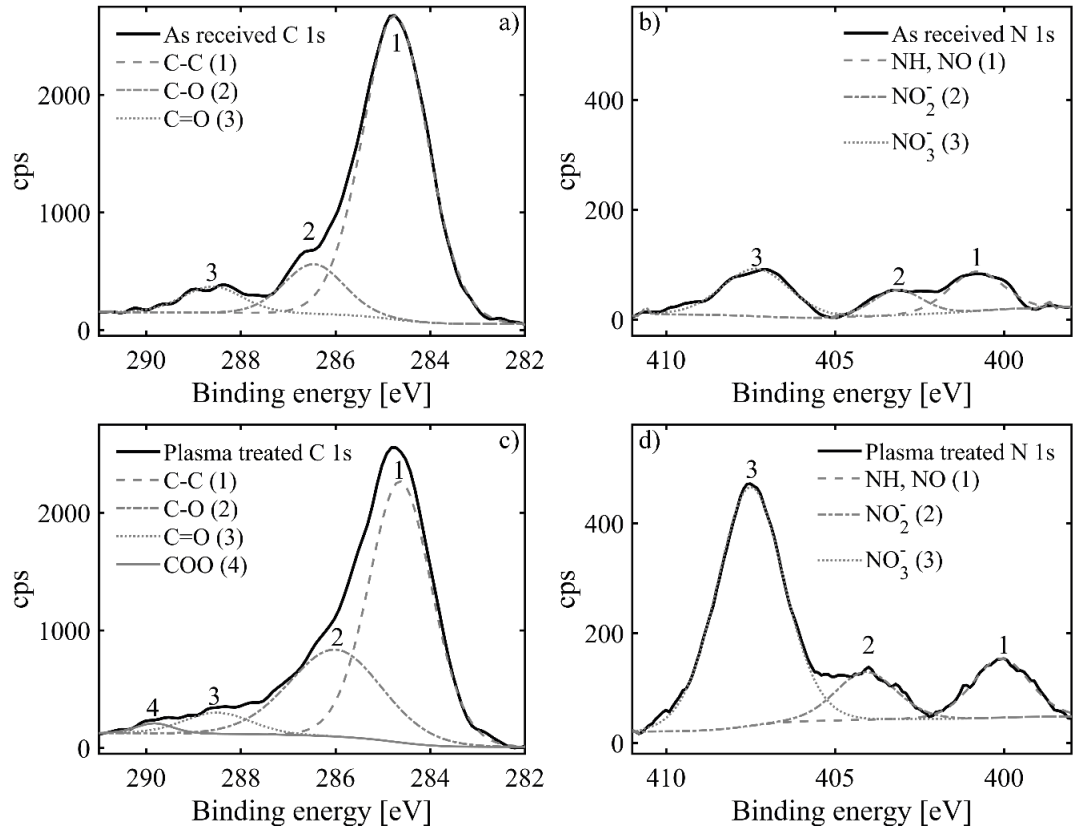

Fig. 4 Deconvoluted XPS spectra of C 1s and N 1s peaks for as received (a, b) and plasma treated (c, d) HA powders [121].

Electrophoretic deposition

The plasma treatment of the HA powder significantly affected its colloidal properties and the EPD process itself. **Table 2** summarises the information on the suspensions containing as received and plasma treated HA powders and the EPD process. The zeta potential of the suspension characterises its stability; suspensions with the zeta potential close to |30| mV can be considered stable and resistant to sedimentation and flocculation of particles [122]. The zeta potential of the suspension with as received powder changed from + 15.3 mV to – 15.2 mV after adding MCAA. The amount of MCAA was insufficient to stabilise the suspension, but the use of higher concentrations could cause problems in the intended application of orthopaedic implants (toxicity, corrosion). Therefore, the work aimed to establish the feasibility of DCSBD treatment to stabilise suspensions for EPD. The presence of additional surface components

in the plasma treated HA powder increased the stability of the suspension and the zeta potential to + 24.7 mV in the suspension without MCAA.

Unstable suspensions also had fewer charge carriers, resulting in low electrical conductivity. This resulted in abrupt cathodic deposition, as shown by the steep curve in **Fig. 5**a. The deposition had to be terminated prematurely due to approaching the limits of the power source. 0.85 wt.% of MCAA increased the electrical conductivity, but the near-zero zeta potential inhibited any deposition. A further increase in MCAA content to 12.75 wt.% resulted in higher conductivity, negative zeta potential, and anodic deposition. The conductivity was still insufficient, and the deposition had to be terminated after 25 min due to the high deposition rate and subsequent development of cracks in the deposit caused by non-optimal particle packing on the electrode [123]. The plasma treated HA powder contained increased amounts of carbon and nitrogen components, which are soluble in the 2-propanol [124–127]. The increased amount of charge carriers increased the electrical conductivity by two orders of magnitude and reduced the rate of cathodic deposition (**Fig. 5**a, dotted line). The addition of MCAA increased the conductivity but also decreased the zeta potential and prevented deposition.

Table 2 MCAA concentration, electrical conductivity, zeta potential, and deposition process [121].

Powder	MCAA [wt.%]	Zeta potential [mV]	El. conductivity [µS/cm]	Deposition process
As	0	15.3	0.1	Cathodic, abrupt
received	0.85	2.7	0.5	None
	12.75	-15.2	5.2	Anodic, cracking
Plasma	0	24.7	38.5	Cathodic, uniform
treated	0.85	16.1	66.6	None
	12.75	10.5	75.3	None

Due to the undesirable behaviour of suspensions with added stabilisers during the EPD, only deposits prepared without any MCAA were further analysed. Unsuitable properties of suspensions with as received HA powder led to abrupt deposition, which resulted in a non-uniform 4 mm thick deposit (**Fig. 5**b) with $R_a = 127.3 \pm 17.5$ µm, $R_z = 461.7 \pm 43.1$ µm. In contrast, stabilised deposition of plasma treated HA powder produced a crack-free, smooth, and uniform deposit with $R_a = 8.2 \pm 2.7$ µm, $Rz = 28.2 \pm 7.7$ µm (**Fig. 5**c), and a thickness of ~1 mm. Controlled deposition of plasma treated HA powder not only produced smoother and crack-free deposits but also enabled better particle packing on the electrode. Deposits were denser, reaching 27.6% of TD compared to 22.4% of TD for as received HA deposits.

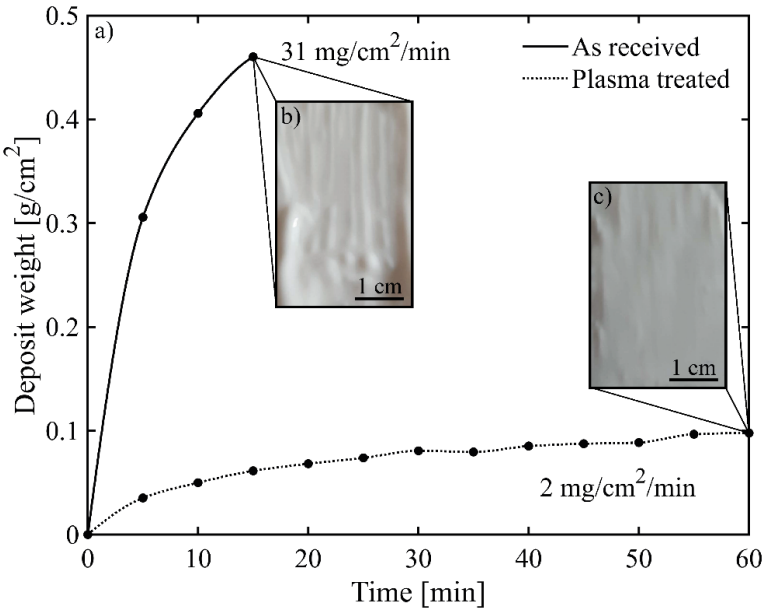

Fig. 5 Deposition yields (a) and photographs of as received (b) and plasma treated (c) HA coatings [121].

Sintering and densification

The deposits removed from the electrodes were sintered using multiple sintering cycles with different sintering temperatures, dwell times, and heating rates. **Table 3** summarises the sintered samples' relative densities and MGS depending on the used sintering cycle. It is apparent that a higher heating rate resulted in a better final density of the coatings. The benefits of high heating rates for densification can be explained by surface diffusion inhibition [89], early activation of lattice and GB diffusion [88], and densification front formation [90]. A dwell time of 10 min at the sintering temperature was sufficient to densify the coating homogeneously and no densification front was observed. At the sintering temperature of 1100 °C, the density ranged from less than 40% of TD (5 °C/min) to more than 52% of TD (100 °C/min) for the coatings prepared from the plasma treated HA powder. The as received powder coatings had slightly lower final densities. The most significant effect of different heating rates was observed at the 1200 °C sintering temperature. Plasma treated HA deposits were densified up to 94.7% of TD (100 °C/min), whilst as received HA deposits were typically 5–10% more porous. At the highest sintering temperature (1300 °C), high heating rates were no longer beneficial as all sintering regimes densified the samples well above 90% of TD. In all cases, the plasma treated coatings retained their higher density after sintering. The maximum density of 97% of TD was recorded for the plasma treated deposit sintered at 100 °C/min.

This value is similar to other reports using pressureless sintering of commercial HA powder with comparable particle size, morphology, and purity at this temperature [128,129].

The slowest sintering cycles with a heating rate of 5 °C/min and 120 min dwell time were designed to mimic the conventional sintering process. The samples were inserted into the furnace chamber, which was gradually heated to the sintering temperature, so there was a negligible temperature difference between the chamber and the sample. In the case of RPLS cycles, the furnace chamber was preheated 100 °C above the desired sintering temperature from the start. The temperature difference was much higher, and the amount of heat transferred during sintering increased because the amount of transferred radiation energy is proportional to the temperature difference between the radiation source and the sample to the power of four [90]. This could explain the higher densities of the RPLS samples even at shorter dwell times (10 vs 120 min). In addition, the conventional-like sintering cycle was more than 17 times longer than the shortest RPLS cycle, which was comparable to SPS [130] or microwave sintering [91].

Table 3 Relative densities (ρ) and MGS depending on the sintering cycle [121].

Sintering temp. [°C]	Heating rate [°C/min]	Dwell [min]	ρ [%]		MGS [µm]	
			Ref[a]	Plasma[b]	Ref[a]	Plasma[b]
1300	100	10	94.4 ± 0.3	97.0 ± 0.1	1.9 ± 0.2	1.9 ± 0.3
	50		93.7 ± 0.2	94.7 ± 0.1	2.0 ± 0.1	2.0 ± 0.3
	20		93.5 ± 0.1	95.0 ± 0.1	2.2 ± 0.2	2.1 ± 0.3
	5		93.3 ± 0.1	95.2 ± 1.0	2.9 ± 0.3	3.2 ± 0.4
	5	120	92.2 ± 0.1	94.7 ± 0.1	2.5 ± 0.3	2.5 ± 0.3
1200	100	10	87.0 ± 0.1	94.7 ± 0.1	1.0 ± 0.1	1.0 ± 0.1
	50		83.0 ± 0.1	86.8 ± 0.1	1.0 ± 0.1	1.0 ± 0.1
	20		71.6 ± 0.1	76.3 ± 0.1	0.9 ± 0.1	0.9 ± 0.2
	5		65.1 ± 0.1	75.5 ± 0.1	1.0 ± 0.1	1.0 ± 0.1
	5	120	61.1 ± 0.1	66.7 ± 0.1	1.1 ± 0.1	1.0 ± 0.2
1100	100	10	49.6 ± 0.2	52.6 ± 0.1	0.4 ± 0.1	0.4 ± 0.1
	50		46.1 ± 0.1	50.8 ± 0.1	0.4 ± 0.1	0.4 ± 0.1
	20		42.7 ± 0.1	45.6 ± 1.0	0.5 ± 0.1	0.4 ± 0.1
	5		40.0 ± 0.1	44.0 ± 0.1	0.5 ± 0.1	0.5 ± 0.1
	5	120	39.0 ± 0.1	39.8 ± 0.1	0.5 ± 0.1	0.5 ± 0.1

[a] produced from as received HA

[b] produced from plasma treated HA

Microstructure

Different sintering trajectories between the plasma treated and as received powder coatings and different sintering cycles resulting in different densities did not significantly affect the MGS (**Table 3**). This contrasts with previous reports for plasma treated alumina powder consolidated by EPD [71], slip-casting [131] and dry pressing [6]. The MGS gradually increased with increasing sintering temperature from 0.5 µm, to 1 µm, to 2–3 µm, for 1100 °C, 1200 °C, and 1300 °C, respectively. RPLS produced dense samples with finer microstructures than conventionally sintered [129] or microwave-sintered [132] hydroxyapatite. A finer microstructure is beneficial as increased surface energy, mechanical properties, and osteoblast activity have been reported for HA with finer grains [133].

Phase composition

Further benefits may arise from the fact that different powder treatment and sintering regimes of the deposits did not affect the phase composition and only pure HA (#ICSD 026204) was identified. Preserved HA is advantageous for the intended use in orthopaedic coatings as it is stable in the physiological environment [134] and increases osteoblast activity [135,136]. The high stability of HA, even at 1300 °C, is surprising but has been reported previously [119,120,137–141]. This can be explained by the used powder, its morphology, and purity. Overall, the results showed that selected processing methods allow tailoring of the final density and MGS whilst maintaining the phase composition, which offers interesting possibilities for coatings on orthopaedic screws.

Coating of orthopaedic screws

As a demonstration, orthopaedic screws were coated with HA using the same settings but with a shorter deposition time to obtain an optimum thickness between 50–100 µm [142]. The rapid deposition of the as received HA powder resulted in a non-uniform coating with visible cracks, as shown in **Fig. 6**a. This is consistent with previous papers related to EPD of HA on orthopaedic coatings reporting several challenges such as cracking, non-uniformity, and poor coating adhesion even after optimising the deposition [143–145]. Thermal spraying methods were more successful, but high temperatures during deposition reduced crystallinity or caused phase transformations to other calcium phosphates [146,147]. On the other hand, the deposition from plasma treated HA powder produced a uniform, crack-free coating, as shown in **Fig. 6**b. This result demonstrates the viability of plasma treatment for regenerative medicine applications.

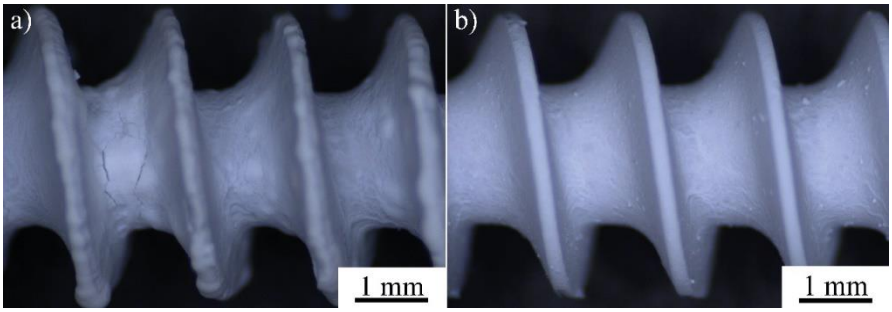

Fig. 6 HA biocoatings on stainless steel orthopaedic screws fabricated by EPD from suspensions containing a) as received powder and b) plasma treated powder [121].

Conclusions of the sub-chapter

This sub-chapter has investigated the suitability of plasma activation of HA powder to produce uniform, defect-free coatings by EPD without hazardous or toxic additives. Adsorbed nitrogen and carbon components positively influenced the suspension properties and the EPD process. RPLS enhanced the benefits of plasma treatment of the powder as these coatings had higher final densities. Finally, the benefits of plasma treatment for producing biocoatings by EPD were directly demonstrated on orthopaedic screws. The results were published in the Journal of the European Ceramic Society (Q1, ref [121]).

5.2 Aluminium tungstate calcination and sintering

This sub-chapter focuses on optimising processing of another advanced oxide ceramic material: thermomiotic $Al_2W_3O_{12}$. Discussed topics include amorphous powder synthesis, investigating extrinsic point defects introduced by calcination, and the improvement of $Al_2W_3O_{12}$ densification by rapid sintering methods (RPLS, SPS). The co-precipitation method was used to synthesise amorphous $Al_2W_3O_{12}$ powder with small primary particles, and agglomerates were broken down by planetary ball milling. The powder was calcined at 500–620 °C, and the influence of the selected temperature was described in terms of crystalline structure and induced point defect concentration. The calcined powder was analysed using high-temperature dilatometry, which established ideal sintering conditions for RPLS and SPS techniques. Sintered $Al_2W_3O_{12}$ samples were evaluated based on their density, microstructure, CTE, and mechanical properties.

Amorphous powder synthesis

The synthesis of nanosized and single-phase $Al_2W_3O_{12}$ powder is required to produce dense and fine-grained ceramic bodies. A solid-state reaction [148], sol-gel [61], and total evaporation techniques [21] have been used previously, but this work relied on co-precipitation due to its low cost and simple synthesis [21,60,61]. The co-precipitation was optimised by using different precursors, lower molarity, and no ageing time to prevent particle coarsening.

As a result, the produced amorphous powder had a specific surface area of 66.3 m^2g^{-1} and a calculated primary particle size of 18 nm, the finest powder reported in the literature to date [149]. However, the measurement of primary particles from SEM images showed slightly higher particle size in the range of 50–100 nm (see **Fig. 7**a). Also, substantial agglomeration of the powder was observed (see inset in **Fig. 7**a). The laser diffraction measurement resulted in a trimodal particle size distribution with peaks at 3, 13, and 60 μm and d_{50} = 35.8 μm (**Fig. 7**d).

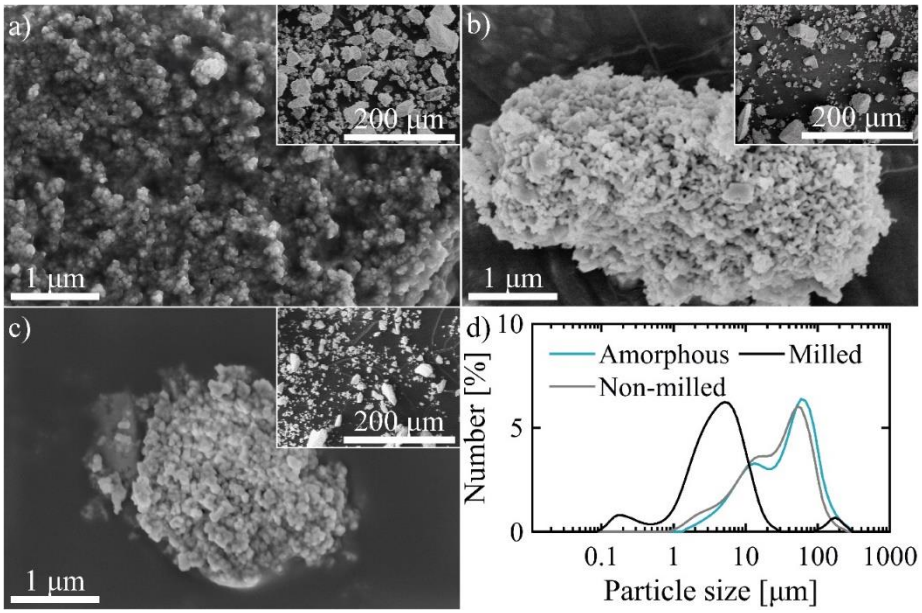

Fig. 7 SEM micrographs of a) amorphous, b) calcined non-milled, and c) calcined milled $Al_2W_3O_{12}$ powders with their particle size distributions (d) [150].

TG and DSC analyses

The amorphous powder was subjected to simultaneous TG and DSC analyses from room temperature to 800 °C in air (**Fig. 8**). The curves suggest two significant events during heating. The endothermic event and the rapid weight loss at lower temperatures, centred at 122 °C, were related to water release and evaporation. The weight loss above 175 °C is due to the release of hydroxyl groups [151–154] originating from the hydroxide-based precursors [152]. A total weight loss of 18.7% was recorded, but the weight loss above 570 °C was negligible, suggesting that structural changes were complete. This contrasts with the DSC curve, which shows a second major exothermic event, the crystallisation of $Al_2W_3O_{12}$ [149], centred around 635 °C with onset at 615 °C.

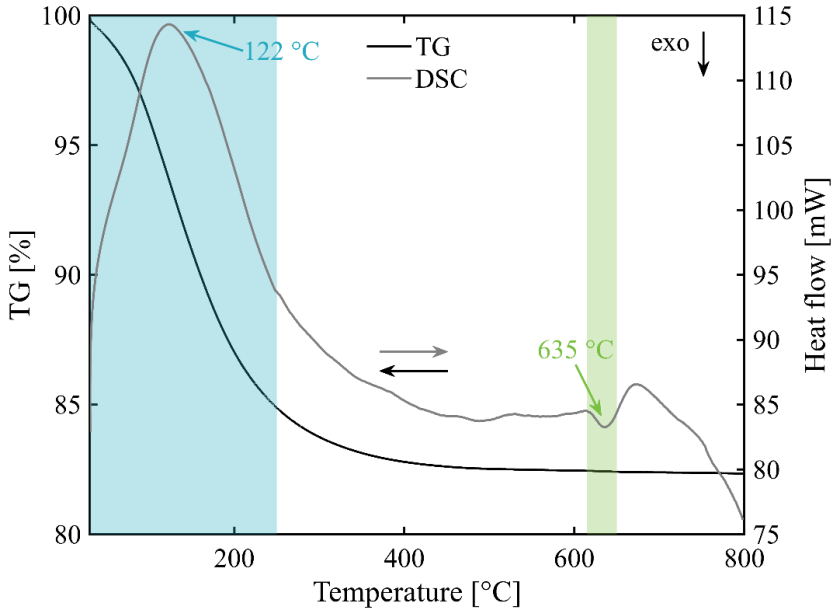

Fig. 8 Simultaneous TG and DSC curves of amorphous $Al_2W_3O_{12}$ powder, with marked water evaporation (cyan underpainting) and crystallisation (green underpainting) events. Note the downward orientation of the exothermic DSC peaks [155].

XRD of calcined powders

Based on the TG/DSC data, the amorphous powder was calcined at temperatures between 500 and 620 °C in the RPLS furnace with a 20 min dwell time. The XRD patterns in **Fig. 9** show that the amorphous precursor (black pattern) showed no diffraction peaks, only an amorphous halo. Diffraction peaks started to appear at higher temperatures, and orthorhombic $Al_2W_3O_{12}$ became dominant at 540 °C (orange pattern). XRD patterns show that a lower temperature under isothermal conditions may be sufficient for crystallising the synthesised amorphous $Al_2W_3O_{12}$ than suggested by the exothermic DSC peak centred at 635 °C (see **Fig. 8**). Pawley method refinement for powders calcined at 540, 570, and 620 °C showed that lower calcination temperatures resulted in 0.36% (540 °C) and 0.18% (570 °C) volumetric expansion of the unit cell compared to the 620 °C calcined powder. This could indicate an increased concentration of point defects in the crystalline structure.

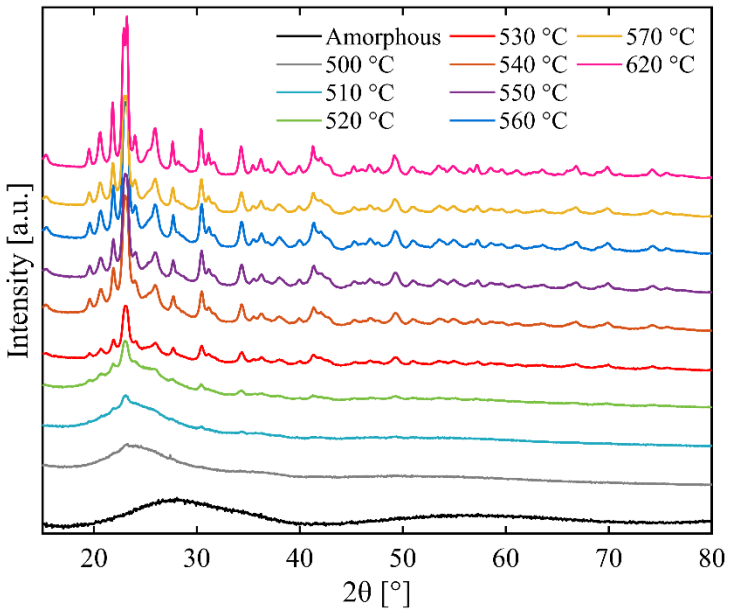

Fig. 9 XRD patterns of amorphous $Al_2W_3O_{12}$ powder and powders calcined at 500–620 °C [155].

Raman spectroscopy of calcined powders

Raman spectroscopy was used to study the vibrational characteristics of the calcined powders, the presence of point defects, and the associated unit cell expansion. Several vibrational bands were identified. Small intensity peaks between 150–300 cm^{-1} (**Fig. 10**, cyan underpainting) were associated with translational and lattice vibrations of WO_4 tetrahedra (ν_2), peaks between 300–450 cm^{-1} (**Fig. 10**, green underpainting) were attributed to O–W–O bending modes in WO_4 (ν_4), double peaks in the range of 800–950 cm^{-1} (**Fig. 10**, red underpainting) were associated with W–O asymmetric stretching vibrations of WO_4 tetrahedra (ν_3), and the most intense peak in the region of 950–1100 cm^{-1} belonged to W–O symmetric stretching vibrations (ν_1) [156–158].

The splitting of the main peak belonging to the ν4 band indicated a lower concentration of oxygen vacancies with increasing calcination temperature. The splitting was evident at 550 °C (**Fig. 10**, purple curve) and was most pronounced at 620 °C (**Fig. 10**, magenta curve). This phenomenon represents the strengthening of the O–W–O band due to the disappearance of oxygen deficiency in the crystal structure and has been reported for highly ordered $Al_2W_3O_{12}$ structures [156–158].

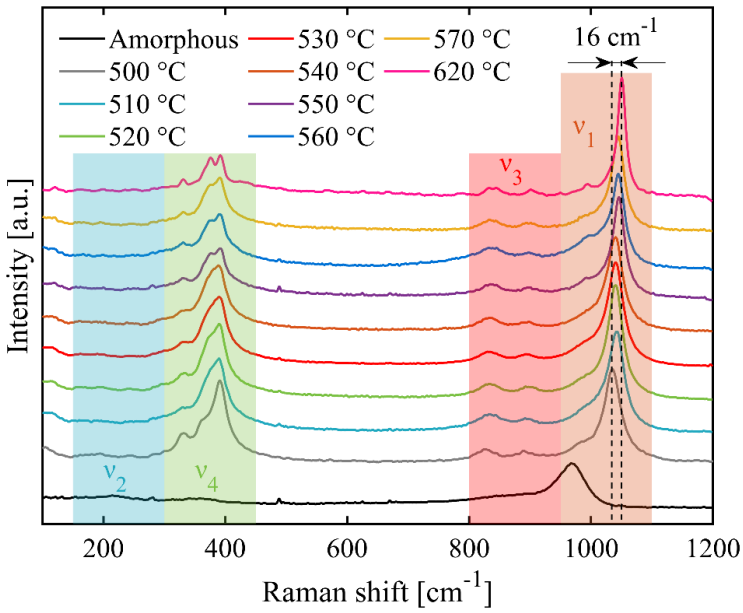

Fig. 10 Raman spectra of amorphous and calcined $Al_2W_3O_{12}$ powders with marked vibrational modes ν_1– ν_4 [155].

Dashed lines in the ν_1 symmetric stretching band region represent the redshift of the main peak towards the lower wavenumber with decreasing calcination temperature by 16 cm^{-1} (620 vs. 500 °C). The distortion in the local structure present in the 500 °C calcined powder could cause softening of the W–O bonds. On the other hand, the ordered structure of powder calcined at 620 °C with stronger bonds showed a shift towards higher wavenumbers [159].

Colour change of calcined powders

Another indication of the increased presence of point defects, namely oxygen vacancies, is the colour change of the powder sample. The sample colour changed from dark grey to almost white with increasing calcination temperature (**Fig. 11**). $A_2M_3O_{12}$-type materials are wide-band-gap semiconductors that do not absorb visible light [159–161]. It has previously been shown that when $Al_2W_3O_{12}$ is reduced in an H_2 atmosphere at 400 °C, the powder becomes dark grey compared to defect-free $Al_2W_3O_{12}$ calcined at 800 °C [159]. The amorphous powder was utterly white, suggesting little or no oxygen vacancies. Therefore, the EPR technique, which allows direct measurement of extrinsic defects, was applied.

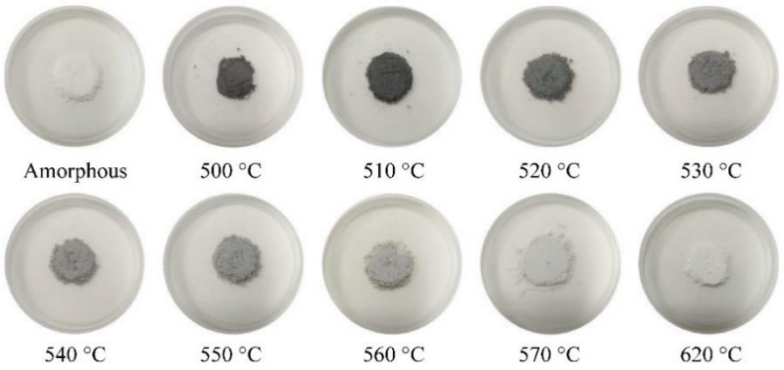

Fig. 11 Photographs of amorphous and calcined $Al_2W_3O_{12}$ powders [155].

EPR of calcined powders

As a definitive proof of the presence of oxygen vacancies in the calcined $Al_2W_3O_{12}$ powders, their paramagnetic signal was measured by EPR (**Fig. 12**). The paramagnetic signal detected at g = 2.0026 was attributed to a single electron trapped in the oxygen vacancy (SETOV) [151]. It can be seen that the concentration of SETOV increased with decreasing calcination temperature and reached its maximum in the powder calcined at 500 °C: $6.66 \cdot 10^{17}$ cm^{-3}. Calcination at 570 °C resulted in a 20-fold lower concentration of oxygen vacancies. The amorphous powder was completely free of oxygen vacancies, as suggested by its white colour, and the powder calcined at 620 °C had a negligible concentration.

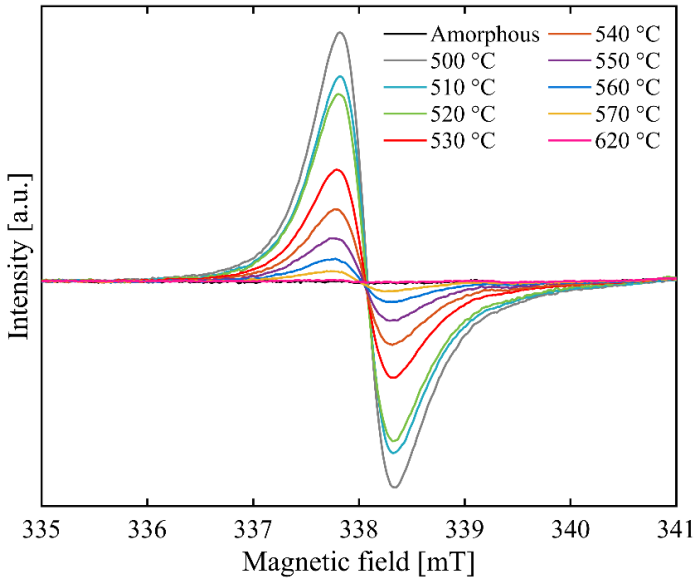

Fig. 12 EPR signals of amorphous and calcined $Al_2W_3O_{12}$ powder in air between 500 and 620 °C [155].

Powder milling and consolidation

Thorough analyses of calcined powders provided valuable information on the ideal calcination temperature for further processing steps, considering the need for nanometric crystalline orthorhombic $Al_2W_3O_{12}$. The selected calcination temperature of 570 °C was considerably lower than previously reported (650 °C) [149]. After calcination, the specific surface area was reduced to 26.4 $m^2 \cdot g^{-1}$ (from 66.3 $m^2 \cdot g^{-1}$) and the calculated primary crystallite size increased to 45 nm. **Fig. 7**d depicts the trimodal particle size distribution measured by laser diffraction with d_{50} = 29.9 μm. The SEM observation in **Fig. 7**b confirms the presence of agglomerates and primary particle size in the 50–100 nm range.

Planetary ball milling was used to break up agglomerated particles and improve particle packing during consolidation. A relatively brief time of 10 min was used to minimise the risk of contamination from the zirconia milling balls. **Fig. 7**d shows that the particle size distribution sifted to lower values with d_{50} = 3.9 μm. However, the distribution was still trimodal with a preserved small fraction of large agglomerates around 200 μm. A similar result has been reported for nanosized $Al_2W_3O_{12}$ [21] and can be explained by reagglomeration during milling [162]. In addition, a new particle size fraction centred around 100 nm was detected.

The SEM image of the agglomerate in the milled powder (**Fig. 7**c) shows that the primary particles remained in the range of 50–100 nm. The inset in **Fig. 7**c confirms that the majority of the large agglomerates were fragmented during the milling process, which could prevent shaping-related defects in compacted green bodies [163]. Finally, the specific surface area of the milled and calcined $Al_2W_3O_{12}$ powder increased to 31.4 $m^2\ g^{-1}$, the highest value reported to date [149].

After the consolidation by uniaxial pressing followed by CIP at 700 MPa, the relative densities of green bodies were 64.4% and 66.4% of TD for non-milled and milled powder, respectively. A small benefit of milling is evident, and the relative densities of the green bodies fell within the range of 58–73% of TD previously reported [21,60,164].

Sintering and densification

High-temperature dilatometry determined the ideal sintering temperature for green body densification. **Fig. 13**a shows the shrinkage (dashed curves) and its first derivative (solid curves) as a function of temperature. The shrinkage curves show that slight densification began around 590 °C (for both

powders), followed by a rapid shrinkage starting at around 810 °C (non-milled powder) and 830 °C (milled powder) and finished just below 1000 °C. The first derivative curve of the shrinkage, i.e., the shrinkage rate, contained three regions of interest (**Fig. 13**a). A broad downward peak centred at 640 °C was detected in the low-temperature region (cyan underpainting). This could be related to the completion of crystallisation, as previously suggested by the DSC measurement (**Fig. 8**), where an exothermic event occurred at 635 °C [150]. A sharp peak was detected in the following green region at 750 °C (non-milled powder) and 790 °C (milled powder), which can be attributed to the necking of the powder particles and pore channel smoothening [60,165]. The final high-temperature region (red underpainting) contains dominant peaks at 950 and 970 °C for non-milled and milled powder, respectively. This is the final stage of sintering with densification by lattice and GB diffusion [166]. Based on the dilatometric data, a sintering temperature of 1000 °C was selected for further experiments using SPS and RPLS.

The shrinkage curves recorded during SPS (see **Fig. 13**b) show that both powders were already densified at a lower temperature of 850 °C due to the applied pressure, which drives the mass transport [80]. Therefore, SPS samples were prepared at 850 and 1000 °C (for comparison with RPLS) sintering temperatures.

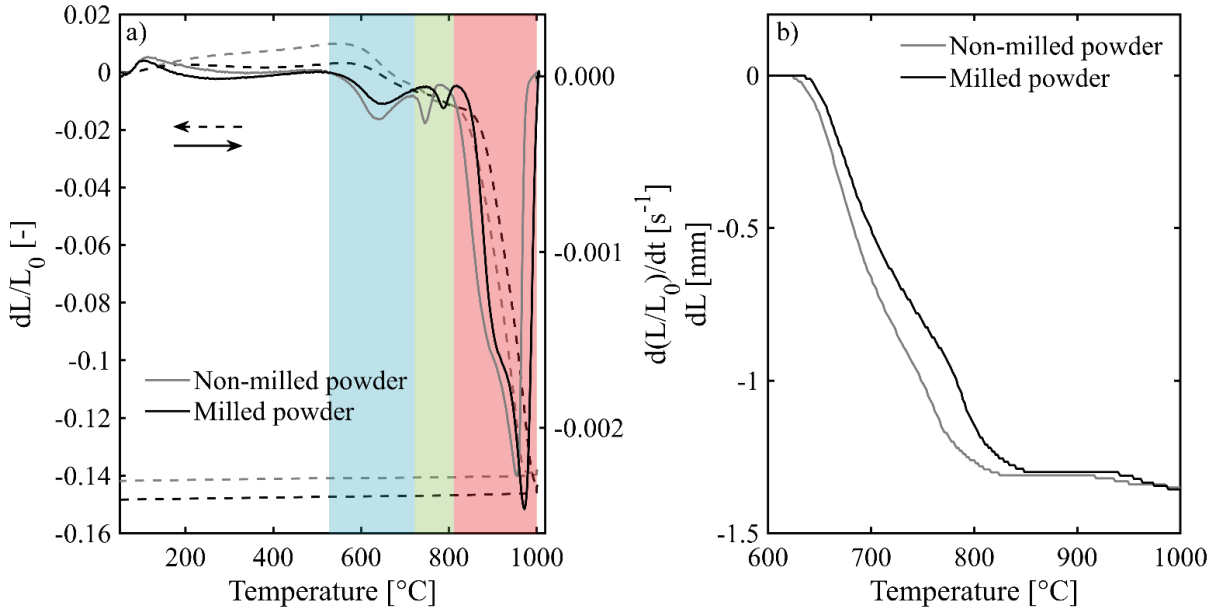

Fig. 13 Relative shrinkage and shrinkage rate curves with underpainted regions of interest (a) and absolute shrinkage measured during the SPS process (b) of non-milled and milled $Al_2W_3O_{12}$ powders [150].

RPLS samples achieved relative densities of 95.5–96.0% of TD regardless of the sintering regime used, as documented in **Table 4**. Similar densification compared to prolonged three-step sintering [60] can be explained by the acting of driving forces associated with the high heating rates, namely the surface diffusion inhibition [89], early activation of lattice and GB diffusion [88], and densification front formation [90], as mentioned in sub-chapter 5.1. The SPS samples surpassed the RPLS and the previous SPS report [60] by reaching relative densities close to 98.0% of TD at a much lower sintering temperature of 850 °C. Slightly lower densities were obtained at 1000 °C. The overall results confirmed the benefits of optimised powder synthesis and calcination, as the sintering temperatures were significantly lower and densification was higher than previous reports dealing with pressure-less sintering [21,60] and SPS [60].

Table 4 Summary of relative densities, Vickers hardness, and Young's modulus of the samples prepared from non-milled and milled powders using RPLS and SPS [150].

Sintering method	Sintering temp. [°C]	Dwell [min]	Powder condition	ρ [% of TD]	HV0.1 [GPa]	E [GPa]
RPLS	1000	10	Milled	95.6 ± 0.3	3.8 ± 0.4	46.8 ± 4.5
			Non-milled	95.5 ± 0.3	3.9 ± 0.5	45.4 ± 1.8
		60	Milled	96.0 ± 0.2	3.9 ± 0.6	42.8 ± 3.5
			Non-milled	95.7 ± 0.3	3.9 ± 0.4	45.9 ± 3.4
SPS	850	2	Milled	97.8 ± 0.1	6.9 ± 0.5	64.0 ± 3.3
			Non-milled	97.7 ± 0.1	6.4 ± 0.3	62.3 ± 2.2
	1000	2	Milled	97.5 ± 0.3	4.0 ± 0.6	51.7 ± 2.7
			Non-milled	97.1 ± 0.2	3.8 ± 0.6	44.7 ± 2.2

Phase composition of sintered bodies

After densification, the phase compositions of sintered bodies were investigated using the XRD analysis. Diffractograms confirmed the presence of monophasic orthorhombic $Al_2W_3O_{12}$ [114], irrespective of the sintering method or temperature. **Fig. 14** shows the XRD patterns of sintered samples from non-milled powder densified by RPLS and SPS (850 and 1000 °C).

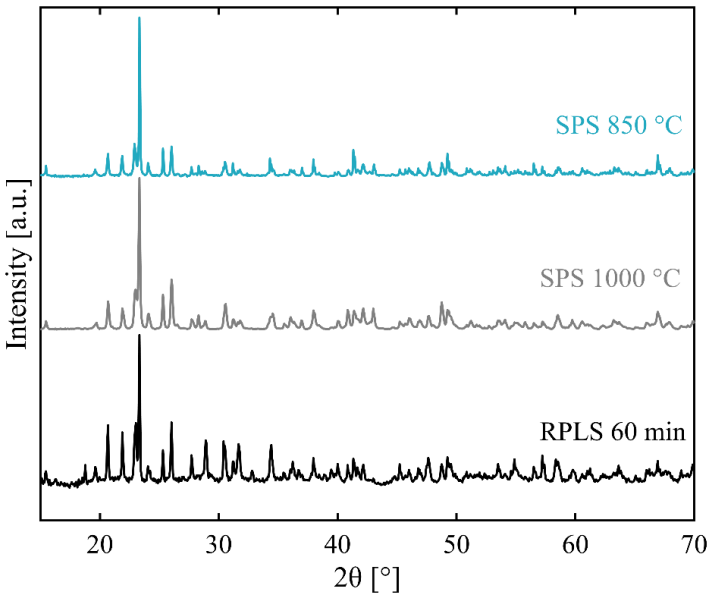

Fig. 14 XRD patterns of samples sintered by RPLS and SPS [150].

Microstructure

The microstructure of sintered samples was studied by SEM to investigate the influence of selected sintering methods on grain size and microcracking. **Fig. 15**a shows a representative microstructure of the RPLS samples. Coarse elongated grains 50 to 150 μm in length contained intragranular pores and several microcracks (white arrows) and were surrounded by larger intergranular porosity. SPS samples sintered at 1000 °C (**Fig. 15**b) also contained coarse elongated grains with microcracks (white arrows) and some intragranular pores. Nevertheless, clusters of the original fine particles were still present. The tendency for abnormal grain growth (AGG) has been observed mainly for nanometric starting powders at temperatures as low as 800–900 °C [167,168], which could explain the current results. However, other reports demonstrated finer microstructures even at temperatures above 1000 °C [21,60]. The mentioned microcracking was caused by the CTE anisotropy of $Al_2W_3O_{12}$ [21], which was facilitated by coarse and elongated grains. The lower sintering temperature of 850 °C preserved a finer microstructure that prevented microcracking, and only submicron grains (~400 nm) were observed (**Fig. 15**c, note the different scale bar). Obtaining dense, fine-grained, and crack-free microstructure is crucial for possible application of thermomiotic ceramic materials in applications requiring resistance to thermal shock.

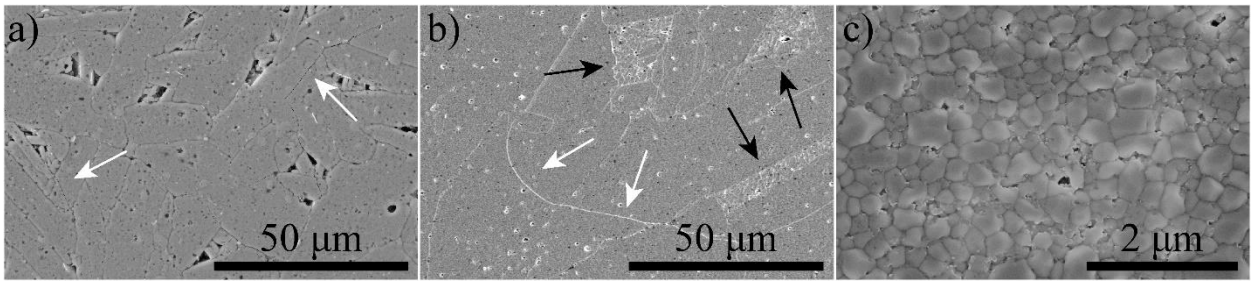

Fig. 15 SEM micrographs of $Al_2W_3O_{12}$ samples from milled powder sintered by a) RPLS with 10 min dwell time, b) SPS at 1000 °C, and c) SPS at 850 °C (note the different scalebar). White arrows indicate microcracks, and black arrows mark preserved clusters of finer grains [150].

Due to the non-circular grain shape in some samples, the grain area appears to be a better indicator of the state of the microstructure than the grain size. **Fig. 16** shows the cumulative count of grain area in all sintered samples. RPLS samples contained submicron grains up to coarse grains with areas of hundreds of µm^2 in cross-section, as shown by SEM (**Fig. 16**a). A shorter dwell time and milling of the powder before sintering resulted in a slightly finer microstructure (curves are shifted to the left). The clustered microstructure of the SPS sample sintered at 1000 °C is represented by a significant fraction of grains below 10 µm^2 with a small fraction of abnormal grains above 100 µm^2. The SPS sample sintered at 850 °C had a narrow microstructure with fine grains well below 1 µm^2.

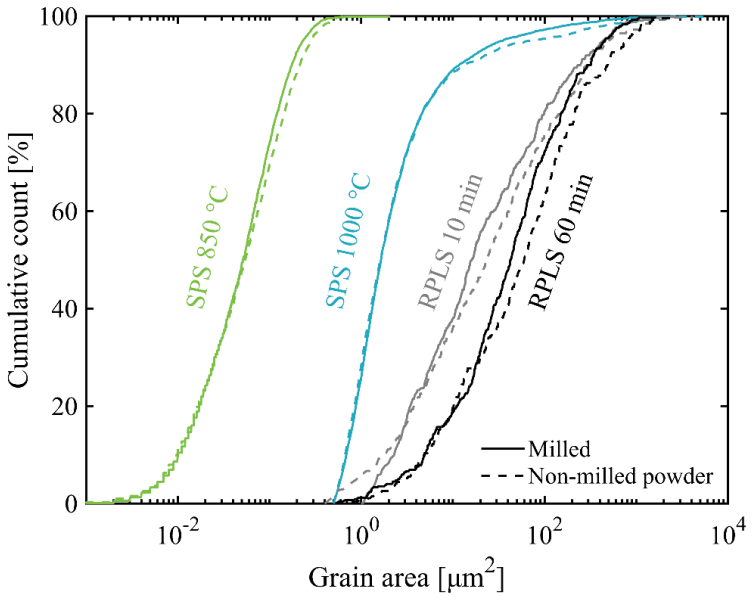

Fig. 16 Cumulative grain area distributions of sintered $Al_2W_3O_{12}$ samples [150].

Coefficient of thermal expansion

Dense ceramic bodies with near-zero CTE were one of the main objectives of this sub-chapter. The CTE of selected RPLS and SPS samples was measured and calculated according to Equation 1 in the direction of the applied pressure during uniaxial pressing or sintering (*z*-axis) and perpendicular to it (*x*-, *y*-axes). Both measured RPLS samples had CTEs between $1.2 \cdot 10^{-6}$ K^{-1} and $1.9 \cdot 10^{-6}$ K^{-1} (**Table 5**), and there was no apparent significant difference between the measurement directions. The CTE values agree with previous reports for polycrystalline [21,60] and single crystal $Al_2W_3O_{12}$ [169]. Both SPS samples showed a significant difference between *z* and *x, y* CTE, especially after sintering at 1000 °C. Abnormal and elongated grains in the microstructure resulted in CTE in the *x, y* direction of $6.2 \cdot 10^{-6}$ K^{-1}. This value was in agreement with the reports of polycrystalline $Al_2W_3O_{12}$ between $6.0 \cdot 10^{-6}$ K^{-1} [114] and $6.6 \cdot 10^{-6}$ K^{-1} [159] in the *a*-axis direction in the *Pbcn* space group and even approached the single crystal CTE ($8.3 \cdot 10^{-6}$ K^{-1}) in the *a*-axis direction [169]. The lower *x, y* CTE agrees with the *b*- and *c*-axis CTE of a single crystal [169]. The smaller CTE difference in the SPS sample sintered at 850 °C was probably due to the absence of abnormal and elongated grains in the microstructure.

Table 5 CTEs of selected samples measured in z-axis (direction of applied pressure during uniaxial pressing or SPS) and along x-, y-axes (direction perpendicular to applied pressure) [150].

Sample	CTE [$\cdot 10^{-6}$ K^{-1}]
RPLS-milled-60 min-*z*	1.6
RPLS-milled-60 min-*xy*	1.2
RPLS-non-milled-60 min-*z*	1.7
RPLS-non-milled-60 min-*xy*	1.9
SPS-milled-850 °C-*z*	4.2
SPS-milled -850 °C-*xy*	2.2
SPS-milled-1000 °C-*z*	6.2
SPS-milled-1000 °C-*xy*	1.4

Mechanical properties

Finally, the evaluation of mechanical properties also demonstrated the differences between selected sintering techniques in terms of the material's performance. The Vickers hardness HV0.1 and Young's modulus obtained from an instrumented hardness testing machine are given in **Table 4**. The HV0.1 of the RPLS samples ranged from 3.8 to 3.9 GPa, and Young's modulus was between 42.8 and 46.8 GPa. Due to their similar microstructures, the SPS sample sintered at 1000 °C had mechanical properties similar to those of the RPLS samples. However, the lower sintering temperature of 850 °C during SPS yielded fine

grain samples and consequently, their mechanical properties improved due to the Hall-Petch effect [170]. HV0.1 reached 6.9 GPa, and Young's modulus 64.0 GPa.

Conclusions of the sub-chapter

$Al_2W_3O_{12}$ ceramics have been produced with the highest density to date. This was achieved by optimising powder synthesis, calcination temperature, milling, and sintering. Co-precipitation yielded high-purity amorphous powder with a large surface area. Different calcination temperatures resulted in $Al_2W_3O_{12}$ powders with various levels of structural order and oxygen vacancy content. Planetary ball milling of the calcined powder slightly increased the surface area and removed most of the agglomerates, resulting in a higher density of the green bodies. The RPLS and SPS were used to densify the samples up to 98% of TD. The different state of the microstructure based on the selected sintering temperature influenced the mechanical properties. The best performance was recorded for fine-grained samples produced by SPS at 850 °C, showcasing possible processing conditions for production of thermomiotic materials for advanced applications. The study of oxygen vacancies in the calcined powders was published in The Journal of Physical Chemistry C (Q1, ref [155]) and the rapid sintering study was published in the Journal of the European Ceramic Society (Q1, ref [150]).

5.3 Microstructural evolution of barium titanate under non-conventional sintering conditions

This sub-chapter examines the microstructural evolution of $BaTiO_3$ densified by RPLS and radiation-assisted sintering, two rapid sintering methods without applied pressure. Dry-pressed green body samples were sintered at different sintering temperatures with a heating rate of 100 °C/min and dwell times of 5 and 15 min in RPLS and radiation-assisted sintering, respectively. The samples were evaluated in terms of microstructure and density.

Rapid pressure-less sintering

The microstructural evolution of barium titanate is an important topic because its dielectric and piezoelectric properties strongly depend on the grain size [39,40]. It is known that barium titanate tends to undergo abnormal grain growth, where the GB mobility of some grains is significantly higher [171] and AGG can occur in a relatively narrow temperature window [172]. **Table 6** documents that no abnormal grains were visible in the sample sintered at 1200–1210 °C. With increasing sintering temperature, the proportion of abnormal grains in the microstructure increased to ~10, 60, and 95% for 1220, 1230, and 1240 °C, respectively. SEM micrographs show the microstructure of the 1220 °C sample (**Fig. 18**a). White arrows indicate several clusters of abnormal grains. Black arrows in the sample sintered at 1240 °C in **Fig. 18**b indicate remaining clusters of fine grains. Most of the AGG was thus concentrated in the narrow temperature range 1220–1240 °C, whilst the original fine grain population remained below 1 µm. Non-Arrhenius behaviour of some grain boundaries, probably caused by small structural and stoichiometric deviations, led to unrestricted grain growth until the abnormal grains started to impinge on each other [172]. At higher sintering temperatures above 1250 °C, the microstructure reverted to normal grain growth and consisted only of ~35 µm coarse grains.

Table 6 MGS of fine grains, abnormal grains and share of abnormal grains in the microstructure as a function of sintering temperature and sintering method.

Sintering method	Sintering temperature [°C]	MGS of fine grains [µm]	MGS of abnormal grains [µm]	Abnormal grains share [%]
RPLS	1200	0.7 ± 0.1	-	0
	1210	0.7 ± 0.1	-	0
	1220	0.8 ± 0.1	18.0 ± 5.1	10
	1230	1.0 ± 0.1	37.3 ± 4.9	70
	1240	1.2 ± 0.1	24.8 ± 3.0	95
	1250	-	25.0 ± 3.6	99
	1300	-	35.1 ± 3.9	100
Radiation-assisted sintering	1325	1.2 ± 0.1	-	0
	1350	1.3 ± 0.1	32.0 ± 5.1	25
	1375	1.3 ± 0.1	39.4 ± 13.8	75
	1400	-	63.8 ± 10.3	100

The relative densities of RPLS samples were above 94% of TD even at the lowest sintering temperatures and reached ~98% of TD for samples sintered at 1200–1240 °C (see **Fig. 17**). These values are comparable to or exceed those reported for conventionally sintered $BaTiO_3$ without the applied pressure [41,52]. As discussed in sub-chapters 5.1 and 5.2, high heating rates are crucial for the densification-promoting mechanisms of surface diffusion inhibition [89], early activation of lattice and GB diffusion [88], and densification front formation [90]. With an increased sintering temperature of 1300 °C, the relative densities decreased to ~95% of TD. The occurrence of AGG could explain the decrease in density because GB moved faster than pores [173] and intragranular porosity increased [174].

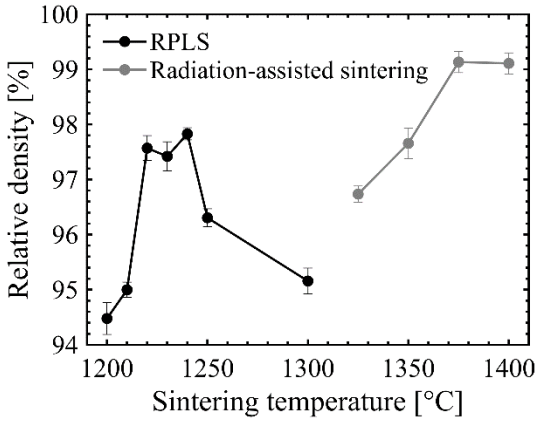

Fig. 17 Relative density as a function of sintering temperature for RPLS and radiation-assisted sintered $BaTiO_3$ samples.

Radiation-assisted sintering

Similar to the RPLS samples, the radiation-assisted sintered samples experienced AGG in a narrow temperature range starting at 1350 °C, as documented in **Table 6**. At the lower temperature of 1325 °C, only fine ~1.3 µm grain microstructure was present, which was gradually replaced by abnormal grains with increasing temperature (see **Fig. 18**c for 1375 °C sample), and at 1400 °C only coarse ~63 µm grain microstructure remained. At this high temperature, a secondary phase was observed at triple junctions of coarse grains, as indicated by cyan arrows in **Fig. 18**d. A wetting secondary phase at GB has been reported in titanates when heating above the eutectic temperature [175]. The eutectic temperature of 1332 °C of the $BaO\text{-}TiO_2$ system [176] was probably exceeded in the bulk sample, and Ti-rich higher barium titanate remained at GB after cooling.

Radiation-assisted sintering used higher temperatures than RPLS and obtained higher densities up to ~99% of TD at 1375 and 1400 °C. Relative densities of 72 and 91% of TD were measured in samples sintered at 1250 and 1300 °C, respectively (not shown here). This direct comparison with RPLS samples sintered at 1250 and 1300 °C showed significantly higher sample densification, probably due to the different temperature fields and, most importantly, the way of measuring the temperature during sintering. In RPLS, the thermocouple was directly next to the samples and the temperature could be precisely controlled. In contrast, in radiation-assisted sintering the pyrometer was aimed at the hole in the crucible and the temperature was measured on the inner wall of the crucible. Using shorter dwell times than 15 min for RPLS (as was the case of radiation-assisted sintering 5 min dwell) was disadvantageous as the experiments with 5 min dwell RPLS produced samples ~0.5% less dense than the 15 min dwell shown here.

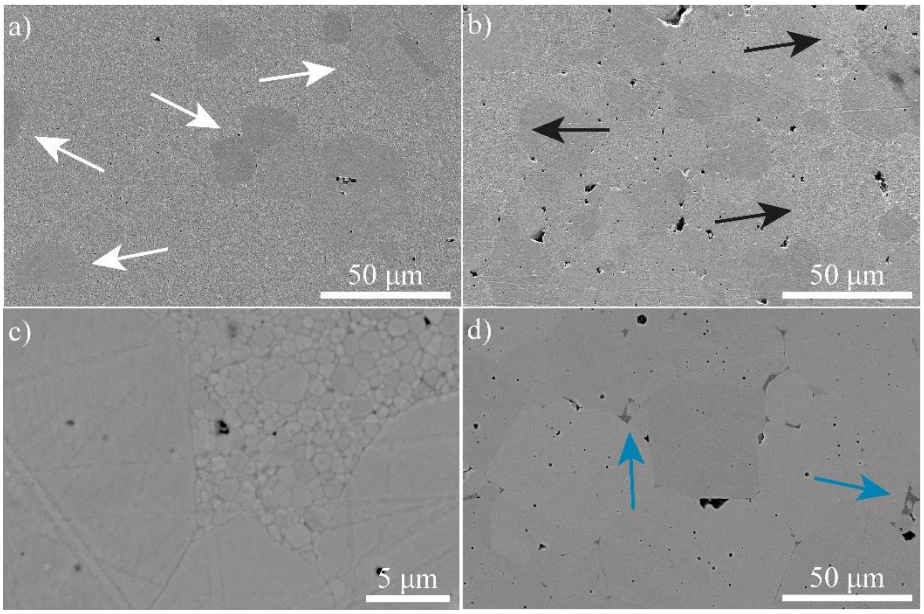

Fig. 18 SEM micrographs of $BaTiO_3$ a) sample sintered by RPLS at 1220 °C with white arrows indicating abnormal grains, b) sample sintered by RPLS at 1240 °C with black arrows indicating remaining fine grains, c) radiation-assisted sintered sample at 1375 °C (note different scalebar), and d) radiation-assisted sintered sample at 1400 °C with cyan arrows indicating secondary phase at triple points.

Conclusions of the sub-chapter

This sub-chapter describes the microstructural evolution and densification of $BaTiO_3$ under non-conventional rapid sintering methods, such as RPLS and radiation-assisted sintering. Abnormal grain growth was observed in both cases but at different temperature ranges. This was probably due to differences in heat transfer and the manner of temperature measurement. Dense $BaTiO_3$ samples were obtained by both methods, even when high heating rates and short dwell times were used. The knowledge gained in this sub-chapter could be useful for production of piezoceramic materials for advanced applications, using rapid sintering methods which require fraction of a time and energy compared to their conventional counterparts. It will also be used in the following sub-chapter, which focuses on fabricating $BaTiO_3$-based particle composites.

5.4 Barium titanate-based particle composites

This sub-chapter investigates the influence of the Al_2O_3 and ZrO_2 dielectric phases in the $BaTiO_3$ matrix on the mechanical and electrical performance of such composites. Mixed powders (3, 5, and 10 vol.% of reinforcing phase) were ball milled for 24 h to ensure good homogenisation. The powders were uniaxially pressed and CIPed, and pellets were sintered by RPLS with a dwell time of 15 min at 1250 °C and a heating rate of 100 °C/min. The sintered composites were characterised in terms of microstructure, phase composition, density, piezoelectric properties, and fracture toughness.

Microstructure

Overview and detailed SEM micrographs of pure $BaTiO_3$ standard and selected composite samples are shown in **Fig. 19**. Pure barium titanate (**Fig. 19**a,b) contained coarse grains (~25 µm) with large intergranular and small intragranular pores. The microstructure of Al_2O_3-reinforced $BaTiO_3$ (see **Fig. 19**c,d) consisted of fine grains (~0.5 µm) of two distinct phases containing heavier (brighter grains) and lighter elements (darker grains). In addition, small clusters of even brighter grains were observed at several points on the surface, as indicated by the white arrows. The microstructure of the ZrO_2-reinforced $BaTiO_3$ (see **Fig. 19**e,f) again consisted mainly of fine grains (~0.5 µm) with slightly varying shades of grey, indicating an inhomogeneous chemical composition. In particular, elongated secondary phase artefacts were scattered throughout the microstructure (marked with black arrows). The chemical and phase composition of these microstructures will be discussed in the next section.

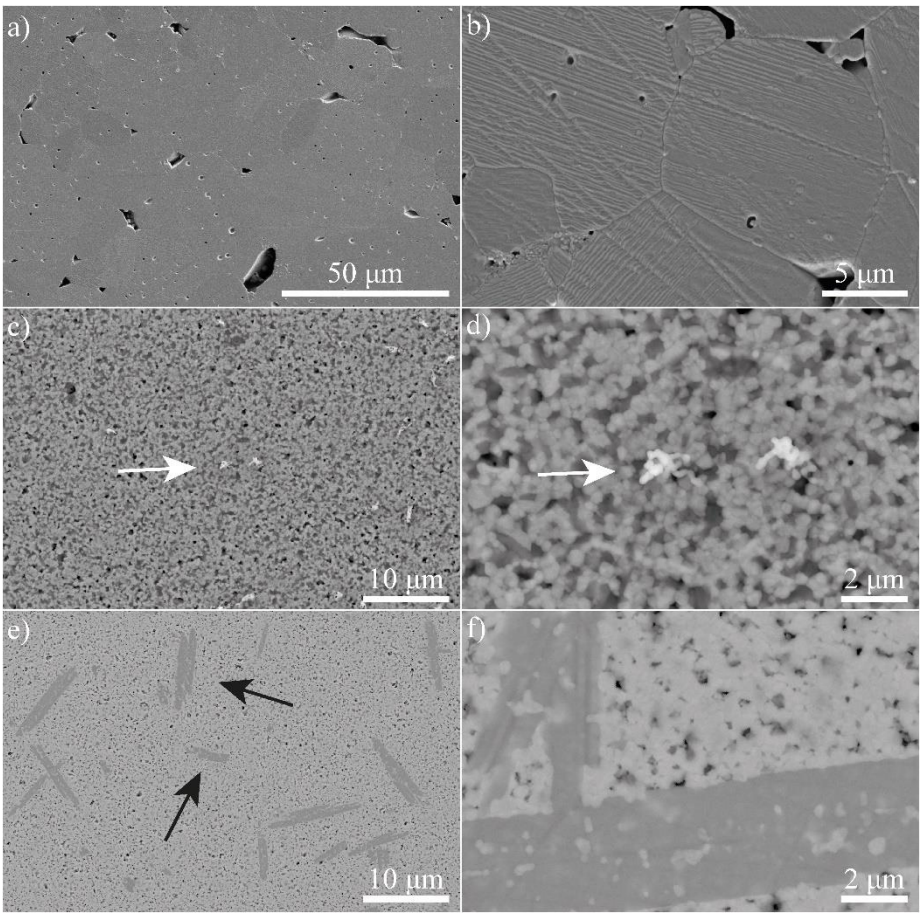

Fig. 19 SEM micrographs (BSE contrast) of a,b) pure $BaTiO_3$, c,d) 10 vol.% Al_2O_3-reinforced $BaTiO_3$ with white arrows indicating the brighter phase, and e,f) 5 vol.% ZrO_2-reinforced $BaTiO_3$ with black arrows indicating the darker phase.

Chemical and phase composition

When dealing with $BaTiO_3$-based particle composites, focus must be placed on the chemical and phase composition, as these significantly impact the ceramic composite's performance in advanced applications. In the case of Al_2O_3 or ZrO_2-reinforced $BaTiO_3$, several reaction products can be expected. Both Al and Zr cations could incorporate into the *B*-site of the $BaTiO_3$ lattice, resulting in the release of the excess TiO_2, which reacts with $BaTiO_3$ to form $Ba_6Ti_{17}O_{40}$ [177,178]. Higher amounts of Al_2O_3 in the system react with $BaTiO_3$, BaO, TiO_2, and $Ba_6Ti_{17}O_{40}$ to form $BaAl_2O_4$ and $Ba_4Ti_{10}Al_2O_{27}$ [177] and even higher amount can lead to formation of $BaTiAl_6O_{12}$ [179]. On the other hand, the addition of ZrO_2 leads to the formation

of $BaZrO_3$ and $Ba(Ti, Zr)O_3$ solid solution [178]. The presence of these reaction products was investigated by EDX and XRD analyses.

EDX mapping of Al in 10 vol.% Al_2O_3-reinforced $BaTiO_3$ (see **Fig. 20**) shows that Al was generally more abundant in locations that appear darker in the BSE contrast. These spots might be attributed to the $Ba_6Ti_{17}O_{40}$, $BaAl_2O_4$, and $Ba_4Ti_{10}Al_2O_{27}$ phases [177].

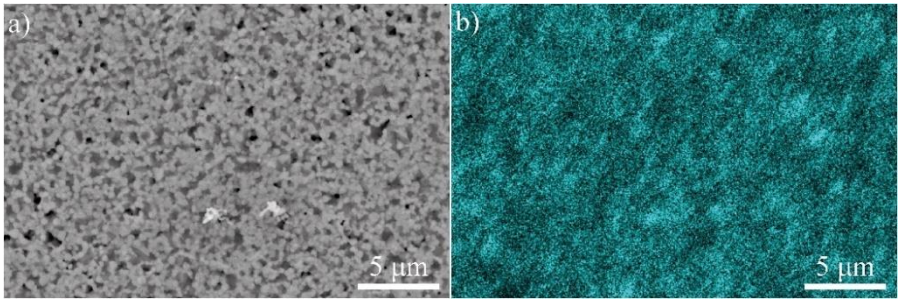

Fig. 20 SEM micrograph (a) with EDX maps showing the distribution of Al (b) in the microstructure of 10 vol.% of Al_2O_3-reinforced $BaTiO_3$.

EDX mapping of Zr (**Fig. 21**b) and Ti (**Fig. 21**c) in 5 vol.% ZrO_2-reinforced $BaTiO_3$ shows that the secondary darker phase contained higher concentrations of Zr and Ti. However, the dispersion of Zr was not restricted to this phase. Previous data reported by Lu et al. [178] and Armstrong et al. [180] on $BaTiO_3$ + ZrO_2 sintering experiments with several orders of magnitude longer dwell times have shown that Zr was thoroughly dispersed in the $BaTiO_3$ matrix, which resulted in reduced tetragonality of $BaTiO_3$. The present work aimed to preserve the tetragonal $BaTiO_3$ for its piezoelectric performance by employing rapid sintering cycles with shorter dwell times, which would hinder the diffusion of added cations. The phase composition analysis will be discussed in the next section.

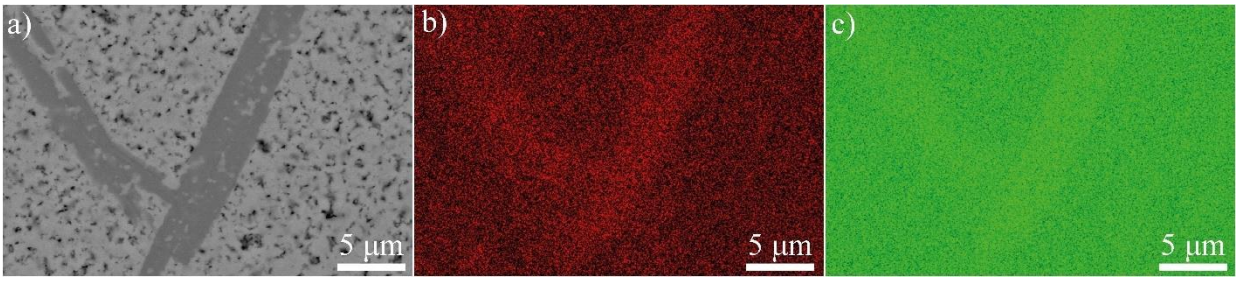

Fig. 21 SEM micrograph (a) with EDX maps showing the distribution of Zr (b), and Ti (c) in the microstructure of 5 vol.% of ZrO_2-reinforced $BaTiO_3$.

The influence of the added phases and the extent of the reaction on the phase composition of the particle composites was analysed by XRD. **Fig. 22**a-c shows the diffraction patterns of Al_2O_3-reinforced $BaTiO_3$. Minority phase peaks between 28 and 34° 2θ have been attributed to $BaAl_2O_4$ (#ICSD 021080) and $Ba_4Ti_{10}Al_2O_{27}$ (#ICSD 087085) [177] (see **Fig. 22**b). Note that residual $Ba_6Ti_{17}O_{40}$ may still be present in the samples [177], but its diffraction pattern overlaps with that of $Ba_4Ti_{10}Al_2O_{27}$. A detailed view of the split (002) and (200) peaks around 45° 2θ, characteristic for tetragonal $BaTiO_3$, in **Fig. 22**c shows that the peak splitting decreased slightly but was still preserved with increasing Al_2O_3 content. This information is important for the viability of the prepared composites as piezoceramics. The tetragonality of $BaTiO_3$, expressed in terms of the *c/a* ratio of the lattice parameters, decreased from 1.0103 ($BaTiO_3$) to 1.0060 (10 vol.% Al_2O_3), which is in agreement with the literature [52] and Raman spectroscopy results (not shown here).

Diffractograms of ZrO_2-reinforced $BaTiO_3$ are shown in **Fig. 22**d. A detailed view at 26–36° 2θ region (**Fig. 22**e) confirms the presence of the reaction product Ba_2ZrO_4 (#ICSD 039707) or $BaZrO_3$ [178] and ZrO_2 (#ICSD 068589, at the highest concentration of reinforcing phase). The Ba_2ZrO_4/$BaZrO_3$ phases should be related to the presence of the Ti-rich phase $Ba_6Ti_{17}O_{40}$ [178], which was not detected by XRD due to the detection limit of the technique. The most notable change in the diffractograms was the gradual splitting of the (101) $BaTiO_3$ peak into two, with a distinct cubic barium titanate (#ICSD 028853) peak at lower angle. It has been reported that the cubic phase content increases with the addition of ZrO_2 [178]. This was investigated by looking at the 44–46° 2θ region (**Fig. 22**f) where the original tetragonal $BaTiO_3$, with distinctly split (002) and (200) peaks, was gradually replaced by a mixture of more $BaTiO_3$ structural phases. Even with 3 vol.% ZrO_2 added, the amount of tetragonal $BaTiO_3$ was significantly reduced and the majority was orthorhombic phase. The tetragonal phase disappeared completely at higher ZrO_2 concentrations, and the samples consisted mainly of orthorhombic and cubic $BaTiO_3$ accompanied by the minority phases mentioned above. The expected presence of Ba(Ti, Zr)O_3 solid solution [178] in the microstructure cannot be conclusively demonstrated by XRD due to the similarity of the diffraction patterns with $BaTiO_3$. However, changes in the 44–46° 2θ region suggest its existence, as it tends to occupy cubic, orthorhombic, and even rhombohedral symmetry at room temperature, depending on the amount of Zr in the lattice [181]. The $BaZrO_3$ diffraction pattern is similar to cubic $BaTiO_3$, making refinement challenging. The peaks in the 44–46° 2θ region shifted to lower angles after adding ZrO_2, as previously reported [173]. This was caused by the accommodation of larger Zr^{4+} (0.720 Å) ions in Ti^{4+} (0.605 Å) sites [182] in the TiO_6 octahedra [183].

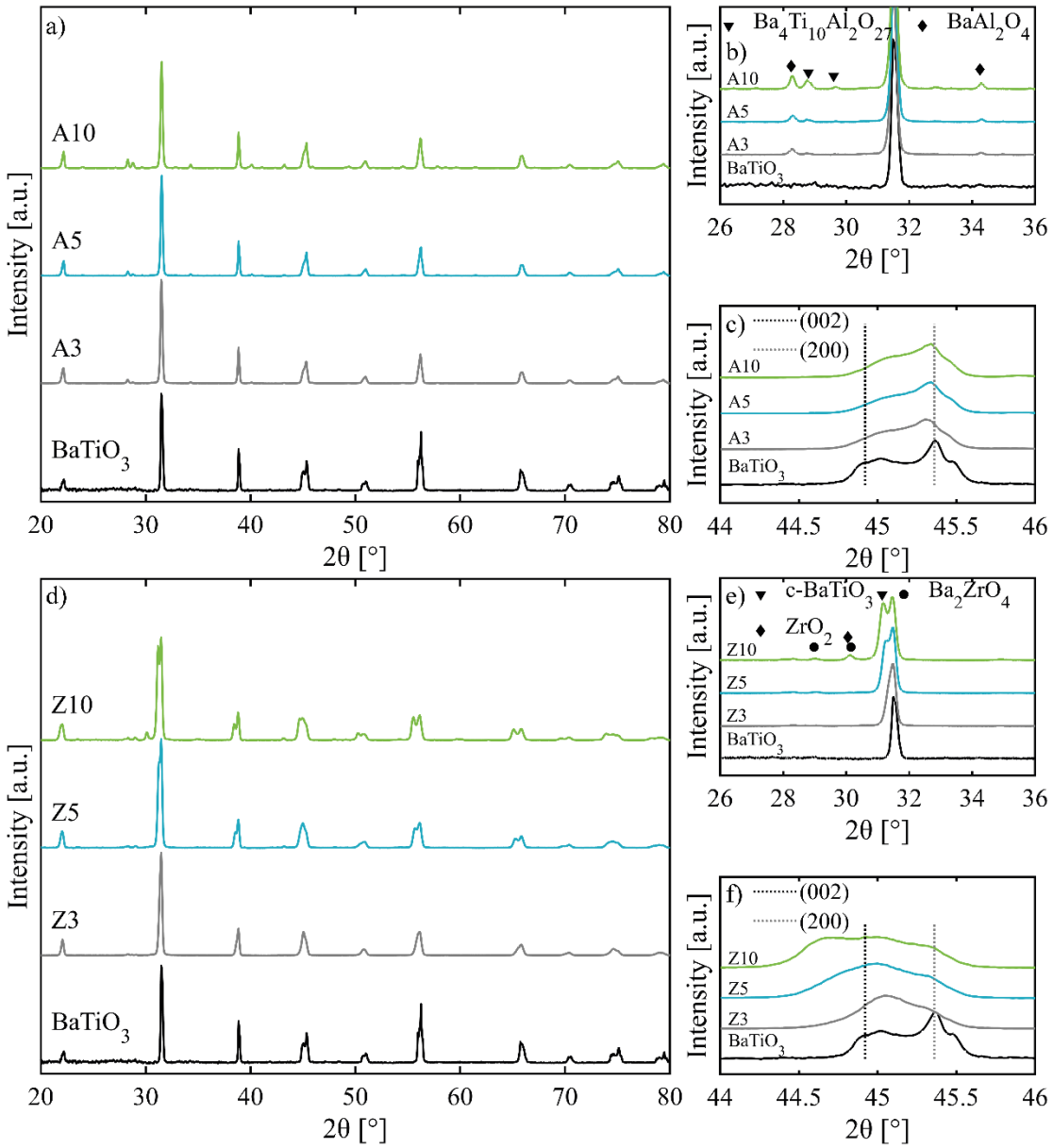

Fig. 22 XRD patterns of $BaTiO_3$ ceramics reinforced with a-c) Al_2O_3 and d-f) ZrO_2.

Relative density

In addition to evaluating the microstructure and phase composition, densification also plays a key role in the mechanical and electrical performance of prepared ceramic composites. The relative densities (calculated by the mixing rule) of $BaTiO_3$-based particle composites after sintering by RPLS at 1250 °C are shown in **Fig. 23**. The exact theoretical density depends on the phase composition of the composite,

but the relatively small amount of detected secondary phases (discussed above) could not dramatically affect the theoretical density of the composites, and the calculated values can be considered realistic. Pure $BaTiO_3$ reached 96% of TD, as discussed in more detail in sub-chapter 5.3. Al_2O_3-reinforced barium titanate exhibited a minor increase to 97% of TD (3 vol.%), followed by a decrease below 95% of TD (10 vol.%). A similar trend was reported in the literature [52,58]. On the other hand, ZrO_2 in the microstructure inhibited the sintering, and the density dropped to 76% of TD (10 vol.%). It is evident that a rapid sintering cycle chosen to eliminate chemical reactions in the composite was insufficient to densify the ZrO_2-reinforced barium titanate. Therefore, ZrO_2-reinforced $BaTiO_3$ samples were excluded from further piezoelectric and fracture toughness analyses due to their low density, inappropriate phase composition, and inhomogeneous microstructure.

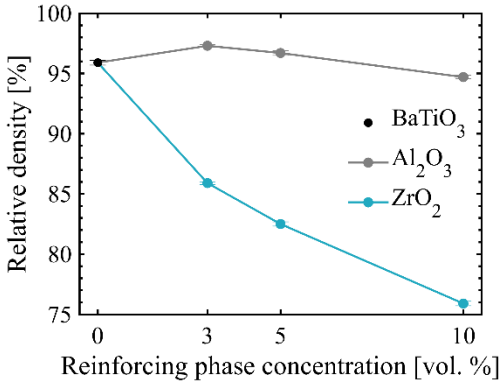

Fig. 23 Relative density of $BaTiO_3$-based sintered ceramics reinforced with Al_2O_3 or ZrO_2.

Piezoelectric properties

The piezoelectric coefficient d_{33} of the prepared Al_2O_3-reinforced composites was measured to establish the role of phase composition and microstructure on the piezoelectric performance. **Fig. 24** shows that the $BaTiO_3$ standard had d_{33} = 180 pC/N. This value is usual for coarse-grained $BaTiO_3$ [184], but the highest reported values for $BaTiO_3$ are in the range of 250–519 pC/N [39,184–187] if the optimal grain size ~1 μm is reached [39,184,187]. The present $BaTiO_3$ had the MGS ~25 μm (sub-chapter 5.3). The composites with added Al_2O_3 experienced a significant decrease to values below 10 pC/N in the sample with the highest concentration. This may be explained by the stoichiometric imbalance in $BaTiO_3$, which reduces tetragonality and negatively affects electric properties [56].

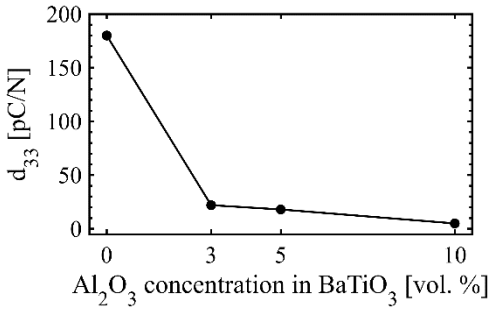

Fig. 24 Piezoelectric coefficient d_{33} of Al_2O_3-reinforced $BaTiO_3$ sintered composites.

Mechanical properties

The main focus of the sub-chapter lies in improving the mechanical properties of $BaTiO_3$ by adding tougher ceramics. Reinforcing phases should provide toughness benefits through various toughening mechanisms [188]; however, the SEM micrograph of the indentation crack propagating through the microstructure of the 5 vol.% Al_2O_3-reinforced $BaTiO_3$ (see **Fig. 25**) showed no evidence of toughening when interacting with the secondary phase particle (darker colour). Crack deflection, bridging, or branching toughening mechanisms [188] were not observed. To quantify the influence of the secondary phase on the fracture resistance of the material, the fracture toughness of the prepared Al_2O_3-reinforced composites was measured.

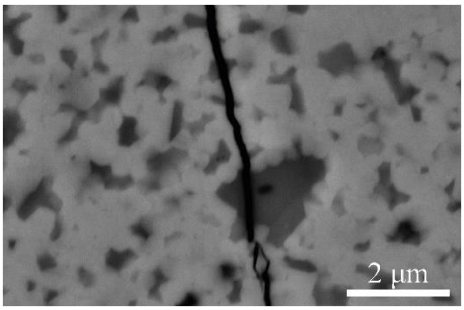

Fig. 25 Propagating crack through the 5 vol.% Al_2O_3-reinforced $BaTiO_3$.

Table 7 shows the fracture toughness of $BaTiO_3$ with added Al_2O_3, including both standards ($BaTiO_3$ and Al_2O_3). Previous reports on fracture toughness of the $BaTiO_3$ resulted in K_{IC} around 1 MPa·m$^{1/2}$ [189,190]. The current fracture toughness of the pure $BaTiO_3$ sample was 0.83 ± 0.04 MPa·m$^{1/2}$, slightly lower, probably due to the coarse microstructure. The addition of Al_2O_3 into $BaTiO_3$ matrix led to lower

fracture toughness associated with the presence of secondary phases. The alumina standard reached ~3.3 MPa·m$^{1/2}$, which is a typical value [191].

Table 7 Fracture toughness of $BaTiO_3$-based sintered ceramics reinforced with Al_2O_3.

Sample	K_{IC} [MPa·m$^{1/2}$]
$BaTiO_3$	0.83 ± 0.04
3 vol.% Al_2O_3	0.65 ± 0.06
5 vol.% Al_2O_3	0.70 ± 0.06
10 vol.% Al_2O_3	0.63 ± 0.09
Al_2O_3	3.33 ± 0.18

Conclusions of the sub-chapter

This sub-chapter has focused on optimising the sintering and phase composition of $BaTiO_3$-based particle composites. Heat treatment by RPLS was used to inhibit the system's reactivity by high heating rate and short dwell time. However, even under these conditions, secondary phases appeared, and no residual alumina was detected in the case of Al_2O_3-reinforced samples. On the other hand, the presence of zirconia strongly inhibited the densification of the samples. As a result, piezoelectric performance and fracture toughness were reduced. Reaction products clearly play an important role, and their proper characterisation could provide essential information. The following sub-chapter will focus on one of the previously uncharacterised reaction products of barium titanate and alumina: $BaTiAl_6O_{12}$.

5.5 Barium titanate and alumina reaction product: $BaTiAl_6O_{12}$

The reaction products in the $BaTiO_3/Al_2O_3$ particle composite profoundly influence the system's properties and performance, as discussed in the previous sub-chapter. Accurate characterisation of these new phases is essential for material design and optimisation of processing steps. The spinel phase $BaAl_2O_4$, often mentioned in the last sub-chapter, has already been described in detail [192–194]. Another important reaction product in composites with a higher content of alumina, $BaTiAl_6O_{12}$ [12,51,54,59], still lacks fundamental characterisation. Therefore, this sub-chapter explores the properties of $BaTiAl_6O_{12}$, prepared by a solid-state reaction. The phase transformation process was monitored by high-temperature dilatometry and evaluated by XRD. The fundamental microstructural, mechanical, and electrical properties of sintered monophasic $BaTiAl_6O_{12}$ were discussed.

Dilatometry and phase evolution

Dry pressed green bodies consisting of a planetary ball-milled 3:1 molar ratio of Al_2O_3:$BaTiO_3$ (66.4:33.6 vol.%) were sintered in a high-temperature dilatometer up to 1450 °C to investigate the solid-state reaction. The shrinkage (black) and shrinkage rate (first derivative, grey) curves show two significant events related to the phase composition change during sintering (see **Fig. 26**). The first event (cyan underpainting) occurred between 1139–1184 °C, followed by the second event (green underpainting) between 1278–1351 °C. To understand the evolution of the phase composition, the complementary XRD analyses of samples sintered at different temperatures (green body, 1250, and 1450 °C) were conducted.

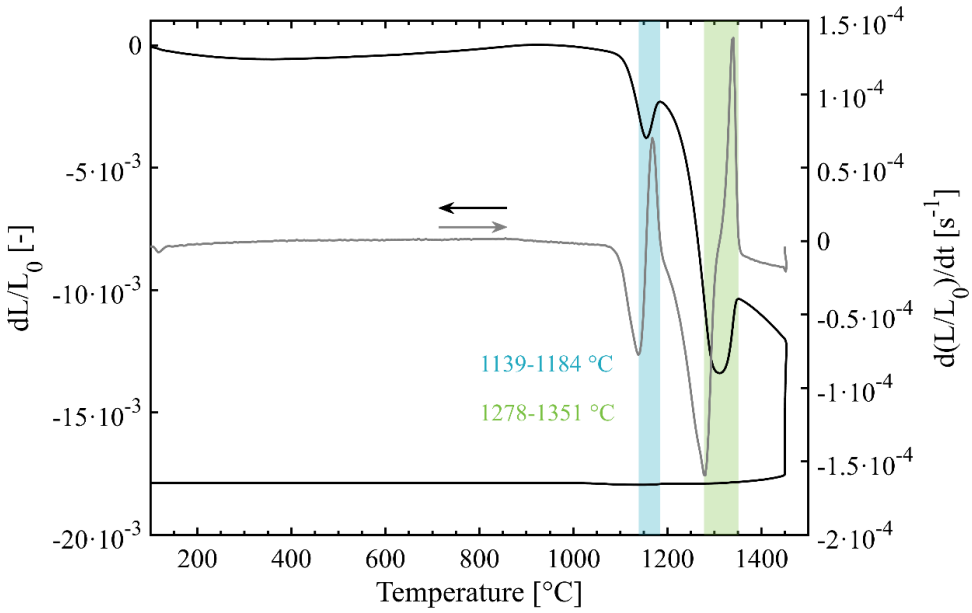

Fig. 26 Dilatometric data from sintering a 3:1 molar ratio of Al_2O_3:$BaTiO_3$ green body.

The XRD patterns describing the stages of the solid-state reaction are shown in **Fig. 27**. The green body diffractogram confirms the presence of Al_2O_3 (#ICSD 031545) and $BaTiO_3$ (#ICSD 067520) in the appropriate proportions. The pattern obtained from the sample sintered at 1250 °C (after the first phase transformation, see **Fig. 26**) shows many coexisting phases. Preserved Al_2O_3 and $BaAl_2O_4$ (#ICSD 021080) formed the majority of the sample, and the minor phases included $BaTiAl_6O_{12}$ (#ICSD 062213), $Ba_4Ti_{10}Al_2O_{27}$ (#ICSD 087085), and $Ba_3TiAl_{10}O_{20}$ (#ICSD 062214). The XRD pattern of the sample after the second phase transformation event (**Fig. 26**) shows only peaks belonging to orthorhombic $BaTiAl_6O_{12}$.

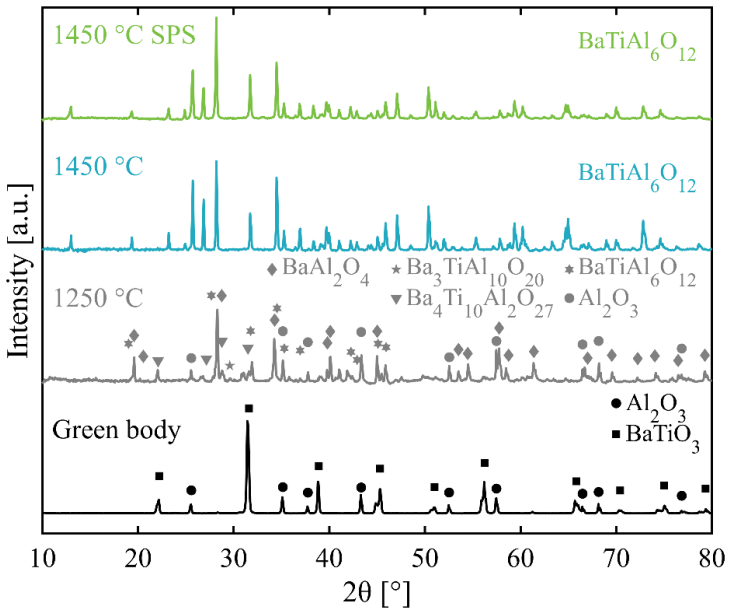

Fig. 27 XRD patterns of 3:1 molar ratio of Al_2O_3:$BaTiO_3$ green body, samples conventionally sintered at 1250 °C and 1450 °C, and sample sintered by SPS at 1450 °C.

Going back to **Fig. 26**, only a small shrinkage of 1.8% was recorded during sintering and the green body was densified from 59.6% of TD only to 77.2% of TD. Therefore, the pressure-assisted sintering method SPS was used to prepare fully dense $BaTiAl_6O_{12}$ (> 99.0% of TD), which is more convenient for further analyses. The XRD pattern of the SPS sample in **Fig. 27** confirms $BaTiAl_6O_{12}$ in the microstructure, indicating that both phase transformation events occurred.

One of the main causes of cracking in ceramic composites combining Al_2O_3 and $BaTiO_3$ is the CTE mismatch. To better understand this phenomenon, the CTE of the reaction product $BaTiAl_6O_{12}$ was investigated. The CTE of the SPS sintered sample was measured and calculated according to Equation 1 along the *x, y*-axis (perpendicular to the applied pressure) and *z*-axis (parallel to the applied pressure). The CTE in *x, y* direction was $8.35 \cdot 10^{-6}$ K^{-1} and in *z* direction was $7.20 \cdot 10^{-6}$ K^{-1}. The slight difference may indicate CTE anisotropy and potentially grain crystallographic anisotropy, which will be further discussed. The measured values are more similar to the CTE of alumina ($8 \cdot 10^{-6}$ K^{-1} [195]) than to $BaTiO_3$ ($11 \cdot 10^{-6}$ K^{-1} [12,196]).

Microstructure

EBSD analysis revealed the presence of elongated grains with varying crystallographic orientations (see **Fig. 28**a). The pressure applied during SPS could cause grain elongation, similar to $Al_2W_3O_{12}$ discussed in sub-chapter 5.2. The grain size distribution in **Fig. 28**b confirms a normal distribution with d_{50} = 20.2 µm. Detailed EBSD and SEM analyses (**Fig. 28**c,d) of a triple-junction point revealed the presence of the remaining secondary phase (white arrow). This observation contradicted the XRD analysis, where no secondary phase was detected. Therefore, an image analysis was performed to calculate its relative representation in the microstructure. The calculated amount of 2.5% was below the resolution limit of the XRD analysis. Based on the EBSD data, the secondary phase was estimated as monoclinic $Ba_3TiAl_{10}O_{20}$.

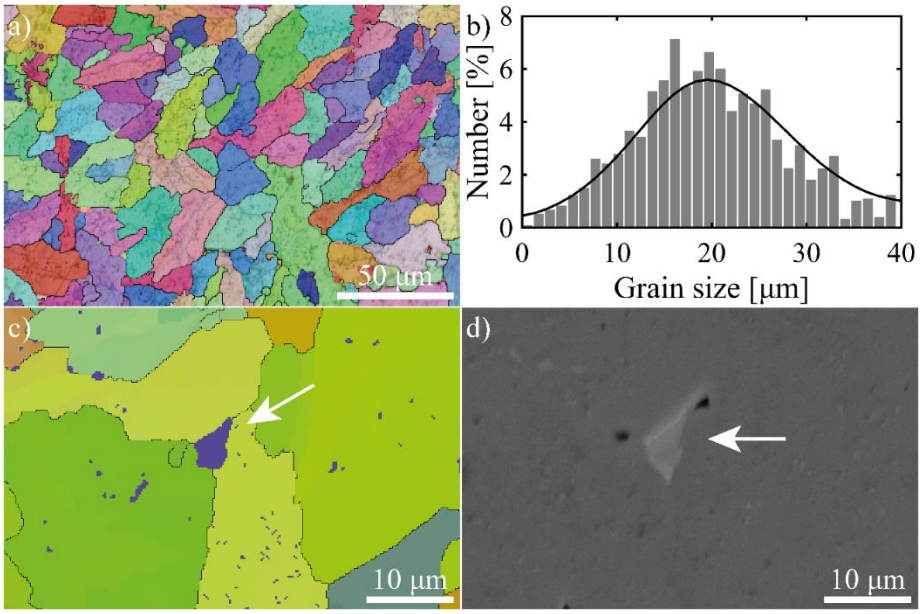

Fig. 28 Microstructure of sintered $BaTiAl_6O_{12}$ shown in a) EBSD map with marked grains, b) grain size distribution, c) detailed EBSD map and d) SEM image showing the secondary phase (marked with white arrow) at the triple-point.

Mechanical properties

The indentation size effect of the $BaTiAl_6O_{12}$ was studied by various loads (0.98 – 49.03 N) using the Vickers indentor. The dependence of indentation hardness (calculated from the indentation depth) and indentation elastic modulus are shown in **Fig. 29**. Typical curve shapes were recorded [197] with plateau appearing at loads above 10 N. Indentation hardness stabilised above 10 GPa and elastic modulus above 130 GPa. The impulse excitation method showed Young's modulus value of 179.00 ± 0.08 GPa, corresponding to the values obtained by low indentation load. The impulse excitation generally provides higher values than mechanical deformation methods and is more comparable to nanoindentation [198]. The calculated shear modulus was 69.50 ± 0.05 GPa and Poisson's ratio was 0.290 ± 0.001. Elastic properties of $BaTiAl_60_{12}$ are higher than the $BaTiO_3$ but are well below the typical values for Al_2O_3 [199,200]. Similarly, the three-point bending test flexural strength was 129.90 ± 4.57 MPa, which is above the value around 100 MPa reported for $BaTiO_3$ [199] but significantly lower compared to 480 MPa of Al_2O_3 [201].

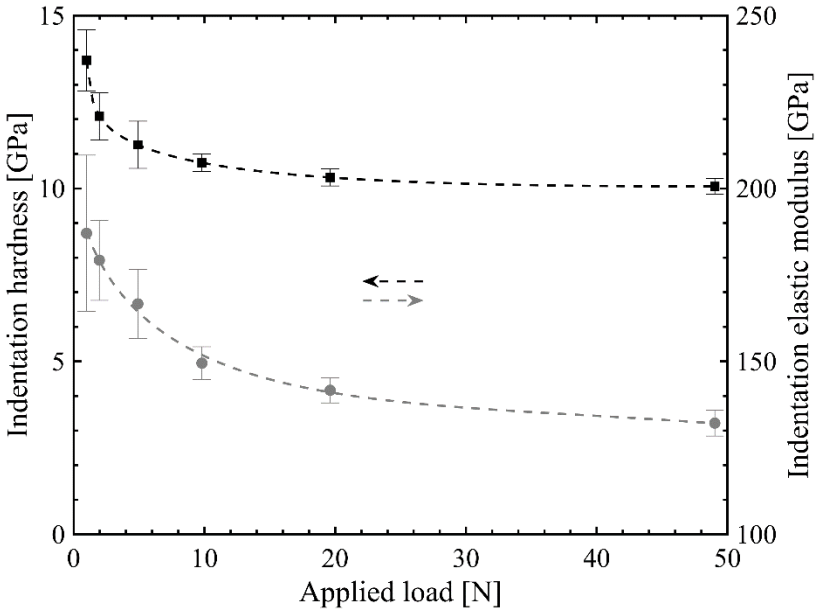

Fig. 29 Indentation hardness and Indentation elastic modulus of $BaTiAl_6O_{12}$ ceramics as a function of applied load.

The toughness of Al_2O_3-reinforced $BaTiO_3$ ceramic composites depends not only on the toughness of the starting phases but also on their reaction products. For this reason, the fracture toughness of $BaTiAl_6O_{12}$ was measured and reached the value of 1.80 ± 0.15 MPa·m$^{1/2}$. Compared with the fracture toughness of $BaTiO_3$ reinforced with various amounts of finely dispersed Al_2O_3 (sub-chapter 5.4), it is apparent that the $BaTiAl_6O_{12}$ (66 vol.% of Al_2O_3) dramatically increased the K_{IC} from below 1 MPa·m$^{1/2}$ and fits reasonably well to the second order polynomial fit (see **Fig. 30**). The overall better mechanical properties of $BaTiAl_6O_{12}$ than $BaTiO_3$ could be advantageous, when formed on $BaTiO_3$/Al_2O_3 interfaces.

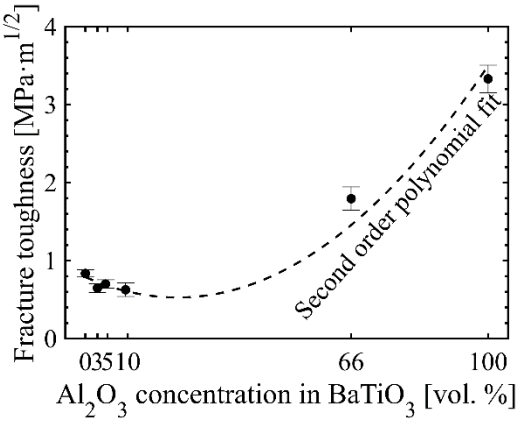

Fig. 30 Fracture toughness of Al_2O_3-reinforced $BaTiO_3$ ceramics.

Electrical properties

Similar to the mechanical and thermal expansion properties of $BaTiAl_6O_{12}$, its electrical properties also play an important role in the final performance of the ceramic composite. **Fig. 31** shows the ε_r and *tan* δ as a function of frequency. $BaTiAl_6O_{12}$ exhibited a low ε_r = 16.0 at a frequency of 1 kHz. By lowering the frequency to 10 mHz, ε_r increased slightly to 16.5. The *tan* δ showed similar behaviour. At the lowest frequency of 10 mHz, the loss was 0.0350 and with increasing frequency, it gradually decreased to a minimum value ~0.0001. The measured ε_r was slightly higher than 10 for alumina [202] but significantly lower than the maximum values reported for $BaTiO_3$ in the range of 5000–10000 [40,185,203,204].

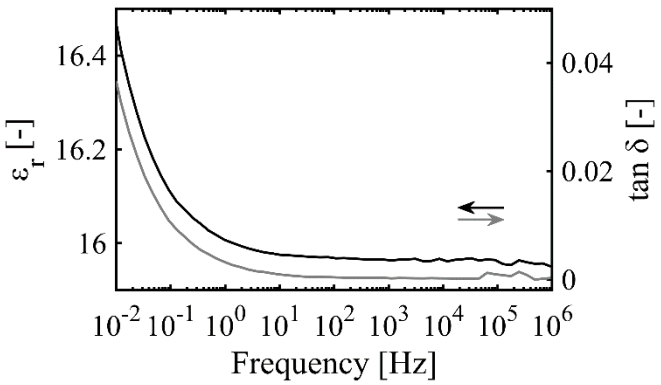

Fig. 31 The frequency dependence of ε_r and *tan* δ.

Conclusions of the sub-chapter

This sub-chapter has aimed to describe the fundamental material properties of the $BaTiAl_6O_{12}$ phase, a reaction product in $BaTiO_3/Al_2O_3$ composites. It has been shown that under conventional sintering conditions, the $BaTiO_3/Al_2O_3$ powder mixture undergoes two notable phase transformations with pure $BaTiAl_6O_{12}$ present at 1450 °C. SPS was used to achieve a fully dense ceramic body. The grains were distorted due to the applied pressure. Mechanical properties were improved compared to pure $BaTiO_3$ or $BaTiO_3$-based composites with lower concentrations of Al_2O_3, as discussed in sub-chapter 5.4. Electrical properties showed that $BaTiAl_6O_{12}$ is a relatively poor dielectric with low relative permittivity. Al_2O_3 is not the only oxide ceramic that reacts with barium titanate in ceramic composites. As was mentioned in the sub-chapter 5.4, ZrO_2, frequently used structural ceramics, can strongly react with $BaTiO_3$. The following sub-chapter focuses on piezoelectric/dielectric laminated composites prepared by EPD and introduces BCZT to eliminate chemical reactions with reinforcing ZrO_2 layers.

5.6 Barium titanate and barium calcium zirconate titanate-based laminated composites

This sub-chapter builds on previously acquired knowledge about $BaTiO_3$-based composites and focuses on the fabrication and characterisation of laminated composites combining $BaTiO_3$ or BCZT with ZrO_2 layers. The EPD was used to control the layer thickness precisely. The deposits were sintered conventionally and by SPS. The microstructure, chemical composition, phase composition, and mechanical properties of laminated composites were characterised.

Electrophoretic deposition

The deposition process of each ceramic material was optimised based on previous reports [13,44,115] to obtain similar green densities: 44.7 ± 0.1% of TD ($BaTiO_3$), 46.7 ± 0.1% of TD (BCZT), and 47.4 ± 0.1% of TD (ZrO_2). It is one of the principal conditions used to avoid delamination in a multi-layered ceramic composite, which would reduce its mechanical and electrical performance. Another important factor affecting the laminate coherence is the CTE mismatch between the materials. $BaTiO_3$ and BCZT have CTE $11.0 \cdot 10^{-6}$ K^{-1} [12,196] whilst ZrO_2 has $10.3 \cdot 10^{-6}$ K^{-1} [13], which is reasonably similar. Moreover, kinetic data acquired during such depositions enabled the calculation of precise deposition times to control the thickness of the individual layers [115].

Microstructure

SEM images of the microstructure of conventionally sintered laminates in **Fig. 32**a and **Fig. 32**c show $BaTiO_3/ZrO_2$ (1300 °C) and BCZT/ZrO_2 (1500 °C) composites, respectively. **Fig. 32**a shows that even the small CTE mismatch between well-defined 60 µm thick layers was too high, and $BaTiO_3$ (brighter layers) developed cracks perpendicular to the interface. In addition, the sintering temperature of 1300 °C was chosen for the densification of ZrO_2 but is rather high for $BaTiO_3$, as discussed in sub-chapter 5.3 and the literature [172]. The microstructure was coarsened, and the strong reaction between the materials (discussed below) adversely affected the $BaTiO_3$ layers. Similarly, **Fig. 32**c shows that the optimal sintering temperature of 1500 °C for BCZT [46] was too high, the microstructure coarsened, the materials reacted, porosity and cracks appeared, and it was difficult to distinguish the individual layers.

Sintering the same laminates by SPS at lower temperatures (1250 °C for $BaTiO_3/ZrO_2$ and 1350 °C for BCZT/ZrO_2 laminates) eliminated most problems and produced well-defined ~25 µm thick layers. The $BaTiO_3/ZrO_2$ laminate still contained some reaction zones (see **Fig. 32**b), whilst BCZT/ZrO_2 laminate

showed no reaction during sintering (see **Fig. 32**d). However, slight interlayer contamination was present in both composites, probably due to the EPD process.

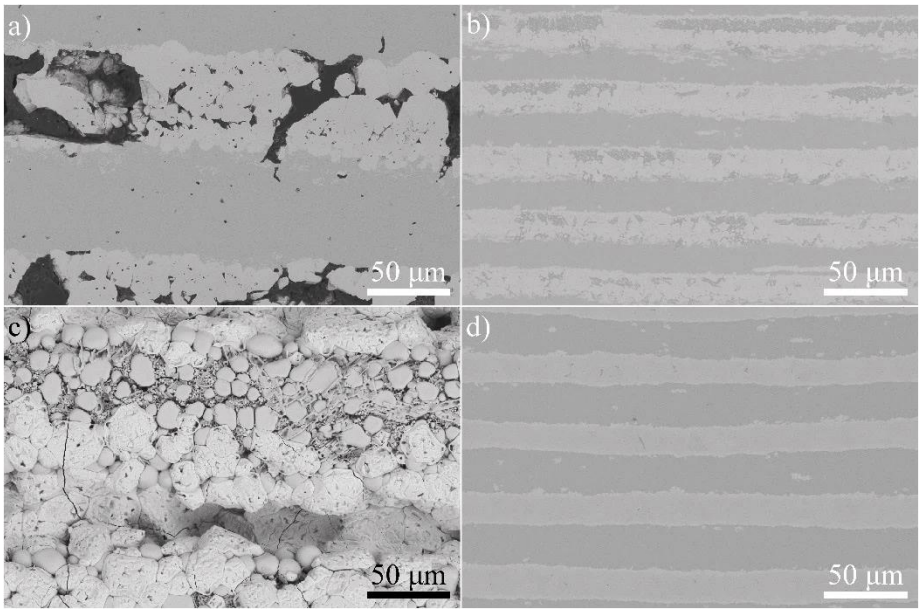

Fig. 32 SEM micrographs of a,b) $BaTiO_3/ZrO_2$ and c,d) $BCZT/ZrO_2$ laminates after sintering conventionally and using SPS [205].

Chemical and phase composition

The chemical composition was analysed across the layer boundaries by EDX (see **Fig. 33**), except for the conventionally sintered $BCZT/ZrO_2$ laminate, which was excluded from further analyses due to its microstructure (see **Fig. 32**c). The EDX line scan of the conventionally sintered $BaTiO_3/ZrO_2$ laminate in **Fig. 33**a confirms a strong chemical reaction at the interface. Zr^{4+} cations have substituted Ti^{4+} at *B*-sites in the perovskite structure of $BaTiO_3$ [178] to form Ba-rich $BaZrO_3$. Exsolved TiO_2 could then react with $BaTiO_3$ and $BaZrO_3$ to form Ti-rich $Ba_6Ti_{17}O_{40}$ and solid solution Ba(Ti, Zr)O_3 [178]. Note that some Ba and Ti atoms were detected even deeper in the ZrO_2 layer. A comparable situation, but to a lesser extent, was observed in the $BaTiO_3/ZrO_2$ laminate sintered by SPS. The EDX line scan through the entire original $BaTiO_3$ layer in **Fig. 33**b shows that Ba-rich (brighter) and Ti-rich (darker) areas were present, and ~5 at.% of Zr is detected throughout the layer. On the other hand, the $BCZT/ZrO_2$ laminate sintered by SPS showed no detectable reaction (see **Fig. 33**c). This is probably due to the combination of relatively low sintering temperature for BCZT and the fact that BCZT is already partially saturated with Zr^{4+} cations.

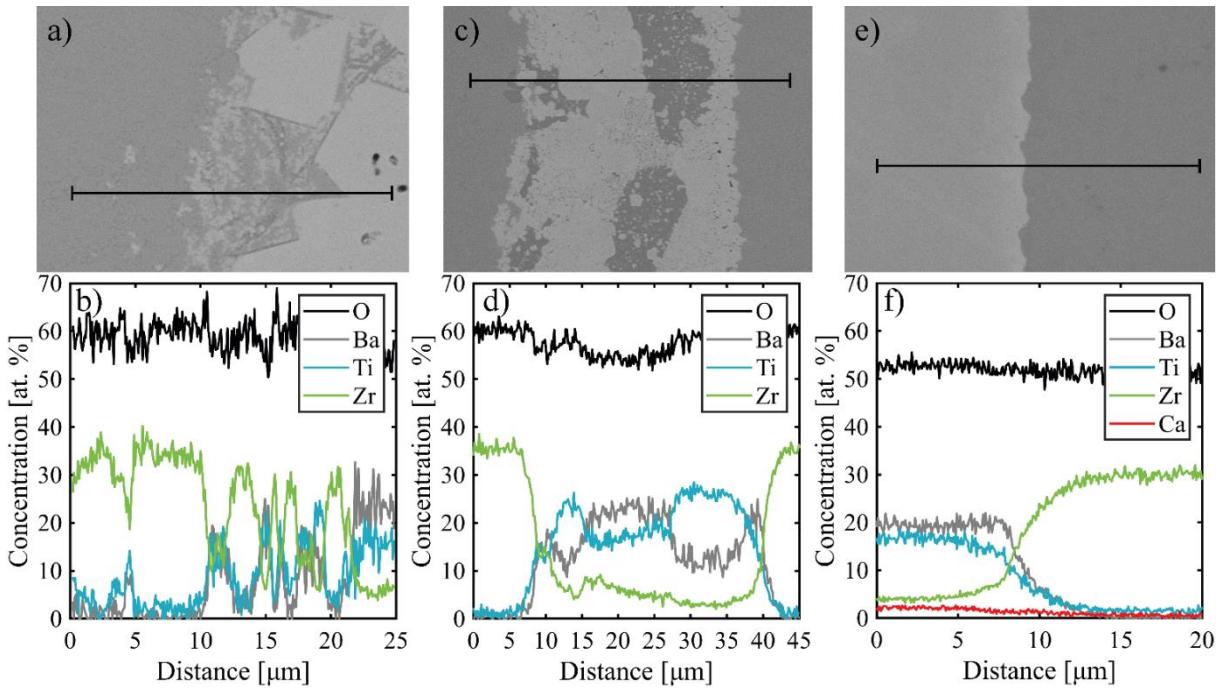

Fig. 33 EDX line scans of a,b) conventionally sintered $BaTiO_3/ZrO_2$ laminate; c,d) $BaTiO_3/ZrO_2$ and e,f) $BCZT/ZrO_2$ laminates sintered using SPS [205].

Phase composition

The local phase composition was analysed using Raman spectroscopy. Superimposed intensity maps with corresponding spectra are shown in **Fig. 34**. The intensity of the maps was based on the peak intensity at ~510 cm^{-1} belonging to the A_1(TO) vibrational mode of $BaTiO_3$. **Fig. 34**a,b shows the Raman mapping of conventionally sintered $BaTiO_3/ZrO_2$. The spectrum measured at the ZrO_2 layer (spot 1) contained 6 active modes at 152, 265, 321, 468, 610, and 646 cm^{-1} of tetragonal ZrO_2 [206]. Other selected regions of interest from the $BaTiO_3$ layer had spectra typical for ferroelectric $BaTiO_3$ with varying degrees of intensity of peak around 307 cm^{-1} of the B_1+E(LO+TO) vibrational mode, which is typical for tetragonal, orthorhombic, and rhombohedral $BaTiO_3$ [207], and the negative peak at 180 cm^{-1}, which is related to tetragonal $BaTiO_3$ [208,209] (both indicated by black arrows). The $BaTiO_3$ layer reacted with the surrounding ZrO_2, as evidenced by SEM and EDX. However, cubic $BaTiO_3$ was insignificant in the microstructure, based on Raman spectra.

Fig. 34c,d shows the Raman mapping and spectra of the $BaTiO_3/ZrO_2$ laminate sintered using SPS. The ZrO_2 layer measured at spot 1 showed a typical spectrum for tetragonal ZrO_2 [206]. The situation in the $BaTiO_3$ layer was more complicated, and spectra from spots 2–4 differed. Spot 2 exhibited a typical spectrum of cubic $BaTiO_3$ with two low-intensity broad bands centred around 260 and 530 cm^{-1}, and completely lacked the characteristic sharp peak around 307 cm^{-1} of the B_1+E(LO+TO) vibrational mode [207]. Spot 3 exhibited higher intensity spectrum typical for tetragonal $BaTiO_3$ stable at room temperature. However, sharp peak around 307 cm^{-1} was still missing and cubic $BaTiO_3$ was probably still present in the microstructure. Spot 4, located in the darker Ti-rich phase, showed no Raman signal, and contained only noise. This was probably caused by a complicated crystal structure with defects [192].

Fig. 34e,f shows the Raman mapping and spectra of the $BCZT/ZrO_2$ laminate sintered using SPS. In this case, there were only two regions: spot 1 in the ZrO_2 layer and spot 2 in the BCZT layer. The Raman signal in the ZrO_2 layer was again typical for tetragonal ZrO_2 [206]. Raman spectra collected from the BCZT layer exhibited a signal typical for tetragonal BCZT [210] with most prominent modes at 176, 290, 522, and 725 cm^{-1}, marked by grey arrows. Notably, the peak at 490 cm^{-1} attributed to orthorhombic BCZT was missing. The co-existence of tetragonal-orthorhombic BCZT at room temperature has been reported several times [42,47,100] but tetragonal BCZT has also been observed [210,211]. The influence of chemical and phase composition on mechanical properties is discussed in the next paragraph.

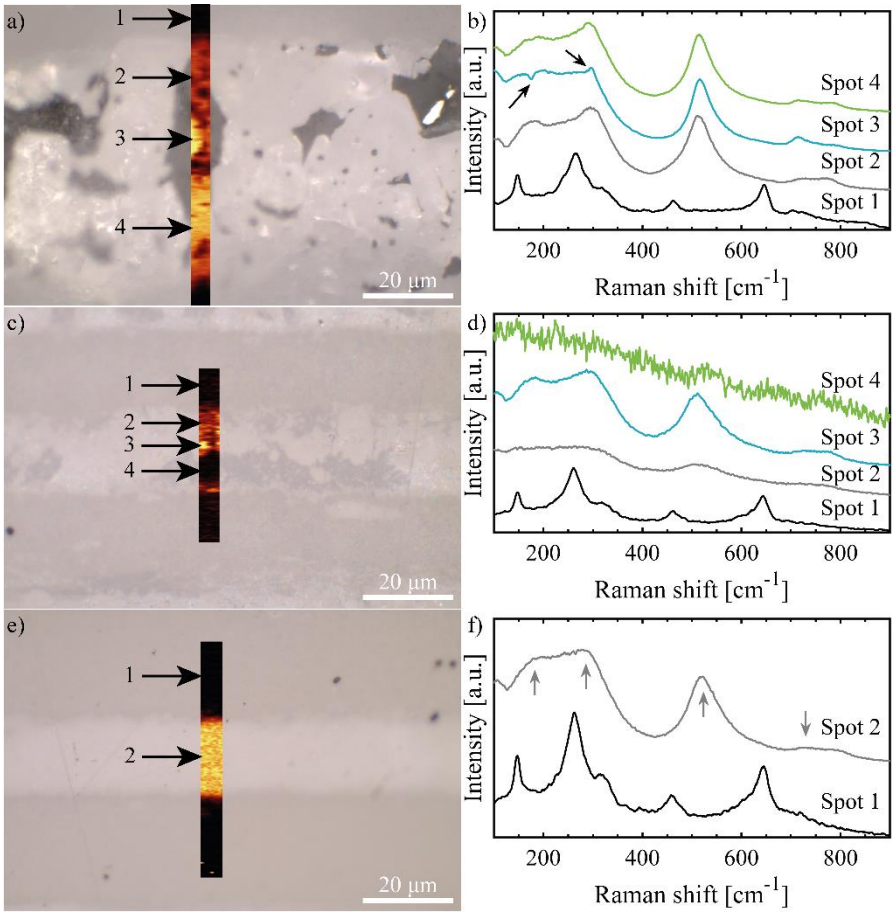

Fig. 34 Raman maps and spectra from the selected spots of a,b) conventionally sintered $BaTiO_3/ZrO_2$ laminate; c,d) $BaTiO_3/ZrO_2$ and e,f) $BCZT/ZrO_2$ laminates sintered using SPS.

Mechanical properties

The indentation hardness and indentation modulus of the sintered laminates are shown in **Fig. 35**. The hardness and modulus of ZrO_2 in the $BaTiO_3/ZrO_2$ laminates sintered in the conventional furnace (black dots) and by SPS (grey dots) were negatively affected by the chemical reactions during the sintering and the change at the interface was not as pronounced as in the $BCZT/ZrO_2$ laminate sintered by SPS (cyan dots). The conventionally sintered laminate achieved lower and more scattered values of hardness and modulus, probably due to the combined effects of coarser microstructure [170], microporosity, and more extensive chemical reactions (note that indents affected by large porosity were excluded). The difference in indentation modulus in the ZrO_2 layer between SPS densified laminates (from ~208 GPa

to ~194GPa) was caused by a 100 °C lower sintering temperature and corresponds to a ~3% increase in porosity according to the Ishai-Cohen model [212].

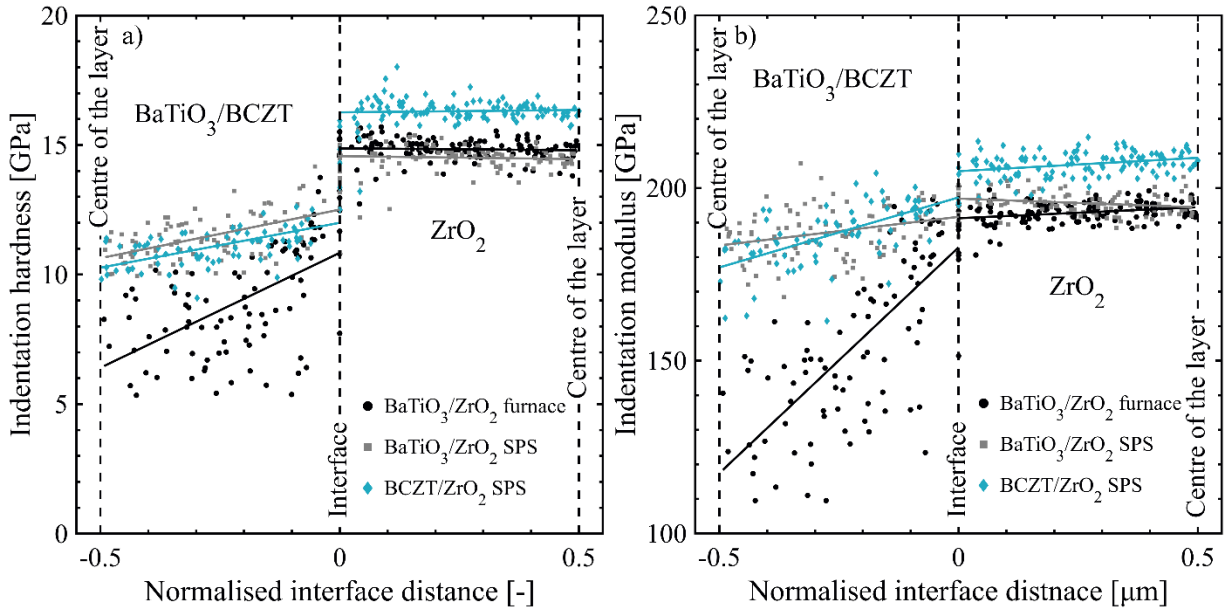

Fig. 35 Indentation a) hardness and b) modulus dependence on normalised distance from the interface of $BaTiO_3/ZrO_2$ laminate sintered conventionally, and $BaTiO_3/ZrO_2$ and $BCZT/ZrO_2$ laminates sintered using SPS [205].

Conclusions of the sub-chapter

This sub-chapter has shown that EPD followed by SPS is a suitable processing strategy for manufacturing laminated composites with $BaTiO_3$ and BCZT layers for potential use in the ceramic multilayer harvesters. Porosity and chemical reactions between highly reactive $BaTiO_3$-based and ZrO_2 ceramics were reduced compared to conventionally sintered laminates. The positive effect on composite's mechanical properties is a crucial benefit for any potential applications. The results summarised in this sub-chapter were already published in Materials Letters (Q2, see ref [205]).

6 Conclusions

In conclusion, this dissertation thesis has provided insights into optimising advanced oxide ceramic materials and composites, focusing on hydroxyapatite, aluminium tungstate, and piezoelectric $BaTiO_3$-based ceramics. Innovative processing techniques have been used to address several key limitations of these materials, including the use of toxic stabilisers, low density, and inferior mechanical and electrical properties.

Hydroxyapatite biocoatings were prepared from plasma treated nanopowder, which allowed a controlled EPD process without toxic stabilisers in the suspensions. This resulted in uniform and homogeneous coatings of high green density. The stand-alone coatings were then sintered by RPLS at 1100–1300 °C with 5–120 min dwell and 5–100 °C/min heating and cooling rates. Rapid heating rates were found to be beneficial in terms of the final density and grain size. To demonstrate practical applicability, the metal orthopaedic screws were coated during EPD by thin, uniform, and crack-free biocoatings from the suspensions containing plasma treated powder.

Aluminium tungstate was synthesised by an optimised co-precipitation method to obtain an amorphous powder with the highest specific surface area and improved sinterability. The powder was calcined at 500–620 °C, and gradual crystallisation and a decreasing concentration of oxygen vacancies were described. The powder calcined at 570 °C was deagglomerated by high-energy ball milling and consolidated by dry-pressing. Dilatometric analysis was used to select sintering temperatures for RPLS and SPS. The best results were obtained by SPS at 850 °C, a significantly lower sintering temperature than previously reported, with the best density to date and improved mechanical properties compared to RPLS samples.

The study of barium titanate-based ceramics covered several topics. Firstly, the microstructural evolution of barium titanate under unconventional RPLS and radiation-assisted sintering techniques was described. Abnormal grain growth occurred in a narrow temperature range around 1230 and 1350 °C for RPLS and radiation-assisted sintering, respectively, indicating differences in energy transfer and temperature measurement reliability of the selected sintering methods. The final density was over 98% in both cases, a higher value than previously reported for conventionally sintered barium titanate.

The knowledge gained was used to sinter up to 10 vol.% of alumina or zirconia-reinforced barium titanate particle composites. Heat treatment was conducted by RPLS at 1250 °C, and the composites were

characterised in terms of microstructure, phase composition, density, fracture toughness, and piezoelectric properties. The high reactivity of the system resulted in the evolution of various secondary phases, causing a decrease in most of the measured properties. In addition, one of the important reaction products of the Al_2O_3 + $BaTiO_3$ system, $BaTiAl_6O_{12}$, was synthesised and thoroughly characterised in terms of microstructural, mechanical, and electrical properties for the first time.

Finally, laminated composites were prepared by combining piezoelectric barium titanate or barium calcium zirconate titanate with zirconia. EPD was used to prepare the precise layer structures, and two different sintering strategies were applied to densify them with suppressed development of reaction zones on the layer boundaries. The conventionally sintered BCZT/ZrO_2 and $BaTiO_3$/ZrO_2 laminates proved to be excessively reactive. The SPS technique significantly reduced reactivity, resulting in more densified samples having better mechanical response.

7 Figure captions

Fig. 1 Cubic and tetragonal $BaTiO_3$ crystal cell with the indicated direction of the intrinsic polarisation P_S [34].
Fig. 2 Schematic setup for a) pressure-assisted sintering and b) radiation-assisted sintering in an SPS machine [98].
Fig. 3 TG/DTG (a) and MS (b) curves of as received and plasma treated HA powders [121].
Fig. 4 Deconvoluted XPS spectra of C 1s and N 1s peaks for as received (a, b) and plasma treated (c, d) HA powders [121].
Fig. 5 Deposition yields (a) and photographs of as received (b) and plasma treated (c) HA coatings [121].
Fig. 6 HA biocoatings on stainless steel orthopaedic screws fabricated by EPD from suspensions containing a) as received powder and b) plasma treated powder [121].
Fig. 7 SEM micrographs of a) amorphous, b) calcined non-milled, and c) calcined milled $Al_2W_3O_{12}$ powders with their particle size distributions (d) [150].
Fig. 8 Simultaneous TG and DSC curves of amorphous $Al_2W_3O_{12}$ powder, with marked water evaporation (cyan underpainting) and crystallisation (green underpainting) events. Note the downward orientation of the exothermic DSC peaks [155].
Fig. 9 XRD patterns of amorphous $Al_2W_3O_{12}$ powder and powders calcined at 500–620 °C [155].
Fig. 10 Raman spectra of amorphous and calcined $Al_2W_3O_{12}$ powders with marked vibrational modes ν_1– ν_4 [155].
Fig. 11 Photographs of amorphous and calcined $Al_2W_3O_{12}$ powders [155].
Fig. 12 EPR signals of amorphous and calcined $Al_2W_3O_{12}$ powder in air between 500 and 620 °C [155].
Fig. 13 Relative shrinkage and shrinkage rate curves with underpainted regions of interest (a) and absolute shrinkage measured during the SPS process (b) of non-milled and milled $Al_2W_3O_{12}$ powders [150].
Fig. 14 XRD patterns of samples sintered by RPLS and SPS [150].
Fig. 15 SEM micrographs of $Al_2W_3O_{12}$ samples from milled powder sintered by a) RPLS with 10 min dwell time, b) SPS at 1000 °C, and c) SPS at 850 °C (note the different scalebar). White arrows indicate microcracks, and black arrows mark preserved clusters of finer grains [150].
Fig. 16 Cumulative grain area distributions of sintered $Al_2W_3O_{12}$ samples [150].
Fig. 17 Relative density as a function of sintering temperature for RPLS and radiation-assisted sintered $BaTiO_3$ samples.
Fig. 18 SEM micrographs of $BaTiO_3$ a) sample sintered by RPLS at 1220 °C with white arrows indicating abnormal grains, b) sample sintered by RPLS at 1240 °C with black arrows indicating remaining fine grains, c) radiation-assisted sintered sample at 1375 °C (note different scalebar), and d) radiation-assisted sintered sample at 1400 °C with cyan arrows indicating secondary phase at triple points.
Fig. 19 SEM micrographs (BSE contrast) of a,b) pure $BaTiO_3$, c,d) 10 vol.% Al_2O_3-reinforced $BaTiO_3$ with white arrows indicating the brighter phase, and e,f) 5 vol.% ZrO_2-reinforced $BaTiO_3$ with black arrows indicating the darker phase.
Fig. 20 SEM micrograph (a) with EDX maps showing the distribution of Al (b) in the microstructure of 10 vol.% of Al_2O_3-reinforced $BaTiO_3$.
Fig. 21 SEM micrograph (a) with EDX maps showing the distribution of Zr (b), and Ti (c) in the microstructure of 5 vol.% of ZrO_2-reinforced $BaTiO_3$.
Fig. 22 XRD patterns of $BaTiO_3$ ceramics reinforced with a-c) Al_2O_3 and d-f) ZrO_2.
Fig. 23 Relative density of $BaTiO_3$-based sintered ceramics reinforced with Al_2O_3 or ZrO_2.
Fig. 24 Piezoelectric coefficient d_{33} of Al_2O_3-reinforced $BaTiO_3$ sintered composites.
Fig. 25 Propagating crack through the 5 vol.% Al_2O_3-reinforced $BaTiO_3$.
Fig. 26 Dilatometric data from sintering a 3:1 molar ratio of Al_2O_3:$BaTiO_3$ green body.
Fig. 27 XRD patterns of 3:1 molar ratio of Al_2O_3:$BaTiO_3$ green body, samples conventionally sintered at 1250 °C and 1450 °C, and sample sintered by SPS at 1450 °C.

8 Glossary

AGG	Abnormal grain growth
BCZT	$(Ba, Ca)(Zr, Ti)O_3$
BET	Brunauer-Emmett-Teller method
CIP	Cold isostatic pressing
CTE	Coefficient of thermal expansion
d_{33}	Indirect piezoelectric constant [pm/V]
DCSBD	Diffuse coplanar surface barrier discharge
DSC	Differential scanning calorimetry
ε_r	Relative permittivity [-]
E	Young's modulus [GPa]
EBSD	Electron backscatter diffraction
EDX	Energy dispersive X-ray spectroscopy
EPD	Electrophoretic deposition
EPR	Electron paramagnetic resonance
G	Shear modulus [GPa]
GB	Grain boundary
HA	Hydroxyapatite
HV	Vickers hardness [GPa]
ICSD	Inorganic Crystal Structure Database
K_{IC}	Fracture toughness [$MPa \cdot m^{1/2}$]
MCAA	Monochloracetic acid
MGS	Mean grain size [µm]
MS	Mass spectroscopy
PEG	Polyethylene glycol
ρ	Relative density [%]
RPLS	Rapid pressure-less sintering
rps	Revolutions per second
rpm	Revolutions per minute
SEM	Scanning electron microscopy
SETOV	Single electron trapped in the oxygen vacancy
SPS	Spark plasma sintering
tan δ	Dielectric loss [-]
T_C	Curie temperature [°C]
TD	Theoretical density [%]
TG	Thermogravimetry
XPS	X-ray photoelectron spectroscopy
XRD	X-ray diffractometry

9 References

[1] C.B. Carter, M.G. Norton, Ceramic Materials, Springer New York, New York, NY, 2013. https://doi.org/10.1007/978-1-4614-3523-5.

[2] Somiya S., Handbook of Advanced Ceramics, Elsevier, 2013. https://doi.org/10.1016/C2010-0-66261-4.

[3] G.B. Olson, Computational design of hierarchically structured materials, Science (1979) 277 (1997) 1237–1242. https://doi.org/10.1126/science.277.5330.1237.

[4] X. Kuang, G. Carotenuto, L. Nicolais, A Review of Ceramic Sintering and Suggestions on Reducing Sintering Temperatures, Adv Perform Mater 4 (1997) 257–274. https://doi.org/https://doi.org/10.1023/A:1008621020555.

[5] S. Adireddy, C. Lin, B. Cao, W. Zhou, G. Caruntu, Solution-based growth of monodisperse cube-like $BaTiO_3$ colloidal nanocrystals, Chem Mater 22 (2010) 1946–1948. https://doi.org/10.1021/cm9038768.

[6] Z. Szalay, K. Bodisova, H. Palkova, P. Svancarek, P. Durina, J. Rahel, A. Zahoranova, D. Galusek, Atmospheric pressure air plasma treated alumina powder for ceramic sintering, Ceram Int 40 (2014) 12737–12743. https://doi.org/10.1016/j.ceramint.2014.04.124.

[7] S.L. Kang, Sintering: Densification, Grain Growth, and Microstructure, Elsevier, 2005. https://doi.org/10.1016/B978-0-7506-6385-4.X5000-6.

[8] B. Budiansky, J.W. Hutchinson, A.G. Evans, Matrix fracture in fiber-reinforced ceramics, J Mech Phys Solids 34 (1986) 167–189. https://doi.org/10.1016/0022-5096(86)90035-9.

[9] Krenkel W., Ceramic Matrix Composites, 1st ed., Wiley, 2008. https://doi.org/10.1002/9783527622412.

[10] T. Chartier, D. Merle, J.L. Besson, Laminar ceramic composites, J Eur Ceram Soc 15 (1995) 101–107. https://doi.org/10.1016/0955-2219(95)93055-8.

[11] K. Niihara, New Design Concept of Structural Ceramics, Journal of the Ceramic Society of Japan 99 (1991) 974–982. https://doi.org/10.2109/jcersj.99.974.

[12] H. Hadraba, Z. Chlup, D. Drdlik, F. Siska, Characterisation of mechanical and fracture behaviour of $Al_2O_3/ZrO_2/BaTiO_3$ laminate by indentation, J Eur Ceram Soc 40 (2020) 4799–4807. https://doi.org/10.1016/j.jeurceramsoc.2020.04.024.

[13] P. Tofel, Z. Machu, Z. Chlup, H. Hadraba, D. Drdlik, O. Sevecek, Z. Majer, V. Holcman, Z. Hadas, Novel layered architecture based on $Al_2O_3/ZrO_2/BaTiO_3$ for SMART piezoceramic electromechanical converters, Eur Phys J Spec Top 228 (2019) 1575–1588. https://doi.org/10.1140/epjst/e2019-800153-0.

[14] J. Jeong, J.H. Kim, J.H. Shim, N.S. Hwang, C.Y. Heo, Bioactive calcium phosphate materials and applications in bone regeneration, Biomater Res 23 (2019). https://doi.org/10.1186/s40824-018-0149-3.

[15] C.D. Friedman, P.D. Costantino, S. Takagi, L.C. Chow, Bonesource(TM) hydroxyapatite cement: A novel biomaterial for craniofacial skeletal tissue engineering and reconstruction, in: J Biomed Mater Res, John Wiley & Sons Inc, 1998: pp. 428–432. https://doi.org/10.1002/(SICI)1097-4636(199824)43:4<428::AID-JBM10>3.0.CO;2-0.

[16] R. Dekker, J. De Bruijn, I. Van Den Brink, Y. Bovell, P. Layrolle, C. Van Blitterswijk, Bone tissue engineering on calcium phosphate-coated titanium plates utilizing cultured rat bone marrow cells: a preliminary study, J Mater Sci Mater Med 9 (1998) 859–863. https://doi.org/10.1023/A:1008956430697.

[17] M.E. Norman, H.M. Elgendy, E.C. Shors, S.F. El-Amin, C.T. Laurencin, An in-vitro evaluation of coralline porous hydroxyapatite as a scaffold for osteoblast growth, Clin Mater 17 (1994) 85–91. https://doi.org/10.1016/0267-6605(94)90016-7.

[18] S. Bose, S. Tarafder, Calcium phosphate ceramic systems in growth factor and drug delivery for bone tissue engineering: A review, Acta Biomater 8 (2012) 1401–1421. https://doi.org/10.1016/j.actbio.2011.11.017.
[19] P.A. Ramires, Biological behavior of sol-gel coated dental implants, J Mater Sci Mater Med 14 (2003) 539–545. https://doi.org/10.1023/A:1023412131314.
[20] A. Dey, A.K. Mukhopadhyay, S. Gangadharan, M.K. Sinha, D. Basu, N.R. Bandyopadhyay, Nanoindentation study of microplasma sprayed hydroxyapatite coating, Ceram Int 35 (2009) 2295–2304. https://doi.org/10.1016/j.ceramint.2009.01.002.
[21] L.P. Prisco, P.I. Ponton, M. V. Guaman, R.R. Avillez, C.P. Romao, M.B. Johnson, M.A. White, B.A. Marinkovic, Assessment of the Thermal Shock Resistance Figures of Merit of $Al_2W_3O_{12}$, a Low Thermal Expansion Ceramic, J Am Ceram Soc 99 (2016) 1742–1748. https://doi.org/10.1111/jace.14160.
[22] K.J. Miller, C.P. Romao, M. Bieringer, B.A. Marinkovic, L. Prisco, M.A. White, Near-Zero Thermal Expansion in $In(HfMg)_{0.5}Mo_3O_{12}$, J Am Ceram Soc 96 (2013) 561–566. https://doi.org/10.1111/jace.12085.
[23] B.A. Marinkovic, P.I. Ponton, C.P. Romao, T. Moreira, M.A. White, Negative and Near-Zero Thermal Expansion in $A_2M_3O_{12}$ and Related Ceramic Families: A Review, Front Mater 8 (2021). https://doi.org/10.3389/fmats.2021.741560.
[24] J.S.O. Evans, T.A. Mary, A.W. Sleight, Negative Thermal Expansion in $Sc_2(WO_4)_3$, J Solid State Chem 137 (1998) 148–160. https://doi.org/10.1006/jssc.1998.7744.
[25] J.S.O. Evans, T.A. Mary, Structural phase transitions and negative thermal expansion in $Sc_2(MoO_4)_3$, International Journal of Inorganic Materials 2 (2000) 143–151. https://doi.org/10.1016/S1466-6049(00)00012-X.
[26] B.A. Marinkovic, M. Ari, R.R. de Avillez, F. Rizzo, F.F. Ferreira, K.J. Miller, M.B. Johnson, M.A. White, Correlation between AO_6 Polyhedral Distortion and Negative Thermal Expansion in Orthorhombic $Y_2Mo_3O_{12}$ and Related Materials, Chemistry of Materials 21 (2009) 2886–2894. https://doi.org/10.1021/cm900650c.
[27] L.P. Prisco, C.P. Romao, F. Rizzo, M.A. White, B.A. Marinkovic, The effect of microstructure on thermal expansion coefficients in powder-processed $Al_2Mo_3O_{12}$, J Mater Sci 48 (2013) 2986–2996. https://doi.org/10.1007/s10853-012-7076-9.
[28] K.F. Etzold, R.A. Roy, K.L. Saenger, J.J. Cuomo, Electrical and Mechanical Properties of PZT Films, MRS Proceedings 200 (1990) 297. https://doi.org/10.1557/PROC-200-297.
[29] A.J. Bell, O. Deubzer, Lead-free piezoelectrics - The environmental and regulatory issues, MRS Bull 43 (2018) 581–587. https://doi.org/10.1557/mrs.2018.154.
[30] T. Tanaka, Barium Titanate Ceramics and their Applications, Bull Inst Chem Res, Kyoto Univ 32 (1954) 43–53.
[31] T. Takenaka, Lead-free piezo-ceramics, in: Advanced Piezoelectric Materials, Elsevier, 2010: pp. 130–170. https://doi.org/10.1533/9781845699758.1.130.
[32] Directive 2011/65/EU "Restriction of the use of certain hazardous substances in electrical and electronic equipment (RoHS)," Official Journal of the European Union (2011).
[33] C.A. Randall, R.E. Newnham, L.E. Cross, History of the First Ferroelectric Oxide, $BaTiO_3$, 2004.
[34] L.L. da Silva, M. Hinterstein, Size Effect on Ferroelectricity in Nanoscaled $BaTiO_3$, in: Technological Applications of Nanomaterials, 2022: pp. 123–133. https://doi.org/10.1007/978-3-030-86901-4_7.
[35] M. Acosta, N. Novak, V. Rojas, S. Patel, R. Vaish, J. Koruza, G.A. Rossetti, J. Rödel, $BaTiO_3$-based piezoelectrics: Fundamentals, current status, and perspectives, Appl Phys Rev 4 (2017). https://doi.org/10.1063/1.4990046.

[36] V. Buscaglia, C.A. Randall, Size and scaling effects in barium titanate. An overview, J Eur Ceram Soc 40 (2020) 3744–3758. https://doi.org/10.1016/j.jeurceramsoc.2020.01.021.
[37] S. Wada, A. Yazawa, T. Hoshina, Y. Kameshima, H. Kakemoto, T. Tsurumi, Y. Kuroiwa, Preparation of barium titanate nanoparticle sphere arrays and their dielectric properties, IEEE Trans Ultrason Ferroelectr Freq Control 55 (2008) 1895–1898. https://doi.org/10.1109/TUFFC.880.
[38] H. Yamaguchi, H. Uwe, T. Sakudo, E. Sawaguchi, Raman-Scattering Study of the Soft Phonon Modes in Hexagonal Barium Titanate, J Physical Soc Japan 56 (1987) 589–595. https://doi.org/10.1143/JPSJ.56.589.
[39] T. Hoshina, S. Hatta, H. Takeda, T. Tsurumi, Grain size effect on piezoelectric properties of $BaTiO_3$ ceramics, Jpn J Appl Phys 57 (2018). https://doi.org/10.7567/JJAP.57.0902BB.
[40] T. Hoshina, Size effect of barium titanate: fine particles and ceramics, Journal of the Ceramic Society of Japan 121 (2013) 156–161. https://doi.org/10.2109/jcersj2.121.156.
[41] L. Lemos Da Silva, K.Y. Lee, S. Petrick, M. Etter, A. Schökel, C.G. Chaves, N. Oliveira Da Silva, K. V. Lalitha, G. Picht, M.J. Hoffmann, M. Hinterstein, Uncovering the symmetry of the induced ferroelectric phase transformation in polycrystalline barium titanate, J Appl Phys 130 (2021). https://doi.org/10.1063/5.0068703.
[42] V. Bijalwan, I. Sokolov, P. Tofel, Poling procedures and piezoelectric response of $(Ba_{0.85}Ca_{0.15}Zr_{0.1}T_{0.9})O_3$ ceramics, J Asian Ceram Soc 9 (2021) 206–213. https://doi.org/10.1080/21870764.2020.1860438.
[43] V. Bijalwan, P. Tofel, Z. Spotz, K. Částková, D. Sobola, J. Erhart, K. Maca, Processing of $0.55(Ba_{0.9}Ca_{0.1})TiO_3$-$0.45Ba(Sn_{0.2}Ti_{0.8})O_3$ lead-free ceramics with high piezoelectricity, J Am Ceram Soc 103 (2020) 4611–4624. https://doi.org/10.1111/jace.17090.
[44] D. Drdlik, D. Zeman, P. Tofel, Z. Chlup, H. Hadraba, K. Drdlikova, A comparative study of direct and indirect evaluation of piezoelectric properties of electrophoreticaly deposited (Ba, Ca) (Zr, Ti)O_3 lead-free piezoceramics, Ceram Int 47 (2021) 2034–2042. https://doi.org/10.1016/j.ceramint.2020.09.035.
[45] I. Coondoo, N. Panwar, D. Alikin, I. Bdikin, S.S. Islam, A. Turygin, V.Y. Shur, A.L. Kholkin, A comparative study of structural and electrical properties in lead-free BCZT ceramics: Influence of the synthesis method, Acta Mater 155 (2018) 331–342. https://doi.org/10.1016/j.actamat.2018.05.029.
[46] V. Bijalwan, J. Erhart, Z. Spotz, D. Sobola, V. Prajzler, P. Tofel, K. Maca, Composition driven (Ba,Ca)(Zr,Ti)O_3 lead-free ceramics with large quality factor and energy harvesting characteristics, J Am Ceram Soc 104 (2021) 1088–1101. https://doi.org/10.1111/jace.17497.
[47] Y. Bai, A. Matousek, P. Tofel, V. Bijalwan, B. Nan, H. Hughes, T.W. Button, (Ba,Ca)(Zr,Ti)O_3 lead-free piezoelectric ceramics-The critical role of processing on properties, J Eur Ceram Soc 35 (2015) 3445–3456. https://doi.org/10.1016/j.jeurceramsoc.2015.05.010.
[48] Y. Tian, Y. Gong, D. Meng, H. Deng, B. Kuang, Low-temperature sintering and electric properties of BCT–BZT and BCZT lead-free ceramics, J Mater Sci: Mater Electron 26 (2015) 3750–3756. https://doi.org/10.1007/s10854-015-2898-2.
[49] D.S. Keeble, F. Benabdallah, P.A. Thomas, M. Maglione, J. Kreisel, Revised structural phase diagram of $(Ba_{0.7}Ca_{0.3}TiO_3)$-$(BaZr_{0.2}Ti_{0.8}O_3)$, Appl Phys Lett 102 (2013). https://doi.org/10.1063/1.4793400.
[50] V. Bijalwan, V. Prajzler, J. Erhart, H. Tan, P. Roupcova, D. Sobola, P. Tofel, K. Maca, Rapid pressure-less and spark plasma sintering of $(Ba_{0.85}Ca_{0.15}Zr_{0.1}Ti_{0.9})O_3$ lead-free piezoelectric ceramics, J Eur Ceram Soc 41 (2021) 2514–2523. https://doi.org/10.1016/j.jeurceramsoc.2020.11.029.

[51] S. Rattanachan, Y. Miyashita, Y. Mutoh, Fatigue behavior of Al_2O_3-based composite with $BaTiO_3$ piezoelectric phase, Int J Fatigue 28 (2006) 1413–1419. https://doi.org/10.1016/j.ijfatigue.2006.02.022.
[52] S. Jiansirisomboon, A. Watcharapasorn, Effects of alumina nano-particulates addition on mechanical and electrical properties of barium titanate ceramics, Curr Appl Phys 8 (2008) 48–52. https://doi.org/10.1016/j.cap.2007.04.008.
[53] G.D. Zhan, J. Kuntz, J. Wan, J. Garay, A.K. Mukherjee, Spark-plasma-sintered $BaTiO_3/Al_2O_3$ nanocomposites, Mater Sci Eng A 356 (2003) 443–446. https://doi.org/10.1016/S0921-5093(02)00812-2.
[54] S. Rattanachan, Y. Miyashita, Y. Mutoh, Microstructure and fracture toughness of a spark plasma sintered Al_2O_3-based composite with $BaTiO_3$ particulates, J Eur Ceram Soc 23 (2003) 1269–1276. https://doi.org/10.1016/S0955-2219(02)00294-7.
[55] M.F. Al-Hilli, Structural and dielectric properties of Zr doped $BaTiO_3$ synthesized by microwave assisted chemical route, Iraqi Journal of Science 59 (2018) 96–104. https://doi.org/10.24996/IJS.2018.59.1A.12.
[56] T.R. Armstrong, L.E. Morgens, A.K. Maurice, R.C. Buchanan, Effects of Zirconia on Microstructure and Dielectric Properties of Barium Titanate Ceramics, J Am Ceram Soc 72 (1989) 605–611. https://doi.org/10.1111/j.1151-2916.1989.tb06182.x.
[57] X.M. Chen, B. Yang, A new approach for toughening of ceramics, Mater Lett 33 (1997) 237–240. https://doi.org/10.1016/S0167-577X(97)00107-9.
[58] S. Jiansirisomboon, A. Watcharapasorn, T. Tunkasiri, Fabrication, Microstructure and Mechanical Properties Relations of Ferroelectric Barium Titanate Reinforced with Alumina Micro/Nano Particulates, in: 11th International Ceramics Congress, Trans Tech Publications Ltd, 2006: pp. 2406–2411. https://doi.org/10.4028/www.scientific.net/ast.45.2406.
[59] S. Rattanachan, Y. Miyashita, Y. Mutoh, Effect of polarization on fracture toughness of $BaTiO_3/Al_2O_3$ composites, J Eur Ceram Soc 24 (2004) 775–783. https://doi.org/10.1016/S0955-2219(03)00319-4.
[60] L.P. Prisco, M. Marzano, P.I. Ponton, A.M.L.M. Costa, C.A. da Costa Neto, G. Sweet, C.P. Romao, M.A. White, B.A. Marinkovic, Relationship between sintering methods and physical properties of the low positive thermal expansion material $Al_2W_3O_{12}$, Int J Appl Ceram Technol 16 (2019) 346–356. https://doi.org/10.1111/ijac.13054.
[61] V. Nikolov, I. Koseva, R. Stoyanova, E. Zhecheva, Conditions for preparation of nanosized $Al_2(WO_4)_3$, J Alloys Compd 505 (2010) 443–449. https://doi.org/10.1016/j.jallcom.2010.06.100.
[62] P.W. Voorhees, The theory of Ostwald ripening, J Stat Phys 38 (1985) 231–252. https://doi.org/10.1007/BF01017860.
[63] M. Broseghini, L. Gelisio, M. D'Incau, C.L. Azanza Ricardo, N.M. Pugno, P. Scardi, Modeling of the planetary ball-milling process: The case study of ceramic powders, J Eur Ceram Soc 36 (2016) 2205–2212. https://doi.org/10.1016/j.jeurceramsoc.2015.09.032.
[64] J. Kujawa, W. Kujawski, Functionalization of Ceramic Metal Oxide Powders and Ceramic Membranes by Perfluoroalkylsilanes and Alkylsilanes Possessing Different Reactive Groups: Physicochemical and Tribological Properties, ACS Appl Mater Interfaces 8 (2016) 7509–7521. https://doi.org/10.1021/acsami.5b11975.
[65] L. Pejchalova, J. Rolecek, D. Salamon, Why freeze-casting brings different phase composition of calcium phosphates?, Open Ceram 7 (2021) 100161. https://doi.org/10.1016/j.oceram.2021.100161.
[66] E. Sato, C. Carry, Effect of powder granulometry and pre-treatment on sintering behavior of submicron-grained α-alumina, J Eur Ceram Soc 15 (1995) 9–16. https://doi.org/10.1016/0955-2219(95)91294-X.

[67] P.A. Jha, A.K. Jha, Enhancement of electrical properties and blue emission due to nanostructuring of $BaZr_{0.05}Ti_{0.95}O_3$ ferroelectric ceramics, J Mater Sci: Mater Electron 25 (2014) 797–804. https://doi.org/10.1007/s10854-013-1648-6.

[68] M. Shu, W. Huang, Y. Qin, D. Wang, S. Li, L. Yin, W. Song, J. Yang, X. Zhu, Y. Sun, Enhanced ferroelectricity in relaxor $0.7BiFeO_3$-0.3 $(Ba_{0.85Ca\ 0.15})TiO_3$ ceramics using ball milling technique, J Mater Sci: Mater Electron 30 (2019) 20221–20228. https://doi.org/10.1007/s10854-019-02406-6.

[69] K.K. Rahangdale, S. Ganguly, Microstructural properties of lead free $BiMnO_3$ ceramic prepared by mechanochemical synthesis, in: IOP Conf Ser Mater Sci Eng, IOP Publishing Ltd, 2019. https://doi.org/10.1088/1757-899X/577/1/012162.

[70] X.J. Liu, Z.Y. Huang, X.P. Pu, X.W. Sun, L.P. Huang, Influence of planetary high-energy ball milling on microstructure and mechanical properties of silicon nitride ceramics, J Am Ceram Soc 88 (2005) 1323–1326. https://doi.org/10.1111/j.1551-2916.2005.00227.x.

[71] D. Drdlik, T. Moravek, J. Rahel, M. Stupavska, J. Cihlar, K. Drdlikova, K. Maca, Electrophoretic deposition of plasma activated sub-micron alumina powder, Ceram Int 44 (2018) 9787–9793. https://doi.org/10.1016/j.ceramint.2018.02.215.

[72] P. Sarkar, P.S. Nicholson, Electrophoretic Deposition (EPD): Mechanisms, Kinetics, and Application to Ceramics, J Am Ceram Soc 79 (1996) 1987–2002. https://doi.org/10.1111/j.1151-2916.1996.tb08929.x.

[73] D. Drdlik, M. Slama, H. Hadraba, K. Drdlikova, J. Cihlar, Physical, mechanical, and biological properties of electrophoretically deposited lithium-doped calcium phosphates, Ceram Int 44 (2018) 2884–2891. https://doi.org/10.1016/j.ceramint.2017.11.035.

[74] J. Ma, C. Wang, K.W. Peng, Electrophoretic deposition of porous hydroxyapatite scaffold, Biomater 24 (2003) 3505–3510. https://doi.org/10.1016/S0142-9612(03)00203-5.

[75] D. Drdlik, V. Marak, K. Maca, K. Drdlikova, Modification of barium titanate sintering via rare earth oxides addition: Dilatometric and microstructural study, Ceram Int 48 (2022) 24599–24608. https://doi.org/10.1016/j.ceramint.2022.05.105.

[76] K. Maca, V. Pouchly, A.R. Boccaccini, Sintering densification curve: A practical approach for its construction from dilatometric shrinkage data, Sci Sinter 40 (2008) 117–122. https://doi.org/10.2298/SOS0802117M.

[77] T. Hoshina, Y. Kigoshi, T. Furuta, H. Takeda, T. Tsurumi, Shrinkage behaviors and sintering mechanism of $BaTiO_3$ ceramics in two-step sintering, Jpn J Appl Phys 50 (2011). https://doi.org/10.1143/JJAP.50.09NC07.

[78] E. Dul'kin, I. Raevski, Influence of conductivity on BaTiO3 crystals phase transitions: A dilatometric study, Ferroelectrics 239 (2000) 381–387. https://doi.org/10.1080/00150190008213345.

[79] M.L. Huckabee, T.M. Hare, H. Palmour, Rate Controlled Sintering as a Processing Method, in: Processing of Crystalline Ceramics, Springer US, Boston, MA, 1978: pp. 205–215. https://doi.org/10.1007/978-1-4684-3378-4_18.

[80] O. Guillon, J. Gonzalez-Julian, B. Dargatz, T. Kessel, G. Schierning, J. Räthel, M. Herrmann, Field-assisted sintering technology/spark plasma sintering: Mechanisms, materials, and technology developments, Adv Eng Mater 16 (2014) 830–849. https://doi.org/10.1002/adem.201300409.

[81] H. V. Atkinson, S. Davies, Fundamental aspects of hot isostatic pressing: An overview, Metallurgical and Materials Transactions A 31 (2000) 2981–3000. https://doi.org/10.1007/s11661-000-0078-2.

[82] I.-W. Chen, X.-H. Wang, Sintering dense nanocrystalline ceramics without final-stage grain growth, Nature 404 (2000) 168–171. https://doi.org/10.1038/35004548.

[83] K.I. Rybakov, E.A. Olevsky, E. V. Krikun, Microwave sintering: Fundamentals and modeling, J Am Ceram Soc 96 (2013) 1003–1020. https://doi.org/10.1111/jace.12278.

[84] R.I. Todd, Flash Sintering of Ceramics: A Short Review, in: Proceedings of the IV Advanced Ceramics and Applications Conference, Atlantis Press, Paris, 2017: pp. 1–12. https://doi.org/10.2991/978-94-6239-213-7_1.
[85] V. Prajzler, S. Prusa, K. Maca, Rapid pressure-less sintering of fine grained zirconia ceramics: Explanation and elimination of a core-shell structure, J Eur Ceram Soc 39 (2019) 5309–5319. https://doi.org/10.1016/j.jeurceramsoc.2019.07.053.
[86] D. Salamon, K. Maca, Z. Shen, Rapid sintering of crack-free zirconia ceramics by pressure-less spark plasma sintering, Scr Mater 66 (2012) 899–902. https://doi.org/10.1016/j.scriptamat.2012.02.013.
[87] D. Salamon, Z. Shen, Pressure-less spark plasma sintering of alumina, Mater Sci Eng A 475 (2008) 105–107. https://doi.org/10.1016/j.msea.2007.01.162.
[88] E.A. Olevsky, S. Kandukuri, L. Froyen, Consolidation enhancement in spark-plasma sintering: Impact of high heating rates, J Appl Phys 102 (2007) 114913. https://doi.org/10.1063/1.2822189.
[89] D.L. Johnson, Comment on "Temperature-Gradient-Driven Diffusion in Rapid-Rate Sintering," J Am Ceram Soc 73 (1990) 2576–2578. https://doi.org/10.1111/j.1151-2916.1990.tb07642.x.
[90] D.E. Garcia, A.N. Klein, D. Hotza, Advanced ceramics with dense and fine-grained microstructures through fast firing, Rev. Adv. Mater. Sci 30 (2012) 273–281.
[91] B. Vaidhyanathan, K. Annapoorani, J. Binner, R. Raghavendra, Microwave Sintering of Multilayer Integrated Passive Devices, J Am Ceram Soc 93 (2010) 2274–2280. https://doi.org/10.1111/j.1551-2916.2010.03740.x.
[92] D.E. Garcia, J. Seidel, R. Janssen, N. Claussen, Fast firing of alumina, J Eur Ceram Soc 15 (1995) 935–938. https://doi.org/10.1016/0955-2219(95)00071-2.
[93] D.E. Garcia, D. Hotza, R. Janssen, Building a sintering front through fast firing, Int J Appl Ceram Technol 8 (2011) 1486–1493. https://doi.org/10.1111/j.1744-7402.2011.02609.x.
[94] V. Prajzler, D. Salamon, K. Maca, Pressure-less rapid rate sintering of pre-sintered alumina and zirconia ceramics, Ceram Int 44 (2018) 10840–10846. https://doi.org/10.1016/j.ceramint.2018.03.132.
[95] D. Salamon, R. Kalousek, J. Zlámal, K. Maca, Role of conduction and convection heat transfer during rapid crack-free sintering of bulk ceramic with low thermal conductivity, J Eur Ceram Soc 36 (2016) 2955–2959. https://doi.org/10.1016/j.jeurceramsoc.2015.11.034.
[96] M. Casas-Luna, H. Tan, S. Tkachenko, D. Salamon, E.B. Montufar, Enhancement of mechanical properties of 3D-plotted tricalcium phosphate scaffolds by rapid sintering, J Eur Ceram Soc 39 (2019) 4366–4374. https://doi.org/10.1016/j.jeurceramsoc.2019.05.055.
[97] M. Biesuz, L. Spiridigliozzi, M. Frasnelli, G. Dell'Agli, V.M. Sglavo, Rapid densification of Samarium-doped Ceria ceramic with nanometric grain size at 900–1100 °C, Mater Lett 190 (2017) 17–19. https://doi.org/10.1016/j.matlet.2016.12.132.
[98] D. Salamon, R. Kalousek, K. Maca, Z. Shen, Rapid Grain Growth in 3Y-TZP Nanoceramics by Pressure-Assisted and Pressure-Less SPS, J Am Ceram Soc 98 (2015) 3706–3712. https://doi.org/10.1111/jace.13837.
[99] X. Deng, X. Wang, H. Wen, A. Kang, Z. Gui, L. Li, Phase transitions in nanocrystalline barium titanate ceramics prepared by spark plasma sintering, J Am Ceram Soc 89 (2006) 1059–1064. https://doi.org/10.1111/j.1551-2916.2005.00836.x.
[100] V. Bijalwan, V. Prajzler, J. Erhart, H. Tan, P. Roupcova, D. Sobola, P. Tofel, K. Maca, Rapid pressure-less and spark plasma sintering of $(Ba_{0.85}Ca_{0.15}Zr_{0.1}T_{0.9})O_3$ lead-free piezoelectric ceramics, J Eur Ceram Soc 41 (2021) 2514–2523. https://doi.org/10.1016/j.jeurceramsoc.2020.11.029.
[101] T. Takeuchi, M. Tabuchi, H. Kageyama, Y. Suyama, Preparation of dense $BaTiO_3$ ceramics with submicrometer grains by spark plasma sintering, J Am Ceram Soc 82 (1999) 939–943. https://doi.org/10.1111/j.1151-2916.1999.tb01857.x.

[102] W. Luan, L. Gao, H. Kawaoka, T. Sekino, K. Niihara, Fabrication and characteristics of fine-grained BaTiOsub>3</sub> ceramics by spark plasma sintering, Ceram Int 30 (2004) 405–410. https://doi.org/10.1016/S0272-8842(03)00124-X.
[103] V. Buscaglia, M. Viviani, M.T. Buscaglia, P. Nanni, L. Mitoseriu, A. Testino, E. Stytsenko, M. Daglish, Z. Zhao, M. Nygren, Nanostructured barium titanate ceramics, in: Powder Technol, 2004: pp. 24–27. https://doi.org/10.1016/j.powtec.2004.09.016.
[104] A. Kocjan, M. Logar, Z. Shen, The agglomeration, coalescence and sliding of nanoparticles, leading to the rapid sintering of zirconia nanoceramics, Sci Rep 7 (2017). https://doi.org/10.1038/s41598-017-02760-7.
[105] A.K. Hofer, A. Kocjan, R. Bermejo, Templated grain growth in rapid sintered 3D-printed alumina ceramics, Open Ceram 15 (2023). https://doi.org/10.1016/j.oceram.2023.100428.
[106] D. Kuscer, A. Kocjan, M. Majcen, A. Meden, K. Radan, J. Kovač, B. Malič, Evolution of phase composition and microstructure of sodium potassium niobate –based ceramic during pressure-less spark plasma sintering and post-annealing, Ceram Int 45 (2019) 10429–10437. https://doi.org/10.1016/j.ceramint.2019.02.102.
[107] C. Ferraro, E. Garcia-Tunon, S. Barg, M. Miranda, N. Ni, R. Bell, E. Saiz, SiC porous structures obtained with innovative shaping technologies, J Eur Ceram Soc 38 (2018) 823–835. https://doi.org/10.1016/j.jeurceramsoc.2017.09.048.
[108] D. Giuntini, X. Wei, A.L. Maximenko, L. Wei, A.M. Ilyina, E.A. Olevsky, Initial stage of Free Pressureless Spark-Plasma Sintering of vanadium carbide: Determination of surface diffusion parameters, Int J Refract Metals Hard Mater 41 (2013) 501–506. https://doi.org/10.1016/j.ijrmhm.2013.06.009.
[109] D. V. Dudina, A.G. Anisimov, V.I. Mali, N. V. Bulina, B.B. Bokhonov, Smaller crystallites in sintered materials? A discussion of the possible mechanisms of crystallite size refinement during pulsed electric current-assisted sintering, Mater Lett 144 (2015) 168–172. https://doi.org/10.1016/j.matlet.2015.01.042.
[110] D. V. Dudina, M.A. Legan, N. V. Fedorova, A.N. Novoselov, A.G. Anisimov, M.A. Esikov, Structural and mechanical characterization of porous iron aluminide FeAl obtained by pressureless Spark Plasma Sintering, Mater Sci Eng A 695 (2017) 309–314. https://doi.org/10.1016/j.msea.2017.04.051.
[111] B.B. Bokhonov, D. V. Dudina, Preparation of porous materials by Spark Plasma Sintering: Peculiarities of alloy formation during consolidation of Fe@Pt core-shell and hollow Pt(Fe) particles, J Alloys Compd 707 (2017) 233–237. https://doi.org/10.1016/j.jallcom.2016.09.146.
[112] E.B. Montufar, S. Tkachenko, M. Casas-Luna, P. Skarvada, K. Slamecka, S. Diaz-de-la-Torre, D. Koutny, D. Palousek, Z. Koledova, L. Hernández-Tapia, T. Zikmund, L. Celko, J. Kaiser, Benchmarking of additive manufacturing technologies for commercially-pure-titanium bone-tissue-engineering scaffolds: processing-microstructure-property relationship, Addit Manuf 36 (2020). https://doi.org/10.1016/j.addma.2020.101516.
[113] R. Yamanoglu, N. Gulsoy, E.A. Olevsky, H.O. Gulsoy, Production of porous Ti5Al2.5Fe alloy via pressureless spark plasma sintering, J Alloys Compd 680 (2016) 654–658. https://doi.org/10.1016/j.jallcom.2016.04.176.
[114] D.A. Woodcock, P. Lightfoot, C. Ritter, Negative Thermal Expansion in $Y_2(WO_4)_3$, J Solid State Chem 149 (2000) 92–98. https://doi.org/10.1006/jssc.1999.8502.
[115] H. Hadraba, D. Drdlik, Z. Chlup, K. Maca, I. Dlouhy, J. Cihlar, Laminated alumina/zirconia ceramic composites prepared by electrophoretic deposition, J Eur Ceram Soc 32 (2012) 2053–2056. https://doi.org/10.1016/j.jeurceramsoc.2011.09.004.
[116] M. Mendelson, Average Grain Size in Polycrystalline Ceramics, J Am Ceram Soc 52 (1969) 443–446. https://doi.org/10.1111/j.1151-2916.1969.tb11975.x.

[117] D. Li, W. Li, C. Fasel, J. Shen, R. Riedel, Sinterability of the oxynitride $LaTiO_2N$ with perovskite-type structure, J Alloys Compd 586 (2014) 567–573. https://doi.org/10.1016/j.jallcom.2013.10.071.
[118] J. Cech, A. Brablec, M. Cernak, N. Puac, N. Selakovic, Z.Lj. Petrovic, Mass spectrometry of diffuse coplanar surface barrier discharge: influence of discharge frequency and oxygen content in N_2/O_2 mixture*, The European Physical Journal D 71 (2017) 27. https://doi.org/10.1140/epjd/e2016-70607-5.
[119] C.-J. Liao, F.-H. Lin, K.-S. Chen, J.-S. Sun, Thermal decomposition and reconstitution of hydroxyapatite in air atmosphere, Biomater 20 (1999) 1807–1813. https://doi.org/10.1016/S0142-9612(99)00076-9.
[120] J. Cihlar, A. Buchal, M. Trunec, Kinetics of thermal decomposition of hydroxyapatite bioceramics, 1999. https://doi.org/https://doi.org/10.1023/A:1004769820545.
[121] V. Marak, M. Ilcikova, K. Drdlikova, D. Drdlik, Plasma treatment and rapid pressure-less sintering for fabrication of environmentally friendly hydroxyapatite biocoatings, J Eur Ceram Soc 44 (2024) 2590–2599. https://doi.org/10.1016/j.jeurceramsoc.2023.11.044.
[122] S. Myhra, J.C. Riviere, Characterization of Nanostructures, CRC Press, 2012. https://doi.org/10.1201/b12176.
[123] M. Farrokhi-Rad, T. Shahrabi, Effect of suspension medium on the electrophoretic deposition of hydroxyapatite nanoparticles and properties of obtained coatings, Ceram Int 40 (2014) 3031–3039. https://doi.org/10.1016/j.ceramint.2013.10.004.
[124] X. Gui, Z. Tang, W. Fei, Solubility of CO_2 in Alcohols, Glycols, Ethers, and Ketones at High Pressures from (288.15 to 318.15) K, J Chem Eng Data 56 (2011) 2420–2429. https://doi.org/10.1021/je101344v.
[125] S.P. Tonner, M.S. Wainwright, D.L. Trimm, N.W. Cant, Solubility of carbon monoxide in alcohols, J Chem Eng Data 28 (1983) 59–61. https://doi.org/10.1021/je00031a017.
[126] S. Signorelli, M.N. Moller, E.L. Coitino, A. Denicola, Nitrogen dioxide solubility and permeation in lipid membranes, Arch Biochem Biophys 512 (2011) 190–196. https://doi.org/10.1016/j.abb.2011.06.003.
[127] A.W. Shaw, A.J. Vosper, Solubility of nitric oxide in aqueous and nonaqueous solvents, Journal of the Chemical Society, Faraday Transactions 1: Physical Chemistry in Condensed Phases 73 (1977) 1239. https://doi.org/10.1039/f19777301239.
[128] G. Georgiou, J.C. Knowles, J.E. Barralet, Dynamic shrinkage behavior of hydroxyapatite and glass-reinforced hydroxyapatites, J Mater Sci 39 (2004) 2205–2208. https://doi.org/10.1023/B:JMSC.0000017788.20785.ff.
[129] S. Ramesh, K.L. Aw, R. Tolouei, M. Amiriyan, C.Y. Tan, M. Hamdi, J. Purbolaksono, M.A. Hassan, W.D. Teng, Sintering properties of hydroxyapatite powders prepared using different methods, Ceram Int 39 (2013) 111–119. https://doi.org/10.1016/j.ceramint.2012.05.103.
[130] H. Li, K.A. Khor, V. Chow, P. Cheang, Nanostructural characteristics, mechanical properties, and osteoblast response of spark plasma sintered hydroxyapatite, J Biomed Mater Res A 82A (2007) 296–303. https://doi.org/10.1002/jbm.a.31143.
[131] V. Pouchly, J. Rahel, T. Spusta, M. Ilcikova, D. Pavlinak, T. Moravek, K. Maca, Improved microstructure of alumina ceramics prepared from DBD plasma activated powders, J Eur Ceram Soc 39 (2019) 1297–1303. https://doi.org/10.1016/j.jeurceramsoc.2018.11.022.
[132] S. Ramesh, C.Y. Tan, S.B. Bhaduri, W.D. Teng, I. Sopyan, Densification behaviour of nanocrystalline hydroxyapatite bioceramics, J Mater Process Technol 206 (2008) 221–230. https://doi.org/10.1016/j.jmatprotec.2007.12.027.
[133] S. Dasgupta, S. Tarafder, A. Bandyopadhyay, S. Bose, Effect of grain size on mechanical, surface and biological properties of microwave sintered hydroxyapatite, Mater Sci Eng C 33 (2013) 2846–2854. https://doi.org/10.1016/j.msec.2013.03.004.

[134] M.M.A. Ramselaar, F.C.M. Driessens, W. Kalk, J.R. De Wijn, P.J. Van Mullem, Biodegradation of four calcium phosphate ceramics;in vivo rates and tissue interactions, J Mater Sci Mater Med 2 (1991) 63–70. https://doi.org/10.1007/BF00703460.
[135] P.A. Ramires, A. Wennerberg, C.B. Johansson, F. Cosentino, S. Tundo, E. Milella, Biological behavior of sol-gel coated dental implants, n.d. https://doi.org/https://doi.org/10.1023/A:1023412131314.
[136] G.L. Darimont, R. Cloots, E. Heinen, L. Seidel, R. Legrand, In vivo behaviour of hydroxyapatite coatings on titanium implants: a quantitative study in the rabbit, 2002.
[137] C.K. Wang, C.P. Ju, J.H. Chern Lin, Effect of doped bioactive glass on structure and properties of sintered hydroxyapatite, Mater Chem Phys 53 (1998) 138–149. https://doi.org/10.1016/S0254-0584(97)02074-9.
[138] C.Y. Tan, R. Singh, R. Tolouei, I. Sopyan, W.D. Teng, Synthesis of High Fracture Toughness of Hydroxyapatite Bioceramics, Adv Mat Res 264–265 (2011) 1849–1855. https://doi.org/10.4028/www.scientific.net/AMR.264-265.1849.
[139] G. Muralithran, S. Ramesh, The effects of sintering temperature on the properties of hydroxyapatite, Ceram Int 26 (2000) 221–230. https://doi.org/10.1016/S0272-8842(99)00046-2.
[140] C.Y. Tan, K.L. Aw, W.H. Yeo, S. Ramesh, M. Hamdi, I. Sopyan, Influence of Magnesium Doping in Hydroxyapatite Ceramics, in: Proc West Mark Ed Assoc Conf, 2008: pp. 326–329. https://doi.org/10.1007/978-3-540-69139-6_83.
[141] C. Wang, J. Ma, W. Cheng, R. Zhang, Thick hydroxyapatite coatings by electrophoretic deposition, Mater Lett 57 (2002) 99–105. https://doi.org/10.1016/S0167-577X(02)00706-1.
[142] A.K. Lynn, D.L. DuQuesnay, Hydroxyapatite-coated Ti–6Al–4V Part 1: the effect of coating thickness on mechanical fatigue behaviour, Biomater 23 (2002) 1937–1946. https://doi.org/10.1016/S0142-9612(01)00321-0.
[143] N.F. Nuswantoro, I. Budiman, A. Septiawarman, D.H. Tjong, M. Manjas, Gunawarman, Effect of Applied Voltage and Coating Time on Nano Hydroxyapatite Coating on Titanium Alloy Ti6Al4V Using Electrophoretic Deposition for Orthopaedic Implant Application, IOP Conf Ser Mater Sci Eng 547 (2019) 012004. https://doi.org/10.1088/1757-899X/547/1/012004.
[144] Ilhamdi, Gunawarman, J. Affi, O. Susanti, D. Juliadmi, D. Oktaviana, M. Tauhid, Effect of Bilayer Nano-Micro Hydroxyapatite on the Surface Characteristics of Implanted Ti-6Al-4V ELI, International Journal of Automotive and Mechanical Engineering 20 (2023) 10777–10785. https://doi.org/10.15282/ijame.20.3.2023.19.0833.
[145] N.F. Nuswantoro, D. Juliadmi, H. Fajri, M. Manjas, N. Suharti, D.H. Tjong, J. Affi, Gunawarman, Electrophoretic Deposition Performance of Hydroxyapatite Coating on Titanium Alloys for Orthopedic Implant Application, Materials Science Forum 1000 (2020) 69–81. https://doi.org/10.4028/www.scientific.net/MSF.1000.69.
[146] I. Demnati, M. Parco, D. Grossin, I. Fagoaga, C. Drouet, G. Barykin, C. Combes, I. Braceras, S. Goncalves, C. Rey, Hydroxyapatite coating on titanium by a low energy plasma spraying mini-gun, Surf Coat Technol 206 (2012) 2346–2353. https://doi.org/10.1016/j.surfcoat.2011.10.025.
[147] B.-Y. Chou, E. Chang, S.Y. Yao, J.M. Chen, Phase Transformation during Plasma Spraying of Hydroxyapatite-10-wt%-Zirconia Composite Coating, J Am Ceram Soc 85 (2004) 661–669. https://doi.org/10.1111/j.1151-2916.2002.tb00147.x.
[148] A. Surjith, N.K. James, R. Ratheesh, Synthesis, structural and microwave dielectric properties of $Al_2W_{3-x}Mo_xO_{12}$ (x=0–3) ceramics, J Alloys Compd 509 (2011) 9992–9995. https://doi.org/10.1016/j.jallcom.2011.08.007.
[149] M. Marzano, P.I. Ponton, A.R.J. Barreto, B.A. Marinkovic, Non-hydrolytic sol-gel synthesis of $Al_2W_3O_{12}$ nanopowders, J Solgel Sci Technol 104 (2022) 267–275. https://doi.org/10.1007/s10971-022-05934-6.

[150] V. Marak, M. Diniz Rocha Henriques, B.A. Marinkovic, D. Drdlik, Rapid densification of low-positive thermal expansion $Al_2W_3O_{12}$ ceramics, J Eur Ceram Soc 44 (2024) 6548–6555. https://doi.org/10.1016/j.jeurceramsoc.2024.04.036.
[151] L. Fu, H. Chen, K. Wang, X. Wang, Oxygen-vacancy generation in $MgFe_2O_4$ by high temperature calcination and its improved photocatalytic activity for CO_2 reduction, J Alloys Compd 891 (2022) 161925. https://doi.org/10.1016/j.jallcom.2021.161925.
[152] P.I. Ponton, L.P. Prisco, A. Dosen, G.S. Faro, M.A.S. de Abreu, B.A. Marinkovic, Co-precipitation synthesis of $Y_2W_3O_{12}$ submicronic powder, Ceram Int 43 (2017) 4222–4228. https://doi.org/10.1016/j.ceramint.2016.12.055.
[153] M. Pudukudy, Z. Yaakob, R. Rajendran, T. Kandaramath, Photodegradation of methylene blue over novel 3D ZnO microflowers with hexagonal pyramid-like petals, Reaction Kinetics, Mechanisms and Catalysis 112 (2014) 527–542. https://doi.org/10.1007/s11144-014-0703-5.
[154] I. Gomez, E.M. Otazo, H. Hernandez, E. Rubio, J. Varela, M. Ramírez, I. Barajas, A.J. Gordillo, Thermal degradation study of PVA derivative with pendant phenylthionecarbamate groups by DSC/TGA and GC/MS, Polym Degrad Stab 112 (2015) 132–136. https://doi.org/10.1016/j.polymdegradstab.2014.12.027.
[155] M.D.R. Henriques, V. Marak, J. Gil-Londono, V.T. Santana, P. Neugebauer, D. Drdlik, B.A. Marinkovic, Extrinsic Oxygen Vacancies Formation during Crystallization of $Al_2W_3O_{12}$ by Calcination in Air, The Journal of Physical Chemistry C 127 (2023) 22425–22434. https://doi.org/10.1021/acs.jpcc.3c06264.
[156] I. Yanase, R. Ootomo, H. Kobayashi, Effect of B substitution on thermal changes of UV–Vis and Raman spectra and color of $Al_2W_3O_{12}$ powder, J Therm Anal Calorim 132 (2018) 1–6. https://doi.org/10.1007/s10973-017-6933-9.
[157] W. Paraguassu, M. Maczka, A.G.S. Filho, P.T.C. Freire, F.E.A. Melo, J.M. Filho, J. Hanuza, A comparative study of negative thermal expansion materials $Sc_2(MoO_4)_3$ and $Al_2(WO_4)_3$ crystals, Vib Spectrosc 44 (2007) 69–77. https://doi.org/10.1016/j.vibspec.2006.08.006.
[158] S. Chan, I.E. Wachs, L.L. Murrell, Relative raman cross-sections of tungsten oxides: $6WO_3$, $Al_2(WO_4)_3$ and WO_3/Al_2O_3, J Catal 90 (1984) 150–155. https://doi.org/10.1016/0021-9517(84)90096-4.
[159] E.C. Moreno Diaz, M.E. Maia Da Costa, W. Paraguassu, K. Krambrock, A. Dosen, M.B. Johnson, M.A. White, B.A. Marinkovic, Extrinsic Point Defects in Low-Positive Thermal Expansion $Al_2W_3O_{12}$ and Their Effects on Thermal and Optical Properties, Inorg Chem 61 (2022) 14086–14094. https://doi.org/10.1021/acs.inorgchem.2c02113.
[160] M. Tsvetkov, D. Elenkova, M. Milanova, Luminescence Properties of $Gd_2(MoO_4)_3$ Modified with Sm(III) and Tb(III) for Potential LED Applications, Crystals (Basel) 12 (2022) 120. https://doi.org/10.3390/cryst12010120.
[161] Y. Liang, Y.-G. Cheng, X.-H. Ge, B.-H. Yuan, J. Guo, Q. Sun, E.-J. Liang, Negative thermal expansion and photoluminescence in solid solution $(HfSc)_{0.83}W_{2.25}P_{0.83}O_{12-\delta}$, Chinese Physics B 26 (2017) 106501. https://doi.org/10.1088/1674-1056/26/10/106501.
[162] L. Zhou, H. Zhang, H. Zhang, Z. Zhang, Homogeneous nanoparticle dispersion prepared with impurity-free dispersant by the ball mill technique, Particuology 11 (2013) 441–447. https://doi.org/10.1016/j.partic.2013.01.001.
[163] R. Oberacker, Powder Compaction by Dry Pressing, in: Ceramics Science and Technology, Wiley, 2011: pp. 1–37. https://doi.org/10.1002/9783527631957.ch1.
[164] P.M. Jardim, E.S. Garcia, B.A. Marinkovic, Young′s modulus, hardness and thermal expansion of sintered $Al_2W_3O_{12}$ with different porosity fractions, Ceram Int 42 (2016) 5211–5217. https://doi.org/10.1016/j.ceramint.2015.12.045.

[165] F.J.T. Lin, L.C. De Jonghe, M.N. Rahaman, Microstructure Refinement of Sintered Alumina by a Two-Step Sintering Technique, n.d.
[166] W.D. Kingery, H.K. Bowen, D.R. Ulhmann, Introduction to Ceramics, Wiley, New York, 1975.
[167] I. Koseva, A. Yordanova, V. Nikolov, High-Density Ceramics of $Al_{2-x}Me_x(WO_4)_3$, (Me = Sc or In) Solid Solutions, New Journal of Glass and Ceramics 03 (2013) 104–110. https://doi.org/10.4236/njgc.2013.34017.
[168] A. Yordanova, V. Nikolov, I. Koseva, Fabrication of high density cramics from $Al_{2-x}In_x(WO_4)_3$ solid solutions, Journal of Chemical Technology and Metallurgy 50 (2015) 537–542.
[169] N. Imanaka, M. Hiraiwa, G. Adachi, H. Dabkowska, A. Dabkowski, Thermal contraction behavior in $Al_2(WO_4)_3$ single crystal, J Cryst Growth 220 (2000) 176–179. https://doi.org/10.1016/S0022-0248(00)00771-5.
[170] J.A. Wollmershauser, B.N. Feigelson, E.P. Gorzkowski, C.T. Ellis, R. Goswami, S.B. Qadri, J.G. Tischler, F.J. Kub, R.K. Everett, An extended hardness limit in bulk nanoceramics, Acta Mater 69 (2014) 9–16. https://doi.org/10.1016/j.actamat.2014.01.030.
[171] S.J. Dillon, M. Tang, W.C. Carter, M.P. Harmer, Complexion: A new concept for kinetic engineering in materials science, Acta Mater 55 (2007) 6208–6218. https://doi.org/10.1016/j.actamat.2007.07.029.
[172] M. Baurer, M. Syha, D. Weygand, Combined experimental and numerical study on the effective grain growth dynamics in highly anisotropic systems: Application to barium titanate, Acta Mater 61 (2013) 5664–5673. https://doi.org/10.1016/j.actamat.2013.06.007.
[173] Q. Xu, Z. Li, Dielectric and ferroelectric behaviour of Zr-doped BaTiO3 perovskites, Processing and Application of Ceramics 14 (2020) 188–194. https://doi.org/10.2298/pac2003188x.
[174] J.E. Burke, Recrystallization and Sintering in Ceramics, in: Sintering Key Papers, Springer Netherlands, Dordrecht, 1990: pp. 17–38. https://doi.org/10.1007/978-94-009-0741-6_2.
[175] W. Rheinheimer, M.J. Hoffmann, Grain growth transitions of perovskite ceramics and their relationship to abnormal grain growth and bimodal microstructures, J Mater Sci 51 (2016) 1756–1765. https://doi.org/10.1007/s10853-015-9535-6.
[176] K.W. Kirby, B.A. Wechsler, Phase relations in the Barium Titanate—Titanium Oxide System, J Am Ceram Soc 74 (1991) 1841–1847. https://doi.org/10.1111/j.1151-2916.1991.tb07797.x.
[177] J.G. Fisher, B.K. Lee, S.Y. Choi, S.M. Wang, S.J.L. Kang, Inhibition of abnormal grain growth in $BaTiO_3$ by addition of Al_2O_3, J Eur Ceram Soc 26 (2006) 1619–1628. https://doi.org/10.1016/j.jeurceramsoc.2005.03.234.
[178] H. -Y Lu, J. -S Bow, W. -H Deng, Core-Shell Structures in ZrO2-Modified $BaTiO_3$ Ceramic, J Am Ceram Soc 73 (1990) 3562–3568. https://doi.org/10.1111/j.1151-2916.1990.tb04258.x.
[179] J.P. Guha, Subsolidus equilibria in the system BaO-TiO_2-Al_2O_3, J Solid State Chem 34 (1980) 17–22. https://doi.org/10.1016/0022-4596(80)90397-7.
[180] T.R. Armstrong, R.C. Buchanan, Influence of Core-Shell Grains on the Internal Stress State and Permittivity Response of Zirconia-Modified Barium Titanate, J Am Ceram Soc 73 (1990) 1268–1273. https://doi.org/10.1111/j.1151-2916.1990.tb05190.x.
[181] P.S. Dobal, A. Dixit, R.S. Katiyar, Z. Yu, R. Guo, A.S. Bhalla, Micro-Raman scattering and dielectric investigations of phase transition behavior in the BaTiO3-BaZrO3 system, J Appl Phys 89 (2001) 8085–8091. https://doi.org/10.1063/1.1369399.
[182] R.D. Shannon, Revised effective ionic radii and systematic studies of interatomic distances in halides and chalcogenides, Acta Crystallographica Section A 32 (1976) 751–767. https://doi.org/10.1107/S0567739476001551.
[183] C. Laulhe, F. Hippert, J. Kreisel, A. Pasturel, A. Simon, J.-L. Hazemann, R. Bellissent, G.J. Cuello, Random local strain effects in the relaxor ferroelectric $BaTi_{1-x}Zr_xO_3$: experimental and theoretical

investigation, Phase Transitions 84 (2011) 438–452. https://doi.org/10.1080/01411594.2010.547153.
[184] Y. Huan, X. Wang, J. Fang, L. Li, Grain size effects on piezoelectric properties and domain structure of BaTiO 3 ceramics prepared by two-step sintering, J Am Ceram Soc 96 (2013) 3369–3371. https://doi.org/10.1111/jace.12601.
[185] D. Ghosh, A. Sakata, J. Carter, P.A. Thomas, H. Han, J.C. Nino, J.L. Jones, Domain wall displacement is the origin of superior permittivity and piezoelectricity in $BaTiO_3$ at intermediate grain sizes, Adv Funct Mater 24 (2014) 885–896. https://doi.org/10.1002/adfm.201301913.
[186] T. Karaki, K. Yan, M. Adachi, Subgrain microstructure in high-performance $BaTiO_3$ piezoelectric ceramics, Applied Physics Express 1 (2008) 1114021–1114023. https://doi.org/10.1143/APEX.1.111402.
[187] P. Zheng, J.L. Zhang, Y.Q. Tan, C.L. Wang, Grain-size effects on dielectric and piezoelectric properties of poled $BaTiO_3$ ceramics, Acta Mater 60 (2012) 5022–5030. https://doi.org/10.1016/j.actamat.2012.06.015.
[188] P.F. Becher, Microstructural Design of Toughened Ceramics, J Am Ceram Soc 74 (1991) 255–269. https://doi.org/10.1111/j.1151-2916.1991.tb06872.x.
[189] M. Radovic, E. Lara-Curzio, L. Riester, Comparison of different experimental techniques for determination of elastic properties of solids, Mater Sci Eng A 368 (2004) 56–70. https://doi.org/10.1016/j.msea.2003.09.080.
[190] Z. Chlup, D. Drdlik, H. Hadraba, O. Ševecek, F. Šiska, J. Erhart, K. Maca, Temperature effect on elastic and fracture behaviour of lead-free piezoceramic $BaTiO_3$, J Eur Ceram Soc 43 (2023) 1509–1522. https://doi.org/10.1016/j.jeurceramsoc.2022.11.030.
[191] J. Kubler, Fracture Toughness of Ceramics Using the SEVNB Method a Joint VAMSA/ESIS Round Robin, in: Fracture Mechanics of Ceramics, Springer US, Boston, MA, 2002: pp. 437–445. https://doi.org/10.1007/978-1-4757-4019-6_33.
[192] K. Ganesh Kumar, P. Balaji Bhargav, K. Aravinth, C. Balaji, Enhanced photoluminescence properties of $BaAl_2O_4$: Ce3+/Li+ yellow phosphors, J Mater Sci: Mater Electron 33 (2022) 15323–15332. https://doi.org/10.1007/s10854-022-08416-1.
[193] C.M.B. Henderson, D. Taylor, The structural behaviour of the nepheline family: (1) Sr and Ba aluminates (MAl_2O_4), Mineral Mag 45 (1982) 111–127. https://doi.org/10.1180/minmag.1982.045.337.13.
[194] H. Sui-Yang, R. Von Der Muhll, J. Ravez, M. Couzi, Phase transition and symmetry in $BaAl_2O_4$, Ferroelectrics 159 (1994) 127–132. https://doi.org/10.1080/00150199408007560.
[195] D. Kuscer, I. Bantan, M. Hrovat, B. Malic, The microstructure, coefficient of thermal expansion and flexural strength of cordierite ceramics prepared from alumina with different particle sizes, J Eur Ceram Soc 37 (2017) 739–746. https://doi.org/10.1016/j.jeurceramsoc.2016.08.032.
[196] Y. He, Heat capacity, thermal conductivity, and thermal expansion of barium titanate-based ceramics, Thermochim Acta 419 (2004) 135–141. https://doi.org/10.1016/j.tca.2004.02.008.
[197] S.J. Bull, T.F. Page, E.H. Yoffe, An explanation of the indentation size effect in ceramics, Philos Mag Lett 59 (1989) 281–288. https://doi.org/10.1080/09500839008206356.
[198] M. Radovic, E. Lara-Curzio, L. Riester, Comparison of different experimental techniques for determination of elastic properties of solids, Mater Sci Eng A 368 (2004) 56–70. https://doi.org/10.1016/j.msea.2003.09.080.
[199] J.M. Blamey, T. V. Parry, Strength and toughness of barium titanate ceramics, J Mater Sci 28 (1993) 4988–4993. https://doi.org/10.1007/BF00361166.
[200] Z. Chlup, H. Hadraba, L. Slabakova, D. Drdlik, I. Dlouhy, Fracture behaviour of alumina and zirconia thin layered laminate, J Eur Ceram Soc 32 (2012) 2057–2061. https://doi.org/10.1016/j.jeurceramsoc.2011.09.006.

[201] R.M. Spriggs, J.B. Mitchell, T. Vasilos, Mechanical Properties of Pure, Dense Aluminum Oxide as a Function of Temperature and Grain Size, J Am Ceram Soc 47 (1964) 323–327. https://doi.org/10.1111/j.1151-2916.1964.tb12994.x.
[202] X. Lu, B. Huang, T. Chen, Z. Fu, Z. Wang, L. Wang, Q. Zhang, Effects of ZnO additive on crystalline phase and microwave dielectric properties of $0.90Al_2O_3$–$0.10TiO_2$ ceramics, J Mater Sci: Mater Electron 27 (2016) 2687–2692. https://doi.org/10.1007/s10854-015-4078-9.
[203] S. Wada, K. Takeda, T. Muraishi, H. Kakemoto, T. Tsurumi, T. Kimura, Preparation of [110] grain oriented barium titanate ceramics by templated grain growth method and their piezoelectric properties, Japanese Journal of Applied Physics, Part 1: Regular Papers and Short Notes and Review Papers 46 (2007) 7039–7043. https://doi.org/10.1143/JJAP.46.7039.
[204] G. Arlt, D. Hennings, G. de With, Dielectric properties of fine-grained barium titanate ceramics, J Appl Phys 58 (1985) 1619–1625. https://doi.org/10.1063/1.336051.
[205] D. Drdlik, V. Marak, H. Hadraba, Z. Chlup, A way for densification of lead-free $BaTiO_3$-based/ZrO_2 laminates for energy harvesting applications prepared by electrophoretic deposition, Mater Lett (2023) 135424. https://doi.org/10.1016/j.matlet.2023.135424.
[206] A.P. Naumenko, N. Berezovska, M.M. Biliy, A.P. Naumenko, N.I. Berezovska, O. V Shevchenko, V. Analysis, R. Spectra, T. Zirconia, Vibrational analysis and Raman spectra of tetragonal Zirconia, Phys Chem Solid State 9 (2008) 121–125.
[207] Y.I. Yuzyuk, Raman scattering spectra of ceramics, films, and superlattices of ferroelectric perovskites: A review, Physics of the Solid State 54 (2012) 1026–1059. https://doi.org/10.1134/S1063783412050502.
[208] T. Takeuchi, C. Capiglia, N. Balakrishnan, Y. Takeda, H. Kageyama, Preparation of Fine-grained BaTiOsub>3</sub> Ceramics by Spark Plasma Sintering, J Mater Res 17 (2002) 575–581. https://doi.org/10.1557/JMR.2002.0081.
[209] B. Li, X. Wang, L. Li, H. Zhou, X. Liu, X. Han, Y. Zhang, X. Qi, X. Deng, Dielectric properties of fine-grained $BaTiO_3$ prepared by spark-plasma-sintering, Mater Chem Phys 83 (2004) 23–28. https://doi.org/10.1016/j.matchemphys.2003.08.009.
[210] V. Bijalwan, P. Tofel, V. Holcman, Grain size dependence of the microstructures and functional properties of $(Ba_{0.85}Ca_{0.15-x}Ce_x)(Zr_{0.1}Ti_{0.9})O_3$ lead-free piezoelectric ceramics, J Asian Ceram Soc 6 (2018) 384–393. https://doi.org/10.1080/21870764.2018.1539211.
[211] A. Di Loreto, R. Machado, A. Frattini, M.G. Stachiotti, Improvement in the sintering process of $Ba_{0.85}Ca_{0.15}Zr_{0.1}Ti_{0.9}O_3$ ceramics by the replacement of Zr by Hf, J Mater Sci: Mater Electron 28 (2017) 588–594. https://doi.org/10.1007/s10854-016-5562-6.
[212] O. Ishai, L.J. Cohen, Elastic properties of filled and porous epoxy composites, Int J Mech Sci 9 (1967) 539–546. https://doi.org/10.1016/0020-7403(67)90053-7.

11 Author's activities and outputs

Coursework

Code	Name	Evaluation	Date
DS444	Academic English for PhD 1	A	14.12.2020
DS446	Friday CEITEC BUT seminar	P	21.12.2020
9SAE	Statistical analysis and experiment	P	02.02.2021
DS214	High-temperature processes in inorganic materials	P	19.11.2020
DS445	Academic English for PhD 2	A	12.05.2021
DS204	Colloids, surface, and catalysis	P	03.06.2021
DS206	Methods of X-ray structural analysis	P	16.07.2021

Internships

2022

Three months at **Forschungszentrum Jülich**, Germany, under the supervision of Prof. Dr. Robert Vaßen

2023

Three weeks at **Jožef Stefan Institute**, Slovenia, under the supervision of Assoc. Prof. Andraž Kocjan

Teaching activities

Introduction to materials science at FME BUT: 2 groups, 4 h/week, 1 semester

Electron microscopy days 2024, BUT Junior 2024, CEITEC Summer School 2024

Mentoring of master's students:

Bc. Ondřej Kučera (FME BUT): Processing and properties of piezo-dielectric ceramic composites

BSc. Marianne Diniz Rocha Henriques (PUC, Rio de Janeiro, Brazil): Consolidation and thermal shock resistance of phases from the $A_2M_3O_{12}$ family

Conferences

14th Conference for Young Scientists in Ceramics (2021), Novi Sad, Serbia Presentation: "*Fabrication and physical, microstructural, and mechanical properties of rare-earth-doped barium titanate ceramics*"

Advanced Ceramics and Applications IX (2021), Belgrade, Serbia Presentation: "*Electrophoretic deposition of plasma-activated hydroxyapatite powder densified by rapid sintering*" – **Best oral presentation award**

Processing and Properties of Advanced Ceramics And Glasses (2022), Mojmírovce, Slovakia Presentation: *"Suspension plasma spraying of barium titanate-based coatings"*

Advanced Ceramics and Applications X (2022), Belgrade, Serbia Presentation: *"Rapid rate sintering of bulk low-positive thermal expansion material $Al_2W_3O_{12}$ for thermal shock resistance applications"*

23rd Conference on Material Science – YUCOMAT (2022), Herceg Novi, Montenegro Presentation: *"Suspension plasma spraying of $BaTiO_3$ and $BaTiO_3/ZrO_2$"* – **Best oral presentation award**

ECerS XVII – Ceramics in Europe (2022), Kraków, Poland Presentation: *"Microstructural evolution of barium titanate at applied non-conventional rapid rate sintering"*

EUROMAT 23 (2023) Frankfurt, Germany Poster: "*Extrinsic point defects in $BaTiO_3$-based ceramics"*

ECerS XVIII (2023), Lyon, France Presentation: "*Properties and performance of rare-earth-doped barium titanate ceramics"*

Projects

Specific research projects as a principal investigator:

2021

Electrophoretic deposition of plasma activated hydroxyapatite powder densified by rapid sintering, VUT-J-21-7198.

2022

Plasma spraying of $BaTiO_3/ZrO_2$ and $BaTiO_3/Al_2O_3$ composite coatings for improved electromechanical properties, VUT-J-22-7926.

Rapid rate sintering of bulk thermomiotic material $Al_2W_3O_{12}$ for thermal shock applications, VUT-J-22-7983.

2023

Oxygen vacancies formation and its influence on electromechanical properties of BaTiO3-based ceramics, VUT-J-23-8308.

Other projects:

8 projects as a part of Research Group Advanced Multifunctional Ceramics (GAČR, TAČR, Horizon Europe, OP JAK)

Publications

Published:

Drdlik, D., Marak, V., Rolecek, J., Drdlikova, K., Kratochvil, J., Salamon, D. (2018). Study of Alumina and Alumina-Silicon Carbide Layered Composite Sintered by SPS. *Key Engineering Materials, 784*, 67–72. https://doi.org/10.4028/www.scientific.net/KEM.784.67

Drdlik, D., Marak, V., Maca, K., Drdlikova, K. (2022). Modification of barium titanate sintering via rare earth oxides addition: Dilatometric and microstructural study. *Ceramics International*, *48*(17), 24599–24608. https://doi.org/10.1016/j.ceramint.2022.05.105 **(Q1 Journal)**

Henriques, M. D. R., Marak, V., Gil-Londono, J., Santana, V. T., Neugebauer, P., Drdlik, D., Marinkovic, B. A. (2023). Extrinsic Oxygen Vacancies Formation during Crystallization of $Al_2W_3O_{12}$ by Calcination in Air. *The Journal of Physical Chemistry C*, *127*(45), 22425–22434. https://doi.org/10.1021/acs.jpcc.3c06264 **(Q1 Journal)**

Drdlik, D., Marak, V., Hadraba, H., Chlup, Z. (2023). A way for densification of lead-free $BaTiO_3$-based/ZrO_2 laminates for energy harvesting applications prepared by electrophoretic deposition. *Materials Letters*, 135424. https://doi.org/10.1016/j.matlet.2023.135424 **(Q2 Journal)**

Marak, V., Ilcikova, M., Drdlikova, K., Drdlik, D. (2024). Plasma treatment and rapid pressure-less sintering for fabrication of environmentally friendly hydroxyapatite biocoatings. *Journal of the European Ceramic Society*, *44*(4), 2590–2599. https://doi.org/10.1016/j.jeurceramsoc.2023.11.044 **(Q1 Journal)**

Marak, V., Henriques, M. D. R., Marinkovic, B. A., Drdlik, D. (2024). Rapid densification of low-positive thermal expansion $Al_2W_3O_{12}$ ceramics. *Journal of the European Ceramic Society*. https://doi.org/10.1016/j.jeurceramsoc.2024.04.036 **(Q1 Journal)**

Submitted:

Drdlik, D., Marak, V., Klement, R., Tofel, P., Drdlikova, K., Hadraba, H., Chlup, Z. (2024) Basic microstructural, mechanical, electrical and optical characterisation of $BaTiAl_6O_{12}$ ceramics. *Boletín de la Sociedad Española de Cerámica y Vidrio.* **(Q1 Journal)**

Marak, V., Drdlik, D., Bijalwan, V., Tofel, P., Erhart, J., Chlup, Z., Maca, K. (2024) Effect of alumina or zirconia particles on the performance of lead-free BCZT piezoceramic. *Journal of the European Ceramic Society.* **(Q1 Journal)**